EFFECTS OF ALIGNED GRAPHENE NANOPLATELETS (GNPS) ON THE MULTIFUNCTIONAL PERFORMANCE OF CARBON FIBER REINFORCED POLYMER (CFRP) COMPOSITES

By

SAI THARUN KOTIKALAPUDI

Bachelor of Technology in Mechanical Engineering
SASTRA University
Thanjavur, Tamilnadu, India
2010

Master of Science in Mechanical Engineering
University of Florida
Gainesville, Florida
2017

Submitted to the Faculty of the
Graduate College of the
Oklahoma State University
in partial fulfillment of
the requirements for
the Degree of
DOCTOR OF PHILOSOPHY
May, 2023

EFFECTS OF ALIGNED GRAPHENE NANOPLATELETS (GNPS)
ON THE MULTIFUNCTIONAL PERFORMANCE OF
CARBON FIBER REINFORCED POLYMER
(CFRP) COMPOSITES

Dissertation Approved:

Dr. Raman P Singh

Dissertation Advisor

Dr. Sandip Harimkar

Dr. Khaled Sallam

Dr. Ranji Vaidyanathan

ACKNOWLEDGMENTS

I would like to begin by expressing my deepest gratitude to God, who has been my guiding light throughout this period. I am thankful for the blessings He has bestowed upon me and for the challenges that have helped me grow into the person I am today.

I would like to thank my advisor, Dr. Raman P. Singh, for his invaluable guidance and support throughout my academic journey. His unwavering dedication and insightful feedback have been instrumental in shaping my research.

I would also like to thank my committee members, Dr. Sandip Harimkar, Dr. Khalled Sallam, and Dr. Ranji Vaidyanathan for their thoughtful comments and constructive criticism.

Special thanks to Dr. Mishra, Dr. Vamshi and Vishal for their research pointers and moral support. I would also like to thank my lab mates Achyuth, Dr. Blaze, Dr. Libin, Dr. Rao, Dr. Ali and AJ Austin for their camaraderie, encouragement, and intellectual stimulation. Their passion for science has inspired me to strive for excellence in my own work. I also appreciate the technical assistance from Dr. Feng Lu and my colleagues at HRC, Rohit, Dr. Ranjan, Siddhesh and Dr. Prahlad for engaging in fun discussions.

I would like to take a moment to express my heartfelt appreciation to Elisa. She has been an incredible source of love, support, and encouragement in my life, and I am so thankful to have her by my side. I appreciate her patience, understanding, kindness, compassion, and ability to make me laugh even when things seem tough.

I also want to recognize the ISM community and members, Ken, Karen, Tyler and Terry for their support for international students and offering social activities, where I could unwind and rejuvenate myself. I would also like to thank Nate and Charles for being great roommates and continuous sources of encouragement.

Last but not least, I would like to thank my family, including my parents, Ramakanth and Lakshmi, my brother Charan, and my grandparents, for their love, encouragement, and belief in me. Without their constant support, I would not have been able to reach this milestone.

Acknowledgments reflect the views of the author and are not endorsed by committee members or Oklahoma State University.

Name: SAI THARUN KOTIKALAPUDI

Date of Degree: MAY, 2023

Title of Study: Effects of aligned graphene nanoplatelets (GNPs) on the multifunctional performance of carbon fiber reinforced polymer (CFRP) composites

Major Field: MECHANICAL ENGINEERING

Abstract:

This study investigates the multifunctional behavior of carbon fiber reinforced composites (CFRP) with respect to energy storage and electrical conduction applications. CFRP laminates were subjected to long-term exposure of low-density electric field by passing direct current (DC) through cross-ply laminates. The laminate resistance and the temperature changes due to Joule heating effects were monitored. A permanent change in physical material characteristics is caused by the following phenomenon, thermal decomposition of epoxy, dielectric breakdown at the carbon/fiber interface and thermal mismatch during heat/cool cycles. A 13–15% reduction in compressive strength, 6–7% reduction in Young's modulus in thickness direction, 3–4% decrease in glass transition temperature, and 41–45% increase in $\tan\delta$ was observed. Through thickness conductivity and CT scans of degraded samples showed the evidence of delamination. The inherent difference between through-thickness and in-plane properties of CFRP is the leading cause of these detrimental effects. Highly conductive aligned graphene nanoplatelets (GNPs) has the potential to bridge the inadequacies.

The unidirectional alignment process of transversely isotropic GNPs in epoxy was characterized by AC conductivity measurements. Epoxy nanocomposites reinforced by aligned GNPs are developed through out of plane electric field alignment during the curing process. A semi-empirical approach is developed to quantify the alignment process considering various parameters such as viscosity of the epoxy-blend, dimensions of the GNP and electric field strength. The quality of alignment is found to be a function of electric field intensity and concentration of GNPs. We notice an increment in dielectric constant and loss, and Young's modulus for aligned samples. We also observe and characterize the brownian movement and the growth of dielectric properties overtime. However, alignment of GNPs resulted in a heterogeneous composite. The planar alignment of GNPs in epoxy is also characterized by AC conductivity measurements. Epoxy nanocomposites reinforced by GNPs oriented with their long-axes parallel to the direction of electric field are developed during the curing process. A rotating electric field about z-axis with varying speeds for different sizes and concentrations is used to systematically align GNPs. The planar aligned GNPs is characterized by XRD analysis, SEM images and dielectric spectroscopy.

TABLE OF CONTENTS

Chapter Page

Chapter Page

LIST OF TABLES

LIST OF FIGURES

CHAPTER I

INTRODUCTION

1.1 Electrical conduction in CFRP

The use of carbon-fiber reinforced polymers (CFRP) as multifunctional composite materials continues to garner increased interest in aerospace, automobile, and energy sectors [1]. Several of these applications involve conduction of electricity through the composite laminates, which raises the question of material degradation upon exposure to these electrical currents.

The response of CFRP structures to electrical environments has been mostly studied under conditions that involve lightning strike. When composites are subjected to lightning strike, the material response involves two distinct effects. First, the "direct effects" are observed resulting from the injection of large amplitude (up to 200kA) current over a $\leq 500\mu s$ time duration, which causes local electrical, mechanical, and thermal degradation [2, 3, 4]. This instantaneous electrical power surge does not necessarily lead to catastrophic failure, but it can leave the composite surface perforated, degraded, and affects flight. Second, "indirect effects" arise from the passage of lower amplitude current (200–800A) over a 0.25–1 s time duration, which can also cause material degradation [5]. Unlike direct effects, indirect effects have often been overlooked in lightning strike studies as they are not easily discernible.

Several studies have focused on the "direct effect" degradation of composite materials subject to lightning strike conditions, as recently reviewed by Kumar *et al.* [6]. It is now understood that the application of short-duration and high-amplitude current lead to highly transient

electro-thermo-mechanical loading in composites [6]. This causes extensive physical damage and loss of mechanical properties. For example, Mall *et al.* found a 30–75% decrease in the compressive strength after simulated lightning strike of magnitude 100kA was applied on the surfaces of different nanocomposites for 40ms [7]. On the other hand, studies on low-current density degradation of composite are not as common. Early evidence of the deleterious effect of electrical conduction-induced Joule heating on the mechanical properties of composites was provided by Zhupanska and coworkers [8, 9]. Their studies were focused on increasing impact strength due to application of currents. It was found that short duration of currents increased the impact strength due to Lorentz force whereas, longer duration lead to loss of strength due to overpowering Joule heating effects. More recently, Amaro *et al.* found that composite laminates exposed to low values of DC current (0.142 A/mm^2) for one (1) to eight (8) hours exhibited a decrease in fatigue impact strength [10]. Also, Haider *et al.* investigated the effects of lower current densities applied to composite laminates for up to 30 s and found that irreversible degradation occurred if the current densities exceeded threshold levels [11]. The damage was identified to occur primarily because of Joule heating of the composite laminate which caused material damage that could be quantified using broadband dielectric spectroscopy.

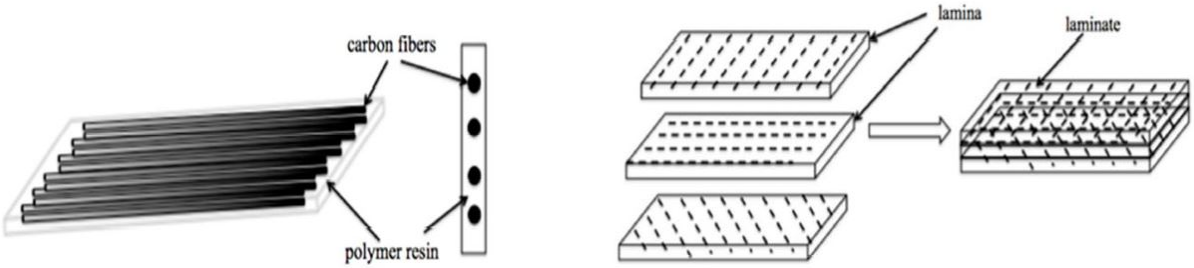

Figure 1: Typical structure of carbon fiber reinforced polymer (CFRP) laminate [12]

The electrical conduction-induced Joule heating of composite laminates is well understood and has been studied as a function of laminate configuration [13]. Zantout and Zhupanska observed a variation in initial electrical resistance between alike samples, this was attributed

Table 1: Comparison of electrical conductivity of various metals used in industry.

Material	Electrical Conductivity (S/m) at 20°C
Carbon Fiber	6.51×10^4
Copper	5.98×10^7
Aluminum	3.50×10^7
Silver	6.30×10^7
Iron	1.07×10^7
Steel	6.21×10^6

to the inherent discontinuity in the electrical contact between the composite laminate and the electrode. The contact resistance decreased with an increase in thickness of the sample, magnitude of current and time of application of current. This behavior was explained by the change in number of conducting spots near the composite electrode interface by localized temperature variations. Contact resistance causes detrimental thermal effects that need to be looked at separately. This study will only focus on Joule heating of CFRP and ensuing effects on the polymer matrix.

When current is passed through CFRP laminates along the fiber axis, Joule heating takes place due to the resistive nature of carbon fibers. Typical CFRP laminate structure is shown is shown in Fig. 1 to highlight the primary way of electrical conduction. Typical resistivity of carbon fibers is $0.65 - 1.4 \times 10^{-3}$ ohm-cm as compared to 1.68×10^{-6} ohm-cm for copper. Electrical conductivity of metals used in industry are shown in 1. This heating of the CFRP laminate will lead to thermo-oxidative ageing of the composite material and causes debonding at the fiber–matrix interface. At the lower currents (and thus associated temperatures) in consideration, this Joule heating would not affect the fibers, however, the heat generated from the fibers could decompose the polymer matrix and affect the fiber–matrix interface. Apart from thermal degradation, the polymer matrix can also experience thermal breakdown of the epoxy due to the heat generated by Joule heating near the fiber–matrix interface where, dielectric strength varies with the microstructure. A permanent change in resistance was observed in epoxy resin filled with short carbon fibers exposed to high voltage for a short time [14]. This resistance decrease was linked to localized dielectric

breakdown which generated conductive paths between insulated fibers. In addition to this, due to a significant difference in coefficient of thermal expansion of carbon fiber (-1×10^{-6} to $8 \times 10^{-6}/^{\circ}\mathrm{C}$), and epoxy materials ($45 \times 10^{-6}$ to $106 \times 10^{-6}/^{\circ}\mathrm{C}$), residual thermal stresses are introduced during heating, and cooling of the composite resulting in delamination of the plies. These phenomenon result in a change of composite's overall mechanical properties that will reflect in different mechanical tests [15].

In these studies, significant differences in electrical and mechanical properties were observed due to current conduction, but the mechanism of electrothermal degradation on CFRP has not been clearly recognized and quantified especially under conditions of long term exposure to low-density currents. Since the damage accumulation mechanism involves Joule heating that produces tremendous heat, it is instructive to see what has been researched in terms of thermal degradation of composites.

Extensive research has been done on the effects of temperature on strength of CFRP's, which showed drastic decrease in mechanical properties especially in the transverse direction and the damage mechanisms were clearly recognized [16, 17]. The introduction of thermal stresses leads to an increase of fiber waviness resulting in delamination and debonding. As multi-functional composites such as structural supercapacitors, experience repeated applications of electrical current, residual thermal effects at ambient temperature must be considered as well.

It should be noted that the link between damage accumulation and resistance change has been used for damage detection in composites by monitoring electrical and thermal characteristics [18, 19, 20, 21, 22]. In this case the damage is introduced through mechanical loading and the electrothermal characteristics are used as a monitoring mechanism. This is unlike the current situation, where the damage is introduced through electrical conduction. Both situations, however, involve a link between micromechanical damage and change in electrical and thermal characteristics of the composite laminate.

Feraboli made an effort to understand the fundamental damage response in carbon fiber–epoxy material from simulated lightning strikes and found that conduction due to a fastener embedded in the plate concentrated the damage near its vicinity [23]. Since the fastener was relatively more conductive, it was able to conduct the current quickly leaving less residual damage compared to a non fastener CFRP plate. Feraboli also compared the energy exerted on CFRP by lightning strike and the same amount of energy absorbed from a mechanical load, lightning strike was less detrimental than the impact load [24]. This shows the energy dissipation potential of highly conductive carbon fibers, which essentially reduce the damage through electrical conduction. Dhakal *et al.* experimented with conductive polymers by introducing GNPs into PANI, which increased the conductivity 40 times by using 20 wt% of graphene reinforcement [25]. Traditional methods involve incorporating a metal mesh that acts as a primary conductor, but this method is counterproductive due to the additional weight added to the system [26]. Alternative methods were employed by researchers to avoid adverse effects on strength and weight of CFRP such as using filler materials like carbon black, carbon nanotube (CNT) and graphene additives [12].

One such method is to use graphene nanoplatelets (GNPs) as a filler material in CFRP laminates to increase the electrical conductivity while improving the strength [27]. Wenzhen *et al.* incorporated 3 wt% GNPs at the fiber–matrix interphase region and obtained 180% increase in through thickness electrical conductivity [28]. Everson *et al.* dispersed 1 vol% GNPs into epoxy resin and fabricated plain weave carbon fiber laminate which showed a increase of 55% in through thickness electrical conductivity [29]. Yan *et al.* used vacuum assisted resin infusion to fabricate 5 wt% GNP laminates and noticed a two order magnitude increase in through-thickness conductivity and a negligible change in in-plane electrical conductivity [30]. Imran *et al.* observed an increase of 132% in transverse electrical conductivity of AS4-Epon 828 composite containing 1 wt% GNP [31]. However, the through-thickness conductivity of CFRP infused with GNPs remain to be unsatisfactory compared to in-plane electrical conductivity due to random distribution that does not guarantee percolated behav-

ior unless used in significant quantities. Aligned GNPs in CFRP can bridge the conductivity barrier between carbon fiber plies by achieving percolation threshold with low concentrations, increasing the through-thickness conductivity and thermal conductivity significantly which reduces the detrimental electrothermal effects caused by electrical conduction.

1.1.1 Importance of GNPs for multifunctionality

Graphene nanocomposites have been successfully implemented in manufacturing industries due to their ease of processing, lower costs and their capability to amplify thermal, electrical, and mechanical properties simultaneously [32, 33, 34]. Due to these incredible properties, graphene has been extensively used for many applications ranging from high performance energy storage devices such as supercapacitors and multifunctional batteries to electronic devices for anti-static coatings and electromagnetic shielding,lightning strike protection, microwave absorption, dielectric material in electronics [35, 36, 37, 38, 33, 39, 40, 41, 42, 43, 44, 45]. Addition of graphene to polymers has a significant impact on its electrical and thermal conductivity's, mechanical properties and polymer flexibility [45].

Graphene is a 2D allotrope of carbon with a unique honeycomb lattice that contributes to its excellent electron mobility and thermal conductivity [46, 40]. The presence of sp^2 bonds between its hexagonal arrangement of carbon atoms provides highly mobile π electrons that are responsible for graphene's exceptional electrical conductivity (6×10^5 S/m) [47]. Several of these two-dimensional layers of mono layer graphene stack upon each other using van der Waals forces, forming a graphene nanoplatelet (GNP). The structure of a single GNP is shown in Fig. 2. GNPs are widely used as a filler material in polymer matrices due to its remarkable properties, such as high electrical and thermal conductivities as well as high tensile strength and Young's modulus [48]. These particles also exhibit anisotropic properties with significantly improved electrical and thermal conductivities parallel to the surface as shown in Table 2.

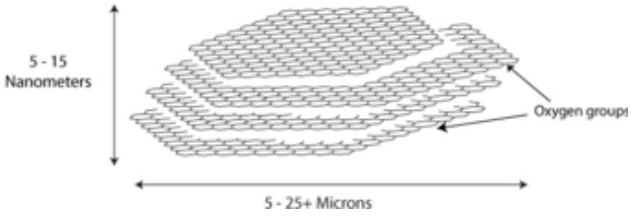

Figure 2: Representation of a single GNP [49].

Chatterjee *et al.* dispersed GNPs in epoxy composites and observed an increase of 60% in fracture toughness [50]. Imran and Shivakumar disperesed GNPs in EPON 828 epoxy and observed an increase in electrical conductivity of epoxy from 4.3×10^{-15} to 2.6×10^{-6} S/m, and doubling of thermal conductivity as well as increase in fracture toughness by one-third [31]. Yan li *et al.* exfoliated high concentrations of 5 wt% GNPs in epoxy resin and observed 160% increase in flexural modulus and 100% increase in thermal conductivity [48]. Aron *et al.* also used high concentrations (5, 10, 15 and 20 wt%) of GNPs along with carbon black in EPON 862 resin and observed a decrease in electrical resistivity of the mixture from 10^{-15} to 10^{-4} ohm $\cdot$ cm [51]. The above mentioned studies regarding incorporation of graphene had a significant improvement in properties, but problems related to agglomeration due to over usage of graphene are still persistent and needs to be addressed.

Table 2: Anisotropic properties of graphene nanoplatelets (GNPs) [49]

Property	Parallel to the surface	Perpendicular to the surface
Thermal conductivity (W/m $\cdot$ K)	3000	6
Electrical conductivity (S/m)	10^7	10^2
Tensile strength (MPa)	5	-
Tensile modulus (MPa)	1000	-
Thermal expansion (m/m/K)	5×10^{-6}	0.75×10^{-6}

1.2 Alignment of GNPs

Although, GNPs are widely used as nanofillers for various polymer nanocomposites, the resulting properties are significantly lower than the analytically predicted properties. The primary reasons being the agglomeration of particles which leads to ineffective nano-scale

regions and lack of control of orientation of these particles in the nanocomposites. The GNP is an anisotropic material whose properties in the in-plane direction are significantly higher than its through-thickness direction [52]. Present-day manufacturing techniques of these nanocomposites results in random dispersion of these particles promoting agglomeration and restricting of the usage of higher concentrations. Also, randomly oriented particles tend to neutralize the anisotropic property advantage if the statistical average is considered. To effectively use GNP's anisotropic properties, modulation of its orientation must be controlled by utilizing appropriate manufacturing processes. These methods can ensure significantly improved directional properties with low concentrations of GNPs. It was demonstrated that controlling the orientation of these particles result in remarkably increased properties in the aligned direction [53, 54]. This facilitates a way of closing the gap to the theoretically predicted properties since the bulk properties critically respond to its micro-structural framework.

1.2.1 Unidirectional alignment of GNPs

There have been several methods of controlling the orientation of anisotropic particles such as, liquid crystal method, electric field, solvent extraction, and magnetic field [55]. Of these, electric field alignment has been utilized favorably due to ease of processing and scalability of the process. Orientation and redistribution of nanoparticles in a polymeric suspension by using external electric field has been theorized and proven for graphite, ceramic and glass fibers [56]. Following the same principles, Wu *et al.* aligned multilayer graphene flakes (0.1–3.2 wt%) in epoxy with an external electric field to improve multifunctional properties of graphene composites such as directional electrical conductivity, thermal conductivity, and fracture toughness [53]. Kwon *et al.* studied the growth of mechanical elasticity and DC electrical conductivity of poly(lactic acid) composite containing 0.34 vol% of GNPs under the application of a strong electric field at low frequency of 60 Hz [54]. Both authors validated the orientation of GNPs using optical imaging and DC conductivity measurements

taken during the alignment process. These works were done for very low weight fractions (0.054 and 0.028 vol%) and they developed analytical models for prediction of rotation and translation times of GNP and time required to obtain percolation threshold. However, these models fail to predict the same for higher weight fractions of GNP, because the behavior becomes complex as particle to particle interactions and viscosity increases proportionally. Hence, a semi-empirical approach is required to characterize the quality of alignment for higher concentrations. The resistivity of the bulk material is dependent on the individual orientation of the particles in the system [57]. Therefore, capturing the displacement and resistive currents through the system during the process of alignment will provide vital information about the electrical networks and orientations of GNPs occurring in the system [58].

Apart from electrical properties, mechanical properties can also be increased by orienting graphene. Khoramishad and Vafa used DC electric field to align 0.3 wt% of graphene oxide nanoplatelets (GONPs) in epoxy to improve the fracture behavior of adhesive joints. They achieved a 56% increase in maximum load of adhesive joints compared to unaligned adhesive joints [59]. However, application of DC fields can lead to permanent migration of particles to the electrodes of the applied field due to directed movement, resulting in unwanted electrophoretic deposition [60, 61, 62]. GONPs were aligned by Besharat *et al.* in polyethersulfone films and an increase of 24% in tensile strength was noticed for 0.1 wt% concentration. TEM also revealed that higher loadings (1–2 wt%) resulted in larger agglomerations which could not be oriented perfectly along the electric field [63]. Su *et al.* investigated the increment of mechanical properties such as Young's modulus and tensile strength along the aligned direction of reduced graphene oxide (rGO) and functionalized graphene (FG) and found an 18% increase in Young's modulus for 1 wt% rGO [64]. Based on these studies, measuring the mechanical properties of aligned graphene nanocomposites should provide validation of the conductivity data obtained during the alignment process as the formed GNP networks are preserved during curing of the epoxy.

In addition to this, due to their excellent dielectric, electrical and mechanical properties, GNPs have been extensively researched as a potential dielectric additive for nanocomposites for applications such as electromagnetic shielding, microwave absorption, embedded capacitors and energy storage [65, 66, 67]. The dielectric properties primarily depend on the polymer matrix, electrical conductivity of the nanofiller, aspect ratio and their distribution in the polymer matrix. Ravindran *et al.* studied the dielectric effects of different GNP sizes and concentrations and found that the dielectric constant of the nanocomposite is highly dependent on the GNP concentration and AC frequency [68]. Also, Figueiredo and Cavaleiro formulated an analytical model for dielectric behavior of ellipsoidal particle system by considering composition, size and orientation of the particles. They found that for a model that represents GNPs such as an oblate spheroid, the effective dielectric properties vary with the orientation of particles [69]. Li and Kim performed a parametric study on the aspect ratio of GNPs and found that it was a predominant factor relating to percolation threshold of these nanocomposites [70]. It is well know that percolation has a direct correlation to dielectric properties [71]. In addition to this, the interface effects from interfacial polarization have been studied thoroughly and its effects on the dielectric constant have been modeled and experimentally verified [72, 73, 74, 75]. Based on these studies, it is instructive to study the effect of aligning GNPs in epoxy has on its dielectric properties due to the changing orientation, enhanced interface effects and GNP concentration.

1.2.2 Planar alignment of GNPs

GNPs exhibit significantly improved properties along the planar direction compared to through thickness direction. Due to their unique shape (oblate spheroid), they have a very high aspect ratio (600-10000) which results in a higher surface area [76, 68]. The high surface area facilitates greater interactions with host polymer, phonon transport, electrical and thermal conductivity [77]. However, the high surface area gives rise to significant Van der Waals forces and $\pi - \pi$ interactions. These forces often result in agglomeration and stacking

of GNP particles which reduces the effectiveness of an individual particle, causing a detrimental effect on the performance of the nanocomposite. In addition to this, the performance of the GNP nanocomposite highly depends on the orientation of the GNPs due to their substantial difference in properties along the plane and through-thickness direction and random orientation of GNPs tend to neutralize this effect. The intrinsic properties such as elastic, thermal, electrical properties of graphene related materials based on orientation has been identified [78, 79, 80, 81].

Notable methods of controlling the orientation of GNPs and other forms of graphene include the use of external electric field, magnetic field, solvent evaporation, and layer-by-layer self assembly method [55]. Of these electric field and magnetic field can be used without any solvent or surfactanats. Yan *et al.* aligned graphene nanosheets (GNS-Fe_3O_4) in epoxy composites using magnetic field. The thermal conductivity in in-plane direction was three times the through-thickness direction [82]. However, usage of magnetic field is restricted to magnetic nanoparticles and the neccessity of high magnetic fields [83, 84]. The most widely reported method for aligning GNPs was using external electric field due to its ease of processing conditions and the ability to modulate the degree of orientation [53]. Several studies have demonstrated the beneficial effects on the mechanical, electrical, thermal and fracture properties of nanoncomposites resulting from aligning graphene platelets through an external electric field. Su *et al.* aligned reduced graphene oxide (RGO) and functionalized graphene (FG) using AC electric field and found an increase in tensile strength and modulii along the aligned direction [64]. Similar results pertaining to growth of elastic modulus and DC conductivity were observed by implementing AC electric field on GNPs in poly(lactic acid) [54, 85]. Wu *et al.* observed 7-8 orders of magnitude improvement in the electrical conductivity, 60% increase in thermal conductivity, and 900% increase in fracture toughness due to aligned GNPs in epoxy [53]. In these studies the chain formation of GNPs with time of exposure of electric field was observed under optical microscope along the through-thickness direction. In all cases, due to the lack of control of chain formation, agglomeration

of particles along the chains takes place as electric field is continuously applied [59]. This results in ineffective usage of GNPs as agglomeration along the chains reduces the surface area for adhesion. Moreover, alignment induces property advantages along the through-thickness direction which is the electric field direction and the transverse properties remain unaltered. *et al.* observed a 2-3 order increase in DC electrical conductivity in the aligned direction compared to randomly oriented samples, but wheres in the transverse direction the conductivity was similar to randomly oriented samples [53]. Unlike one direction alignment, planar alignment of GNPs will fully utilize the transversely isotropic properties of GNP and will yield a uniform array capable of developing tunable nanocomposites. Furthermore, using rotating electric field generates repulsion of adjacent particles which prevents chain formation that could lead to agglomerated chains.

Planar alignment of GNPs will lead to anisotrpoic electrical, mechanical and thermal properties in the bulk composite. Of these, dielectric properties of graphene nanocomposites are of particular interest due to their potential applications such as integrated circuits, electromagnetic shielding, embedded capacitors [86, 87, 88, 89]. The presence of GNPs in polymer matrix significantly alters the dielectric properties of the composite. Primary factors affecting these properties are dielectric mismatch between the host polymer and GNP, size, and concentration of GNPs. In addition to these, the orientation of GNP plays an important role in obtaining high dielectric constants [90]. The effect of concentration, size and surface area of GNPs on dielectric properties of epoxy nanocomposites are well studied and documented. Ravindran *et al.* studied the effect of GNP size, surface area and concentration for epoxy nanocomposites and found that the dielectric constant increases with concentration and surface area but reduces with the thickness of GNP [68]. Other similar studies show that the aspect ratio of GNP plays an effective role in enhancing the electrical properties of various polymer based nanocomposites [91, 92]. The high aspect ratio constitutes for a larger interface region which enhances the Maxwell-Wagner-Sillars (MWS) effects resulting in higher dielectric constant [71]. However, research based on the effects of orientation of GNPs on

the dielectric properties of the bulk nanocomoposite are deficient. Yousefi *et al.* fabricated aligned reduced graphene oxide (rGO) nanocomposites using an all aqueous casting method and observed a significant increase of dielectric constant along the aligned direction [86]. This was primarily attributed to achieving percolation threshold and increased MWS effects. Stehle *et al.* also noticed a significantly higher in-plane dielectric constant compared to through-thickness directions of graphene oxide membranes prepared by layer-by-layer self assembly [93]. However, Santos and Kaxiras found that the dielectric constant of graphene is $\tilde{3}$ in the through-thickness direction and $\tilde{1}.8$ in in-plane direction and are dependant of the layers and electric field strength [94]. Due to the peculiar dielectric nature of graphene, it is worthwhile to investigate the dielectric behavior of planar aligned GNPs.

1.3 Solid polymer electrolyte (SPE) and structural supercapacitor (SSC)

Solid polymer electrolytes (SPEs) are being investigated extensively to assess their application prospects in fuel cells, solid state batteries and structural supercapacitors [95, 96, 97, 98]. The main purpose of these solvent-free electrolytes is to prohibit the growth of lithium dendrites and offer substantially increased safety features to the energy storage system. The secondary purpose emphasizes on the load bearing capabilities, which is especially true for the case of structural supercapacitors. Apart from these, SPEs have interesting features such as fire and leak proof, low volatility, high thermal, electrical, mechanical and electrochemical stabilities. They also eliminate the usage of corrosive liquids which increases their shelf life and operating temperatures. However, the ionic conductivities of SPEs remain to be almost three orders magnitude less than liquid electrolytes.

Dry solid electrolyte based on polyethylene oxide (PEO) was identified and investigated as a primary ion carrying component due to its high ionic conductivity in amorphous state [99]. However, the performance of PEO based SPE was unsatisfactory due to poor ionic conductivity at room temperature due to crystallization [100]. To decrease the polymeric crystallization, small size electrochemically inert fillers can be added to the conducting polymer.

These fillers not only improve the ionic conductivity but also provide improved mechanical and thermal stability while decreasing the interfacial resistance [101]. Particles with high surface area to volume ratio are preferred due to their effectiveness to reduce crystallization. These fillers can also deform the lattice structure resulting in the formation of interfacial layers that helps trapping of ions within grain boundary. Researchers have used aluminum oxide (Al_2O_3), titanium oxide (TiO_2) and zirconium oxide (ZrO_2) as high surface area fillers and a reasonable increase in ionic conductivity was achieved [102, 103].

Addition of doping salts to the polymer electrolyte will provide a source of free ions as well as increase the ionic conductivity of the SPE. Increased performance can be achieved when the lattice energy of the participating salt is low and the dielectric constant of the polymer is high [104]. The added salt will also interact with the ion-conducting polymer matrix and inorganic fillers by Lewis acid-base reactions through the surface of functional groups and help dissociation of lithium salt [105]. Researchers have used lithium salts such as $LiPF_6$, LiTFSI, $LiClO_4$ and $Li_2B_4O_7$ as charge carrier providers in various polymer electrolytes [104]. Of these LiTFSI is more appropriate due its bulky structure that increases electrochemical stability, dissociates well in low dielectric solvents, non-corrosive to electrodes and also possess a high transference number[106, 107].

Graphene oxide (GO) is a promising filler material for improving ionic conductivity due to its electrically insulating properties resulting from disrupted sp^2 bonded networks [108]. The large surface area and the presence of functional groups like alcohols, carboxylic acid, and epoxides promote ion accommodation, potential formation of ion transport channels and increased salt dissociation. In addition to this, GO exhibits strong interactions with PEO, thus reducing the interfacial resistance through low-energy conducting paths and increasing the thermo-mechanical stability of the polymer electrolyte [109, 105]. Yuan *et al.* fabricated a PEO/GO composite membrane with ionic conductivity of 0.086 mS/cm, Young's modulus of 3.21 GPa and electronic resistance of 20 MΩ [110]. Saleem *et al.* observed a significant

increase in ionic conductivity of 0.027 mS/cm and a decrease in activation energy which shows a decrease in crystallinity due to addition of lithium salts in PEO/GO thin film SPE [111]. Megying *et al.* achieved a two order of magnitude increase in ionic conductivity and 260% increase in tensile strength by incorporating 1 wt% GO into PEO and $LiClO_4$ SPE [112]. These studies revealed the advantages of using GO as a conductivity enhancer while improving the strength of the polymer electrolyte which is a necessity for structural supercapacitors.

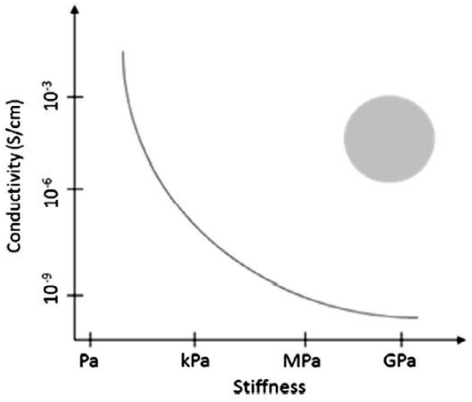

Figure 3: Conductivity versus stiffness of solid polymer electrolytes, gray area indicates the desired properties [113]

For the performance of structural supercapacitor, mechanical and ionic properties of the SPE are equally important unlike solid state batteries, where ionic properties are a priority. In general, the ionic conductivity and stiffness of a solid polymer electrolyte are inversely related as depicted in Fig. 3. Any increment of mechanical properties will reduce the ionic conductivity and *vice versa* [114, 115]. To achieve higher mechanical properties, researchers have used a bicontinous ionic liquid-epoxy resin system which provide structural properties while retaining good amount of ionic activity [114]. Shirshova *et al.* obtained room temperature conductivity of 0.8 mS/cm for a mixture of 30 wt% structural resin and 70 wt% of ionic liquid, but a drastic reduction in Young's modulus (1250%) was observed [116]. The ionic liquid (IL) phase is responsible for the softening of epoxy, hence optimum ratio of structural epoxy to ionic liquid must be considered for achieving acceptable properties. Investigation of

the microstructure of the electrolyte revealed a bead like structure with regions rich in ionic liquid and porosity in epoxy resin rich regions were found [113]. Porosity can be reduced by increasing the resin content which also increases the stiffness but will restrict the ion movement considerably. These conflicting factors reduces the capabilities of the SPE and needs to be addressed.

The effects of the doping salt content on the ionic conductivity of the SPE for structural supercapacitor applications have been studied as well. Javiad *et al.* fabricated a solid polymer electrolyte using 10 wt% of 1-ethyl–3-methylimidazolium bis(trifluoromethysulfonyl) imide (EMITFSI) in 82.6 wt% of polythylene glycol diglycidylether (PEGDGE) and crosslinked with tri–ethylene-tetramine (TETA) [117]. They varied the concentrations of EMITFSI and achieved an ionic conductivity of 0.176 mS/cm. Kim *et al.* also varied the concentration of -ethyl-3-methylimidazolium tetrafluoroborate $EMIBF_4$ in ionic liquid (1-ethyl-3-methylimidazolium tetrafluoroborate) from 0 to 0.3 mol and observed a maximum ionic conductivity of 0.325 mS/cm [118]. In both cases the ionic conductivity increased due to addition of IL, reaching a maximum value and decreased with further addition of IL. The increase in salt content will have adverse effects by increasing the viscosity of the IL, hence the ratio of doping salt to ionic liquid content must be optimized depending on the type of chemicals used. James *et al.* found 9–12 wt% of lithium trifluoromethanesulfonate salt with polyethylene glycol (PEG) had minimal impact on compression modulus and significant influence on ionic conductivity [119].

Although several methods have been employed to increase the ionic conductivity of the SPE such as blending of structural and gel-like electrical phases with additional lithium ions, blending structural resins with ionic liquids and utilizing inorganic fillers, the results are unsatisfactory and there is a lot of scope for improvement. The ratio of IL to structural resin and doping salt to IL have been optimized, which saturated the ionic conductivity. Hence, modifications of SPE by including inorganic fillers must be explored further.

1.4 Motivation

The aim of this study is to understand graphene alignment and identify its application in carbon fiber reinforced polymer composites to imbue enhanced multifunctional properties. This study will investigate the behavior of CFRP laminates under constant low density currents to understand the electrical effects on mechanical strength and the evaluate the need for graphene alignment. Graphene alignment will be performed in pure thermosetting polymer and AC conductivity obtained during the process will be used to characterize the quality of alignment. This will be extended to planar alignment to increase the essential properties such as dielectric constant and mechanical strength while possessing a low dielectric loss which is necessary for energy storage applications. An itemized list of primary objectives of this research is presented below:

- In order to understand the effects of electrical conduction on CFRP laminates, an experiment is designed to study the effects of long-term exposure of low-density electric field on the mechanical degradation of CFRP. Experiments are performed using an in-house setup to study the effects of passing low constant direct current (DC) on cross-ply CFRP laminates. A constant current study is conducted to characterize the voltage across the laminate over a period. It is indicative that the strength of the polymer depends on the integrity and type of bonds and the observed resistance change is a perceptible way of demonstrating the change in mechanical properties. The combined effect of electrical and thermal fields is studied by mapping the surface temperatures continuously on the entire length of the laminate. Research shows that the presence of non-conducting epoxy undergoes localized dielectric breakdown near the carbon epoxy interface. In order to quantify the degradation, combined loading compression (CLC) and dynamic mechanical analysis (DMA) tests are performed on coupon size samples which are electrically degraded for a definite period.

- The dielectrophoretic behavior of transversely isotropic graphene nanoplatelets (GNPs)

in thermoset epoxy polymer under alternating electric field will be characterized depending on factors such as alignment time, chain formation, magnitude of electric field and thickness of specimen. To accomplish this, work done by Wu *et al.* is replicated by creating a mold that can generate an alternating electric field between two aluminum plates separated by insulating epoxy containing GNPs [53]. The AC current flowing through the bulk system will track minuscule changes in orientation and simultaneous chain formation. A semi-empirical approach is developed to quantify the alignment process considering various parameters such as viscosity of the epoxy-blend, dimensions of the GNP and electric field strength. Variation of AC current flow is used to study the alignment of different concentrations of GNPs (0.7, 1.4 and 2.8 wt%). The effect of different electric field strengths (25–55 V/mm), and the evolution of chain formation with time and brownian motion of GNPs for 1.4 wt% concentration is also studied. The validation of the experiment is done Young's modulus measurements in the aligned direction and dielectric spectroscopy measurements.

- The understanding of unidirectional alignment of GNPs will be extended to the planar alignment of GNPs. AC conductivity measurements formulated using displacement current will be used to characterize the planar alignment process of transversely isotropic graphene nanoplatelets (GNPs) in a thermoset epoxy polymer. Epoxy nanocomposites reinforced by GNPs oriented with their long-axes parallel to the direction of electric field will be developed during the curing process. A composite electrode that is capable of producing a cylindrical specimen will be developed. A rotating electric field about the z-axis will be applied as the epoxy is being cured. The rotation speed of electric field will be calculated using an analytical model considering parameters of GNPs such as concentration, thickness and diameter of GNPs. Experiments will be conducted for two different types of GNPs (M5 and M25) whose diameters are 5 μm and 25 μm respectively. The concentrations of these GNPs will be varied from 0.175 to 1.4 wt%. Validation of the planar alignment will be done by AC conductivity mea-

surements and dielectric spectroscopy. The fracture surfaces of planar aligned GNP composites will be viewed under as SEM. Furthermore, XRD analysis will be used to evaluate the anisotropy in the final GNP composite.

CHAPTER II

DEGRADATION MECHANISMS IN CARBON FIBER-EPOXY LAMINATES SUBJECTED TO CONSTANT LOW-DENSITY DIRECT CURRENT

In this study, we have investigated and quantified the degradation of carbon fiber–epoxy interface due to long term exposure of low-density direct electric currents in cross-ply CFRP's.

2.1 Materials and Methods

2.1.1 Experimental Setup

The purpose of these experiments is to understand the mechanisms contributing to the degradation of cross-ply CFRP's subjected to low constant direct currents. Figure. 4 shows the schematic of the electrical setup, which was developed taking into consideration the efforts of Zantout and Zhupanska [13], Telitchev *et al.* [8], Sierakowski *et al.* [120], and Deirling and Zhupanska [121]. The three essential requirements for the electrical setup are: (i) a DC power source with high power and accuracy, (ii) a high frequency steady temperature recording device to capture minor changes, and (iii) a reliable electrode fixture capable of passing uninterrupted flow of DC for a given period.

The DC power supply (6031A, HP-Agilent Santa Clara, California) has a current rating of 120A and voltage rating of 20V. The power source was connected to a computer through a GP-IB cable. It was controlled by SCPI command language and voltage/current characteris-

tics were recorded. Commercially available infrared multi-array sensor (MLX90621, Melexis Inc, Nashua, New Hampshire) was used to capture the temperatures over a field view of $30° \times 120°$. The IR camera has a red pointer to ascertain uniform view of temperature grid.

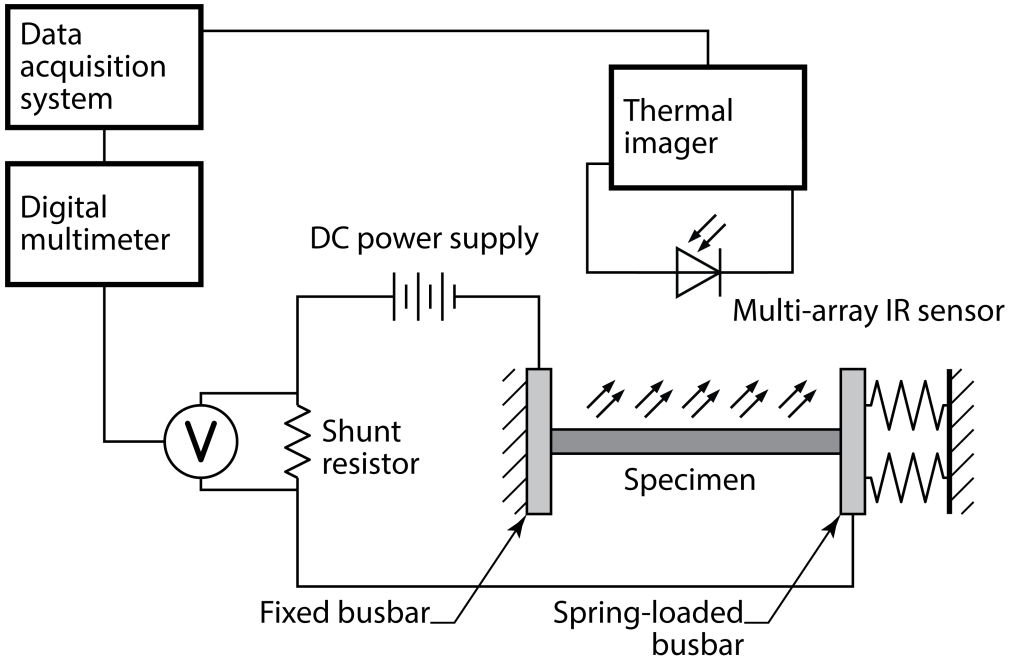

Figure 4: Schematic of the electrical degradation test setup for CFRP laminates.

The custom fixture is an improvement of Zantout and Zhupanska [13]. Their fixture consisted of two fixed copper busbars. Instead, we use one fixed and one spring-loaded busbar which can adjust to dimensional changes of CFRP plate. The fixture is a standalone unit capable of accommodating $250 \times 100 \times 8$ mm rectangular plate specimen of uniform thickness. The specimen is placed in between two copper busbars which are connected to the power supply. The left busbar is fixed, and the right busbar is movable to accommodate different sizes of specimens. To keep the CFRP specimen in place, compression springs were employed against the movable bus bar. From the weight of the copper bar, the approximate spring coefficient was calculated to be around 192.6 N/m and to avoid tilting of the busbar, four springs were used; minimal compression of the samples was ensured to avoid introducing new stresses. The IR sensor was housed on a wooden construct which has the capability of horizontal, vertical, and angular movements to capture thermal data for different sample sizes. The real

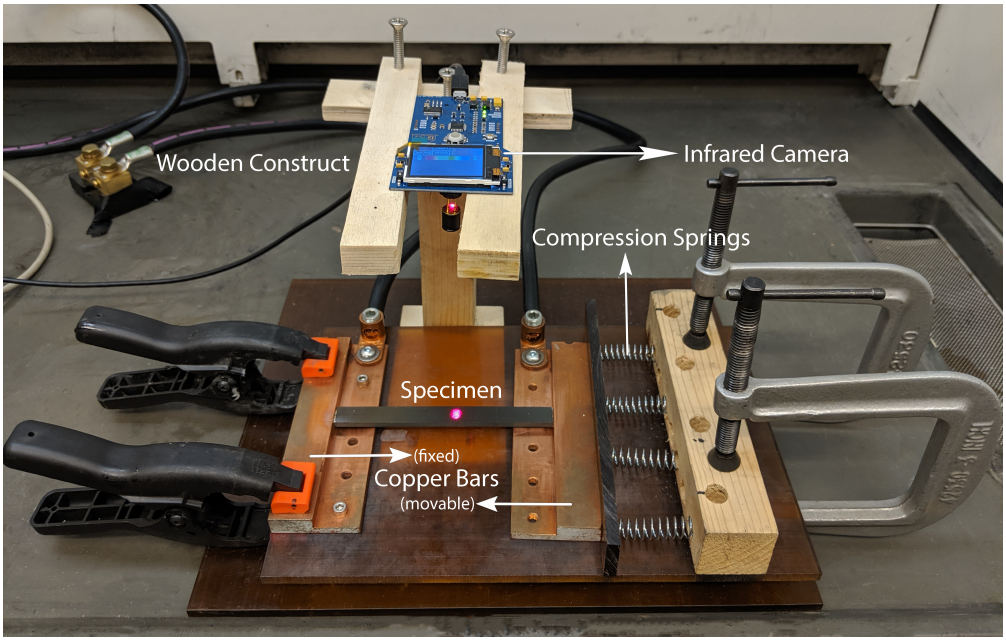

Figure 5: Real experimental setup for electrical degradation of CFRP specimens. The infra red camera is located on the wooden housing.

experimental setup is shown in Fig. 5. During temperature recording, the coupon sample is divided into twelve segments of equal length to obtain a 12×1 uniform temperature grid. Temperature measurement is not only an indirect identification of the conduction paths in the sample, but also assists in estimating the induced temperature effects on epoxy due to Joule heating of carbon fiber. Shunt resistor and AC-DC digital multi-meter was used to ensure accurate voltage supply. The voltage and current changes were logged into an excel sheet via visual basic code. The temperature was monitored and recorded through an Arduino board which using an in-house data acquisition code. Temperature and voltage data were documented every 30 seconds to track small variations.

2.1.2 Materials and Preparation

Cross-ply CFRP plate of size 500×500 mm with a thickness of 4 mm was procured from Zhongfu-Shenying Carbon Fiber Co, Jiangsu, China for the analysis. It is made of T300-3k carbon fibers and E51 thermosetting epoxy. Coupon samples of size 140×13 mm were cut from the plate using a tile saw (MK-370, MK Diamond Products, Torrance, California).

Cross-ply samples were considered because two types of electrical conduction can occur, axially through carbon fibers and electron hopping through parallel fibers. The axial current causes resistive heating in the carbon fibers and the voltage difference between parallel fibers would cause localized dielectric breakdown and cracking of the epoxy.

Good electrical contact of the composite specimen with copper electrodes must be maintained throughout the experiment to obtain repeatability and to avoid hot spot formation. Due to the presence of an insulating medium between the fibers, an effective contact must be ensured by reducing the contact resistance. There are two factors associated with contact that govern the quality of electrical characterization, surface roughness and change in dimensions during testing. The first issue was addressed by preparation of contact surfaces, where the edges of the coupon samples of CFRP were sanded with different sandpaper grits in an order of, 320, 400, 800 to form a smooth surface. The orthogonality of the edges was visually examined through a magnifying glass and plane surface was verified. The sanded ends were varnished with an electrically conductive epoxy (Duralco 120, Cotronics, Brooklyn, New York) to reduce the contact resistance between CFRP and copper electrodes. The samples were left to cure at room temperature for 24 hours. Excess resin was lightly sanded with 1200 grit paper to obtain a smooth texture of silver oxide layer. This process is critical, since the current carrying capacity is drastically reduced by contact resistance. The second issue addresses the shrinkage of the CFRP sample in the axial direction due to thermal contraction of carbon fibers. According to Schapery equation [122], the CTE of the cross-ply composite used, is calculated to be around $-1.2 \times 10^{-6}/^{\circ}\mathrm{C}$. This would cause a shrinkage of 0.023 mm in the axial direction for a sample length of 140 mm. This change in dimension is a significant factor to be considered, since there is a high possibility of losing contact if the electrodes were fixed. This issue was resolved by using four compression springs which aided in the adjustment of the busbar.

2.1.3 Electrical Degradation

By dynamic mechanical analysis (DMA-Q800, TA Instruments, New castle, Delaware), the T_g of the composite was found to be near 165.8°C. The density of current to be passed was determined by trial and error, considering the glass transition temperature of the sample. The samples could pass a constant current of 0.22 A/mm^2 lengthwise without having any adverse burning near the contacts.

Five CFRP samples of size 140 × 13 mm were subjected to 0.22 A/mm^2 constant direct current for two different durations, (3 hrs and 24 hrs). Besides this, we also investigated the effects of repeated current application on CFRP samples for 3 hours. A similar approach was followed by Miller and Feraboli [123]. They observed a gradual reduction in resistance for repeated application of high currents (30A) in regular intervals of 10 seconds. Similarly, five identical undegraded samples were subjected to a fixed value of current 0.22 A/mm^2 for one hour, then the samples were allowed to cool down to ambient temperature naturally, and current was supplied for an hour again. The specimen was left in the fixture while it returned to ambient temperature, it should be noted that the cooling time was not considered. The amount of time exposed is three hours, so three cycles were monitored, and voltage-time behavior was characterized.

Although the voltage curve can be used to assess the damage, thermal effects superimpose the electric effects on epoxy. To distinguish between electrothermal and thermal effects on CFRP, few samples were subjected to isothermal conditions in a forced air oven (1350FM, VWR International, Radnor, Pennsylvania) at a temperature of 160°C for two different durations (3 hrs and 24 hrs). This temperature was chosen to simulate the conditions experienced at the mid span of the samples due to passage of direct current, which is further explained in the results section. Table 3 summarizes the different tests performed on cross-ply samples.

Table 3: Summary of different tests performed on cross-ply CFRP coupon samples. Five samples were tested for each case.

Sample type	Exposed conditions
ED-3hrs	Electrically degraded for 3 hours
ED-24hrs	Electrically degraded for 24 hours
ED-Cyclic	Electrically degraded for 3 hours (Intervals of 1 hour)
Oven heated-3hrs	Isothermal at 160°C for 3 hours
Oven heated-24hrs	Isothermal at 160°C for 24 hours

2.1.4 Material Analysis and Characterization

In order to quantify the electrical degradation on mechanical properties, compression and DMA tests were performed on five undegraded, five electrically degraded (ED-3hrs and ED-24hrs), and five cyclically degraded samples (ED-Cyclic). Compression strength of CFRP is critically dependent on the polymer's ability to support the reinforcing fibers and resist buckling. To avoid excessive buckling during compression tests, combined loading compression (CLC) tests were carried out on the coupon samples according to ASTM D6641 [124]. Compression tests were also performed on five oven heated samples (Oven heated-3hrs and Oven heated-24hrs) to identify the mechanisms and the extent of thermal effects on CFRP.

Glass transition temperature (T_g) range of a thermosetting polymer indicates the transition from a rigid state to a more rubbery state. It also indicates the degree of cross-linking of the polymer matrix. Higher T_g value correlates to higher cross linking and higher compressive strength of the epoxy. DMA (Dynamic mechanical analysis) was used to calculate the T_g for samples exposed to different conditions. DMA is also used to measure stiffness and damping characteristics which are reported as loss modulus (E''), storage modulus (E'), and $\tan\delta$. Basically, $\tan\delta$ can be used to characterize the storage and loss moduli of the material at a particular temperature. The value of δ can lie between 0° and 90°. As δ approaches 0°, the material exhibits pure elastic behavior while 90° is purely viscous behavior. Besides T_g, damping can also be used to interpret the level of fiber–matrix adhesion. The $\tan\delta$ values obtained from flexural deformation mode of DMA proved to be more sensitive for the study

of the carbon fiber–epoxy interface [125]. Three samples from each category were tested on a dual cantilever beam with 1 Hz frequency and isostrain conditions. T_g values were extracted from the peaks of $\tan\delta$ curves.

Due to electrically conductive behavior of CFRP laminates, damage detection such as matrix cracks, delamination and fiber breaks is possible by calculating the resistance change in in-plane and through-thickness directions [126, 127, 128]. In cross-ply CFRP samples, current primarily flows through fibers when potential is applied in transverse and longitudinal directions. But when potential is applied in the thickness direction, delamination can be detected which is often difficult to measure by visual inspections [129, 130]. In this study, the mid span of the degraded and undegraded samples were cut into three equal segments of size 13×13 mm by using a tile saw and DC resistivity was measured in through-thickness, transverse and longitudinal directions by applying a constant voltage of 100 mV using a DC power supply and measuring the current by a digital multimeter (5491B, BK Precision, Yorba Linda, California). Electrically conductive epoxy was applied on the surfaces before measurement and 9 segments were tested for each case.

In addition to this, modulus of the degraded and undegraded samples was measured using ultrasonic pulse-echo method. Negative square wave pulser-receiver (5077PR, Panametrics, Waltham, Massachusetts) was coupled to an oscilloscope (3052, Tektronix, Beaverton, Oregon) to measure the ultrasonic sound wave propagation. Young's modulus in the thickness direction was measured from the density, shear wave and longitudinal wave speed at the mid span of the specimen.

Finally, the internal micro-scale damage of the degraded samples were analyzed using a X-ray computed tomography machine (Xradia 410, Zeiss, Oberkochen, Germany). 3D images of size $1000 \times 1000 \times 1000$ pixels of the damaged surface were captured with a high resolution of 0.7 micron to investigate the micro-scale damage. Thermal and electrically degraded sample images were compared to analyze the damage accumulation behavior.

2.2 Results and Discussion

The temperature profile of a coupon sample exposed to direct current of magnitude 0.22 A/mm^2 for 3 hours is depicted in Fig. 6. As mentioned in the experimental setup section, the coupon sample is divided into 12 segments for temperature measurement. Segments 1, 2, 3, 10, 11, and 12 are located near the extremes of the specimen. These segments experience detrimental effects from contact resistance heating at the composite-electrode interface. These edge effects cannot be avoided and can often overwhelm the effects of electrical conduction. These effects exponentially decrease as we move to the center of the specimen. It can also be noted that the temperature profile at segments 4 to 9 is uniform, which can be considered as the mid span of the specimen. The difference in temperatures between the ends of specimen and the mid span was (10–20)°C above the mid span temperature. In addition to this, more emphasis was laid on the mid span of the specimen because, in compression tests the sample fails at the mid span and also to avoid contact resistance effects. Therefore, for all degradation studies, the resistance change was studied along with average mid span temperature (Average of segments 4–9). Figure. 6 also shows the laminate resistance history of the same sample for 3 hours. The initial increase in resistance due to temperature increase can be attributed to the positive temperature coefficient behavior of carbon fibers [131]. The variations in temperature and resistance are synchronous and complement each other as expected. We can also observe that both resistance and temperature fields start stabilizing after half an hour. This shows the direct correlation between resistance change and temperature.

The normalized resistance history for five identical laminate samples subjected to direct current of magnitude 0.22 A/mm^2 for 3 hours is shown in Fig. 7. Here, R and R_o represent instantaneous resistance and initial resistance of the laminate, respectively. Since there was no noise or sharp variations in the curves obtained, a good contact between the copper bars and the samples is assumed. Also, since the composite adheres to Ohm's law, the varia-

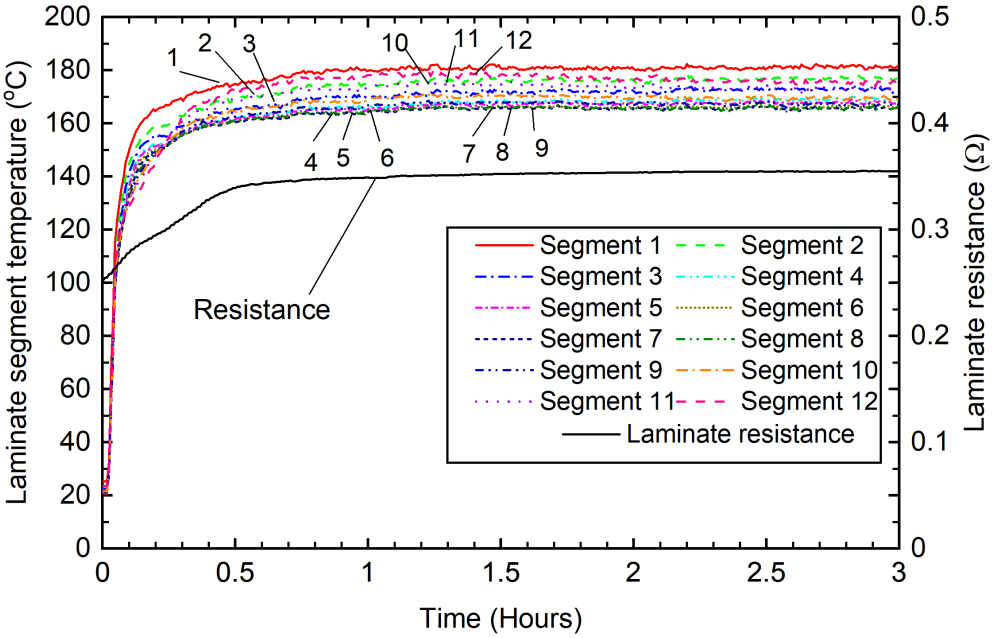

Figure 6: Laminate segment temperature and resistance variations of a coupon sample exposed to 0.22 A/mm^2 direct current for 3 hours. The coupon sample is divided into 12 equal segments and each curve represents the temperature variation of the specific segment.

tion of voltage gradient is directly proportional to resistance change within the composite, provided that constant current is maintained. The evident change in resistance signifies the material changes due to Joule heating effects, local dielectric breakdown of the epoxy and delamination. The variability from experiment to experiment can be ascribed to the fact that every sample has different internal anisotropy, resistance, and variable number of conducting channels. However, in majority of the samples an initial increase in resistance can be observed which typically takes about an hour to stabilize. Phase I in Fig. 7 shows a gradual increase in resistances of identical samples for a period of one hour. This peculiar behavior can be attributed to Joule heating of the carbon fibers due to electrical conduction, which causes micromechanical damage to the surrounding epoxy leading to matrix decomposition. Phase II indicates the region of stability, which occurs after dielectric breakdown of the epoxy between the plies due to a potential gradient or between parallel fibers due to impurities present in the polymer. In solid polymers, dielectric breakdown involves an irreversible damage in the form of carbonization of the polymer and destruction of the molecular struc-

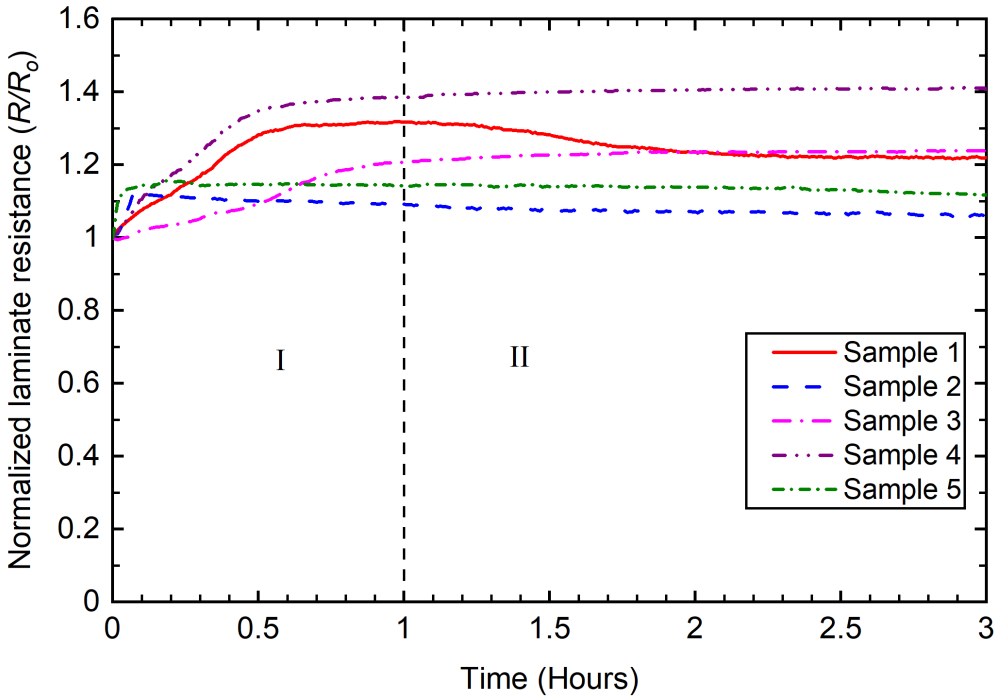

Figure 7: Normalized resistance (R/R_o) history of coupon samples exposed to 0.22 A/mm^2 direct current for 3 hours. R is the instantaneous resistance and R_o is the initial resistance of the composite laminate.

ture, which provokes conducting pathways [14, 132]. Depending on the degree of anisotropy of the sample, dielectric breakdown takes place after a certain period which leads to opening of new pathways for current flow, hence reducing the resistance of the material. However, in samples 3 and 4 the resistance continues to increase, signifying that Joule heating effects are still persistent and more time is required for dielectric breakdown to overpower thermal effects thus requiring more than 3 hours to acquire stabilization. In order to understand the correlation between time and variation in resistance of the composite laminate, samples were exposed to 24 hours direct current.

The average temperature at the mid span of the specimen vs time for the same set of five samples exposed to DC of magnitude 0.22 A/mm^2 for 3 hours is shown in Fig. 8. Any distinct variations in the temperature field can be attributed to change in resistance that occurs due to micromechanical damage from thermal mismatch, epoxy decomposition around the fiber, and formation of new electrically conductive paths which cause localized heating. During the

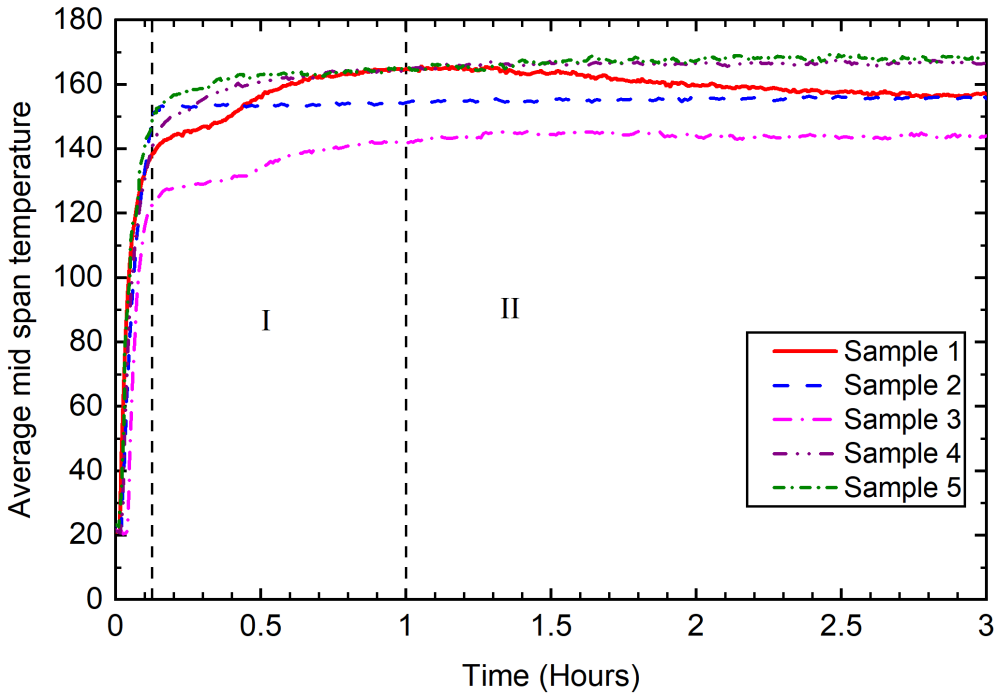

Figure 8: Average mid span temperature variation of coupon samples exposed to 0.22 A/mm^2 direct current for 3 hours.

first five minutes of current conduction, rapid heating of the composite occurs due to positive temperature coefficient of CFRP, followed by a gradual increase (phase I) until equilibrium is achieved, which is depicted by phase II in Fig. 8. In phase I, temperature increases due to increase of resistance from Joule heating, this significant rise can be noticed in all the samples, which takes an hour to stabilize depending on the internal anisotropy and the degree of epoxy degradation. Phase II is characterized by a decrease in temperature due to a decrease in resistance resulting from dielectric breakdown. Any structural irregularities, damage or porosity present in the composite can significantly change the dielectric properties [133]. The outcome of these asperities gives rise to different conductivity levels throughout the sample. Furthermore, dielectric strengths drastically decrease with temperature and when the rate of heat input exceeds heat removal rate, accelerated thermal breakdown of the epoxy occurs [134, 135]. The impurities present near the vicinity of carbon–fiber epoxy interface will cause severe dielectric decomposition, which leads to reduction of bond strength.

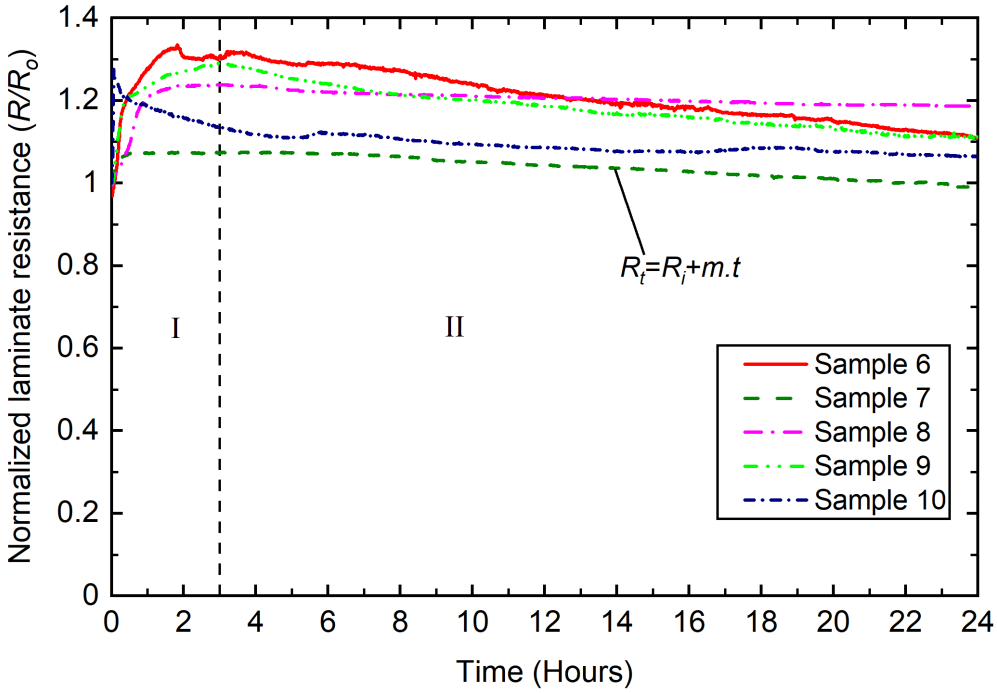

Figure 9: Normalized laminate resistance history of coupon samples exposed to 0.22 A/mm^2 direct current for 24 hours. R is the resistance at any given time and R_o is the initial resistance of the laminate. R_t and R_i represent normalized resistance at any given time after 3 hour mark and the normalized resistance intercept along the line $t = 3$ hours respectively.

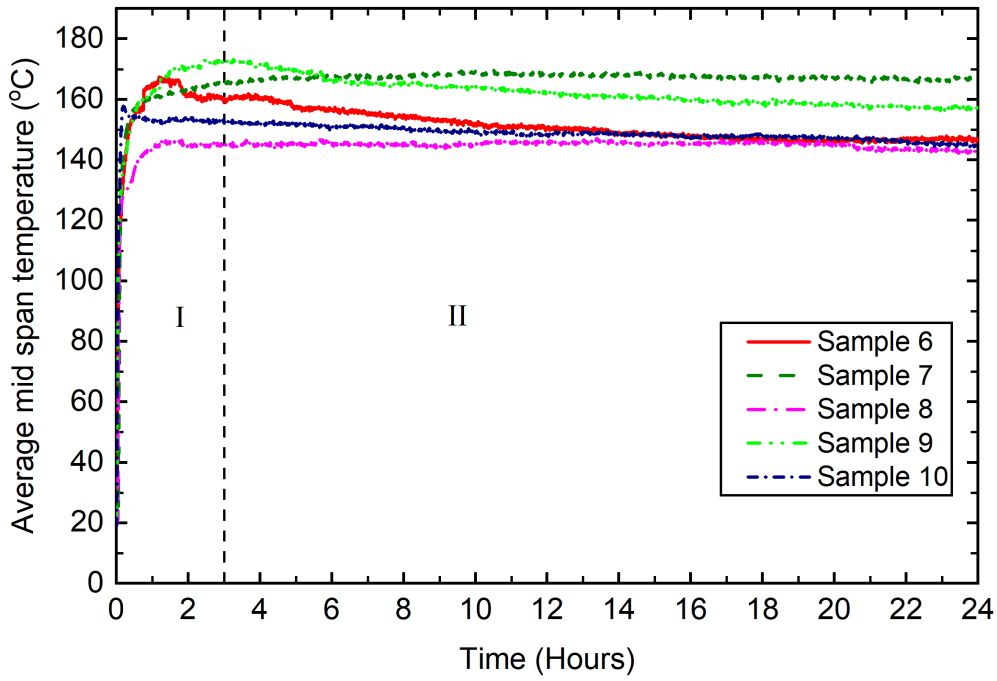

Figure 10: Average laminate mid span temperature variation for coupon samples exposed to 0.22A/mm^2 direct current for 24 hours.

The resistance variation with time for identical samples exposed to 0.22 A/mm^2 direct current for 24 hours is depicted in Fig. 9. All samples showed an increase in resistance over time and gradual reduction until steady state was obtained. The initial increase in resistance is due to the permanent material changes which can also be observed in cyclic tests, which is explained later. Phase I shows a gradual increase in resistance until dielectric breakdown occurs leading to a decrease in resistance. When epoxy degrades near the interface, more fibers come in contact with each other, causing a reduction in resistance and surface temperature, which can be observed in Fig. 10. Steady state is acquired when dielectric breakdown occurs near the carbon fiber–epoxy interface and all the pathways for electric current are explored. Since CFRP exhibits positive temperature coefficient effect of resistivity behavior, as the temperature decreases, resistance also decreases. All samples had a linear relationship with resistance in phase II of the resistance plot, which can be formulated as,

$$R_t = R_i + m \cdot t$$

where, R_t is the normalized resistance at any given time after 3 hour mark, R_i is the normalized resistance intercept along the line $t = 3$ hours, m is the slope of the normalized resistance lines and t is the time in hours. The slope varies from -0.009 to -0.003 for samples 6–10. The negative slope indicates a steady decrease in resistance in all the samples, which is an effect of diminished Joule heating due to discovery of new pathways for current flow.

In order to understand the mechanisms of damage accumulation, which is revealed by resistance change, cyclic tests have been performed on five identical samples. Figure. 11 shows the variation of laminate resistance change for cyclic loading of three hours for these samples. Figure. 12 shows the normalized resistance variation of sample 11 which is subjected to cyclic loading. From Fig. 12 it is evident that the steep increase in resistance in all the cycles is from Joule heating of the conductive pathways. The change in resistance (start

of cycle to the end of cycle) of the first, second and third cycles are 0.27, 0.18 and 0.14 Ω/Ω respectively. We can interpret the physical damage accumulation through resistance change of the material over every cycle, a change in initial resistance of 0.16 Ω/Ω between the first and second cycle can be noticed, but when second and third cycles are compared, a change in initial resistance of 0.06 Ω/Ω is observed. This indicates a permanent change in physical material characteristics which is due to thermal mismatch induced damage resulting in delamination of the plies. Due to the absence of temperature effects at the initial point, this permanent increment in starting resistance for every cycle signifies the level of electrical degradation and validates the above conclusion. Since the fibers are not affected by this low-density current, this notable distinction is a phenomenon pertaining to reorganization of conductive paths caused by micro-scale delamination between the plies. From Fig. 11, it can be observed that majority of the samples had a permanent increase in resistance except for sample 13, where dielectric breakdown has occurred in the second and third cycles resulting in stabilization and also a steep reduction in apparent damage accumulation.

The temperature changes for every one-hour cycle of the same sample is shown in Fig. 13 shows. Time taken to achieve 63% of the steady state in the first cycle is approximately 3.3 minutes, whereas in the second and third cycles it takes 3 minutes and 2.8 minutes, respectively. Since current is constant, heat generated in the sample is directly proportional to the resistance. An increase in resistance increases the heat generated per unit time, which reduces the time taken to achieve steady state.

Table 4: Glass transition temperature (T_g) and $\tan\delta$ variation for different exposures.

Specimen type	T_g (°C)	Reduction (%)	$\tan\delta$	Increment (%)
Undegraded	166.1 ± 0.4	-	0.22	-
ED-3hrs	160.2 ± 1.3	3.6	0.31	41
ED-24hrs	159.7 ± 2.6	3.8	0.31	41
ED-Cyclic	159.4 ± 1.4	4.0	0.32	45
Oven heated-3hrs	163.7 ± 0.5	1.1	0.26	18
Oven heated-24hrs	163.8 ± 0.5	1.4	0.29	32

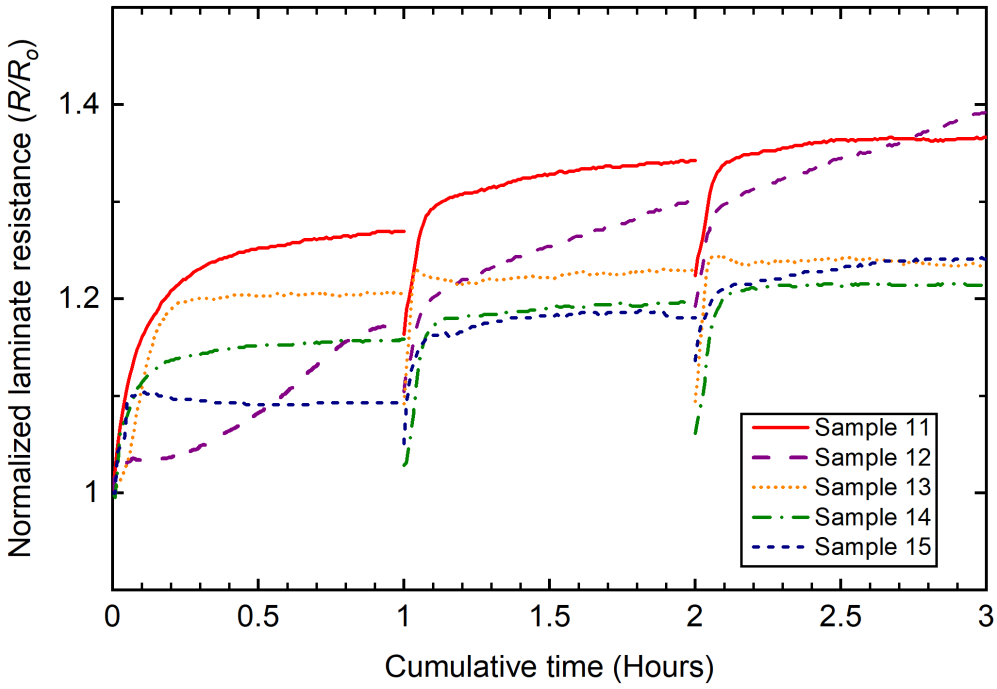

Figure 11: Normalized resistance change of the laminates subjected to three hour cyclic load.

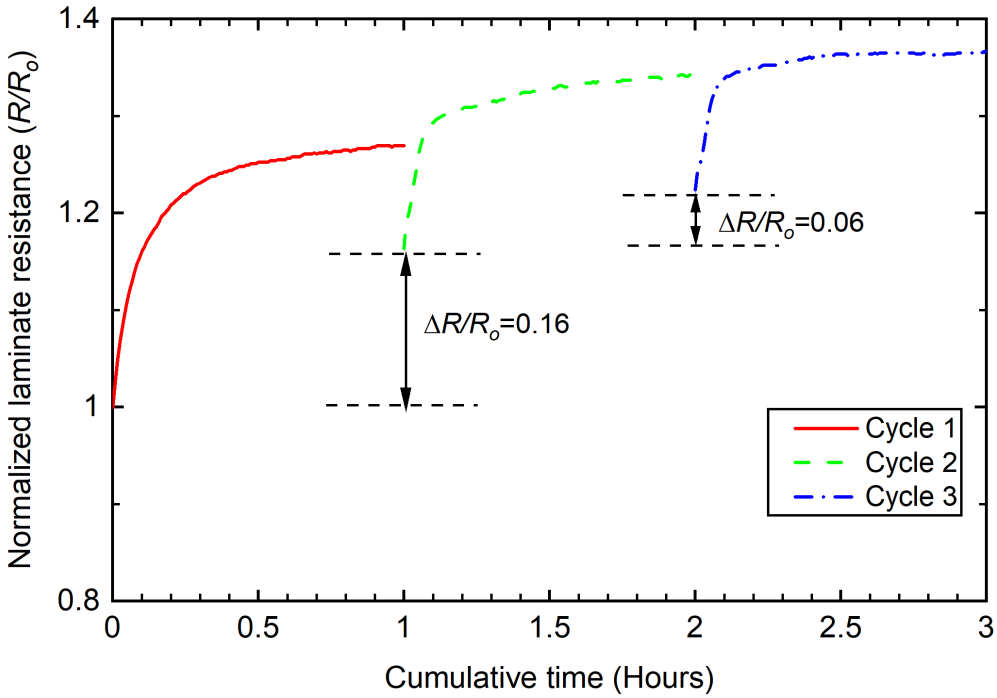

Figure 12: Normalized resistance change of the sample 11 subjected to three hour cyclic load. $\Delta R/R_o$ represents the increase in normalized laminate resistance from previous cycle.

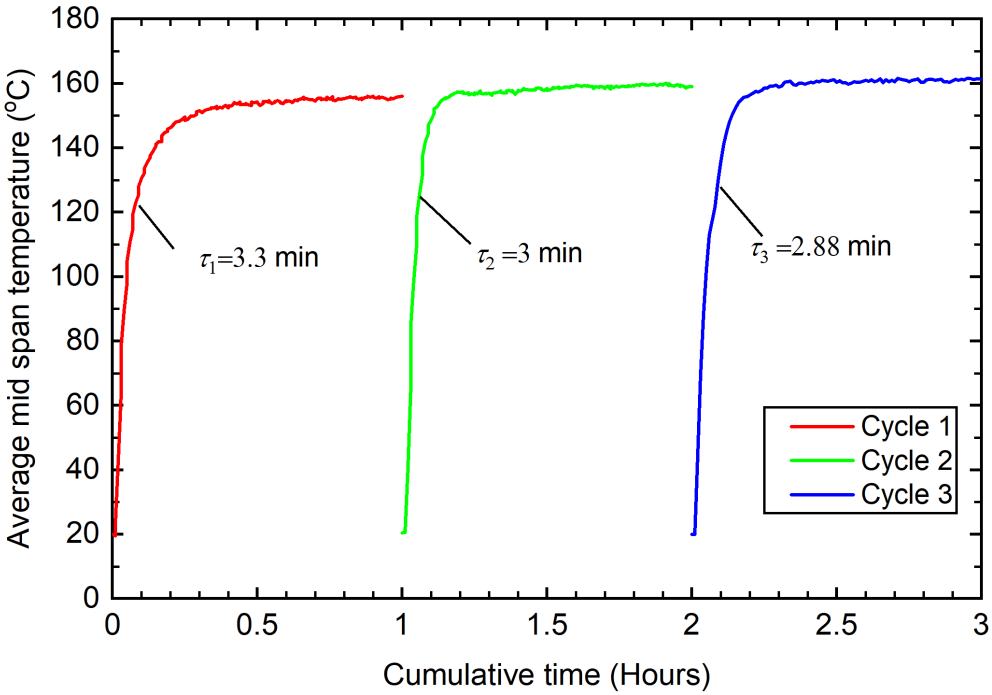

Figure 13: Variation of average mid span temperatures of the sample 11 for three hour cyclic load. Here, τ (time constant) represents the time taken to achieve 63% of the steady state temperature in their respective cycles.

Table 5: Compressive strength variation for different exposures.

Specimen type	Compressive strength (MPa)	Reduction (%)
Undegraded	755 ± 33	-
ED-3hrs	643 ± 22	14.9
ED-24hrs	646 ± 24	14.4
ED-Cyclic	657 ± 36	13.0
Oven heated-3hrs	721 ± 10	4.5
Oven heated-24hrs	691 ± 31	8.5

Table 5 shows the comparison of compressive strengths of samples exposed to various conditions. A significant amount of difference in ultimate compressive strengths between undegraded, electrically degraded and oven heated samples is evident when reduction percentage is analyzed. The percentage difference between the mean values of electrically degraded (ED) and undegraded samples is (13–14.9%). This variation corresponds to the irreversible degradation by electrical conduction due to electrothermal effects. Considerable difference of about 10.4% can be noticed between electrically degraded (ED-3hrs) and oven heated

(Oven heated-3hrs) samples. This difference in compressive strengths was reduced to 5.9% when samples exposed to 24 hours (ED-24hrs and Oven heated-24hrs) were compared. We can conclude that electrical degradation cannot be accounted by thermal effects of the direct current alone and dielectric effects have an important role in reducing the strength. From ED-cyclic data we could interpret that there is a progressive damage accumulation over time and, we can exclusively estimate the effects of electrothermal effects by comparing oven treated samples with ED samples. The absence of notable differences between compressive strengths, T_g and, $\tan\delta$ values for ED-3hrs, ED-Cyclic, and ED-24hrs experiments demonstrates that electrical degradation occurs very early under these conditions and dielectric degradation continues as long as it is exposed to electric current, but the damage accumulation is minimal.

Table 4 shows the T_g values obtained for samples exposed to direct current and isothermal conditions in an oven. The reduction in compressive strengths support the T_g values when percentage difference is examined. A (3.5–4.0%) reduction in T_g can be observed for electrically degraded samples. This supports the reduction in compressive strengths and concludes that dielectric degradation will have minimal effects which are restricted around the conductive paths, and any further degradation can be attributed to thermal effects caused by heating of fibers. Although the temperature was below T_g, an increase in storage modulus was observed in electrically degraded and oven heated samples. This increase is associated with physical aging of the amorphous phase and densification of the polymer network occurring at temperatures below T_g [136]. Since the oven heated composites experience the same temperature, the further reduction of T_g as seen in electrically degraded samples compared to oven heated samples can be associated with severe delamination of the carbon fiber plies and debonding near the interface.

It is evident from Fig. 14 and Table 4 that the $\tan\delta$ values are increasing after passage of electricity, an increment of (41–45%) is observed for ED samples. This indicates the

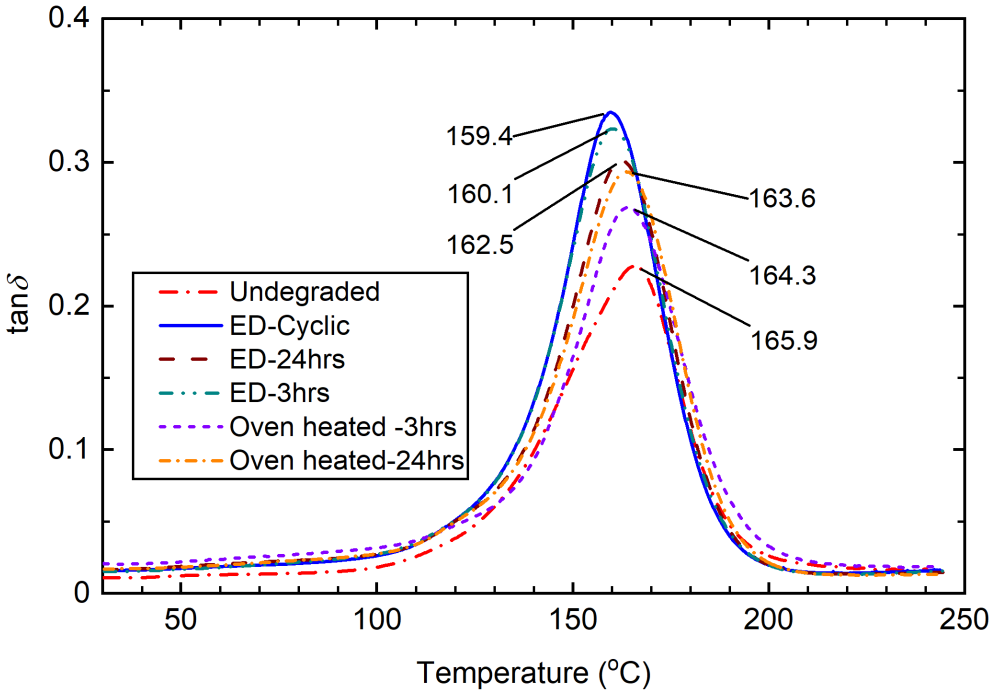

Figure 14: T_g and $\tan\delta$ variation for different exposures.

material has more energy dissipation potential which is inversely proportional to the load carrying capacity. The $\tan\delta$ values of the undegraded samples and ED-3hrs are 0.22 and 0.31, respectively. The increase in damping factor also implies a reduction in the carbon fiber–epoxy interface bonding which depends on the mobility of the molecular chains at the interface [137]. Furthermore, since the fibers have negative CTE and the epoxy has a positive CTE, significant amount of thermal stresses will be developed at the interface during heating and consequent cooling. These residual thermal stresses caused by thermal mismatch will be higher for the case of electrically degraded samples compared to oven heated samples due to resistive heating nature of the fibers.

The Cole–Cole plots of three electrically degraded (ED-3hrs, ED-24hrs), cyclically degraded (ED-Cyclic), and undegraded samples are shown in Fig. 15. Here, the loss modulus (E'') values are plotted against storage modulus (E') on a logarithmic scale. An imperfect or a semi ellipse indicates heterogeneity and good fiber–matrix interface, while a perfect semicircle exhibits a pure polymer [138]. A notable difference in the shape of the Cole–Cole plots

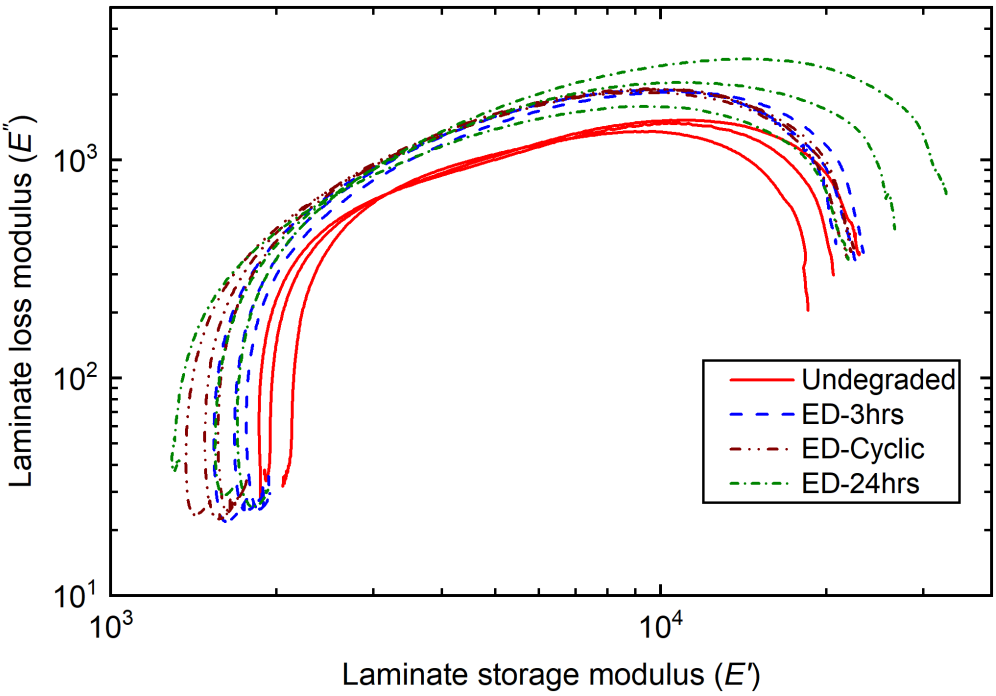

Figure 15: Cole–Cole plots for Undegraded, ED-3hrs, ED-Cyclic, and ED-24hrs samples.

between undegraded and ED samples can be observed. The shape of the Cole–Cole plots become more semicircular after passing electricity, which indicates weaker adhesion due to dielectric breakdown and debonding at the carbon fiber–epoxy interface. Due to indistinguishable shape of Cole–Cole plots of ED-cyclic and ED-3hrs, we can conclude that electrical degradation in CFRP is an irreversible phenomenon and accumulates over time.

Table 6 shows the permanent resistivity changes along the transverse, longitudinal and through-thickness directions for different exposures. Indication of delamination is evident in all samples considering the increment of resistivity in through-thickness direction. However, electrically degraded samples experienced more damage as compared to oven-heated samples due to Joule heating, subsequent decomposition of surrounding polymer and the development of matrix cracks due to electron hopping between parallel fibers. Nevertheless, a decrease in through-thickness resistivity was observed when ED-Cyclic and ED-24hrs are compared, this can be attributed to dielectric breakdown taking place for prolonged exposure that causes more fibers to come into contact. However, transverse and longitudinal

resistivities showed different behavior where oven-heated samples experienced an increase in resistivity suggesting delamination and increased waviness from pure thermal damage but in electrically degraded samples a slight decrease in resistivity was observed, supporting the dielectric breakdown of polymer which results in retaining the conductive paths formed during degradation. The initial thermal damage from Joule heating causes severe delamination, but due to dielectric breakdown of the polymer from elevated temperature, the resistivity of the material decreases as the polymer becomes conductive overtime. This phenomenon is supported by longitudinal resistivity of ED-24hrs and ED-Cyclic samples. Table 7 also shows the variation of Young's modulus of the samples in thickness direction. A decrease in modulus was observed in all cases when undegraded samples are compared to degraded samples. However, the modulus of electrically degraded samples was lower than thermally degraded samples, a similar trend was observed for reduction in compressive strengths.

Table 6: Resistivity measurements at the mid span of the samples for different exposures.

Specimen type	Transverse resistivity (Ω-mm)	Longitudinal resistivity (Ω-mm)	Through-thickness resistivity (Ω-m)
Undegraded	1.49 ± 0.08	1.50 ± 0.03	0.45 ± 0.02
ED-24hrs	1.36 ± 0.05	1.46 ± 0.02	3.72 ± 0.32
ED-Cyclic	1.35 ± 0.04	1.58 ± 0.05	4.95 ± 1.58
Oven heated-3hrs	1.64 ± 0.06	1.74 ± 0.07	1.40 ± 0.14
Oven heated-24hrs	1.75 ± 0.06	1.77 ± 0.08	1.50 ± 0.04

Table 7: Young's modulus measurements at the mid span of the samples for different exposures.

Specimen type	Through-thickness Young's modulus (GPa)
Undegraded	0.45 ± 0.02
ED-24hrs	3.72 ± 0.32
ED-Cyclic	4.95 ± 1.58
Oven heated-3hrs	1.40 ± 0.14
Oven heated-24hrs	1.50 ± 0.04

The sectional views of X-ray CT scans of a cross-ply Undegraded, Oven heated-24hrs and ED-24hrs samples are shown in Fig. 16. Here, the 0° fibers are coming out of the picture and the current was passed along these fibers. Interply damage leading to delamination

is visible in Oven heated-24hrs and ED-24hrs samples as seen in Fig. 16b and 16c. The interply damage in the case of Oven heated-24hrs sample is caused by matrix decomposition and thermal mismatch between the 0° and 90° plies. However, for the case of ED-24hrs, the interply damage is a combination of thermal effects resulting from dielectric breakdown and matric decomposition. The in-plane views of Oven heated-24hrs and ED-24hrs samples are depicted in Fig. 17a and 17b respectively. Here, the current carrying fibers are running from left to right. Severe delamination due to damage accumulation is visible between 0° and 90° plies in Fig. 17b. From the in-plane view it is revealed that the 0° plies are the most affected as a consequence of debonding and dielectric breakdown. In addition to this, electrically degraded samples also experience matrix decomposition due to the heat generated by Joule heating of the carbon fibers.

2.3 Conclusion

In this study the results for mechanical strength degradation of CFRP laminates due to low-density direct current and the mechanisms involved have been presented. Application of direct current in CFRP encompasses major challenges: (i) electrical setup, (ii) sample preparation, (iii) temperature and resistance measurement, (iv) contact resistance, and (v) dimensional changes while passing current. This study overcomes these challenges via developing a robust experimental setup, capable of passing uninterrupted current and adjusting to dimensional changes while simultaneously capturing temperature and voltage data. Samples were carefully examined for orthogonality and minimal contact resistance was ensured by applying conductive paste. Joule heating of carbon fibers played an integral part in varying the resistance and temperature of the CFRP sample. Effective edge contact between the fixture and specimen was critical for obtaining consistent results. Since, contact resistance heating has an adverse effect on the temperature profile at the edges, mid span of the specimen was analyzed. Experimental results show that the electrical degradation in CFRP is a cumulative effect of thermal and electrical effects and the damage occurs very early under

these circumstances. A permanent change in physical material characteristics was captured by cyclic tests which showed the level of degradation over time. The observed degradation is caused by the following phenomenon, thermal decomposition of the epoxy due to resistive heating, dielectric breakdown at the carbon fiber–epoxy interface and thermal mismatch during heating and cooling of the laminates. Compression test results showed an average percentage decrease of (13.0–15%) in ultimate compressive strengths from electrical degradation. Electrically degraded samples also had a reduction of (6–7%) in Young's modulus in the thickness direction. The electrothermal degradation at the carbon fiber–epoxy interface has resulted in reduction of glass transition temperatures (3–4%) and the increment of $\tan\delta$ values (41–45%). The through-thickness resistivity measurements showed the extent of delamination in degraded samples and in-plane resistivity changes revealed the effects of Joule heating and subsequent reduction of resistance due to dielectric breakdown of polymer leading to a more conductive but degraded sample over time. CT scan images showed the extent of damage accumulated in electrically degraded samples is a combination of dielectric breakdown between plies that led to delamination and matrix decomposition caused by the heat generated due to Joule heating of carbon fibers.

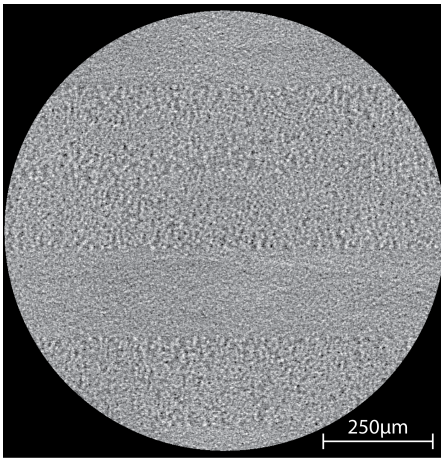

(a)

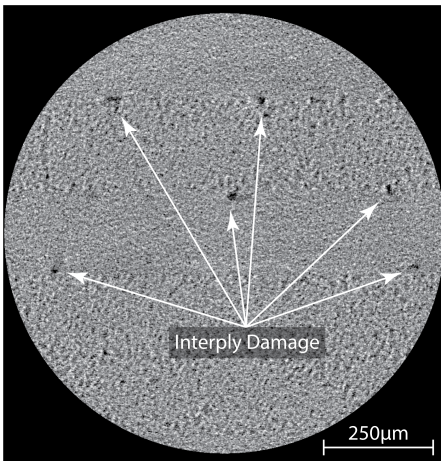

(b)

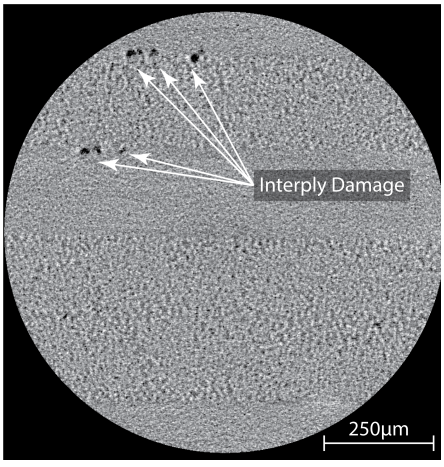

(c)

Figure 16: CT scans of cross-ply Undegraded, Oven heated-24hrs and ED-24hrs samples. Here, (a), (b) and (c) represent the sectional views of Undegraded, Oven heated-24hrs and ED-24hrs samples respectively. Interply damage leading to delamination between the plies is visible in both Oven heated-24hrs and ED-24hrs samples.

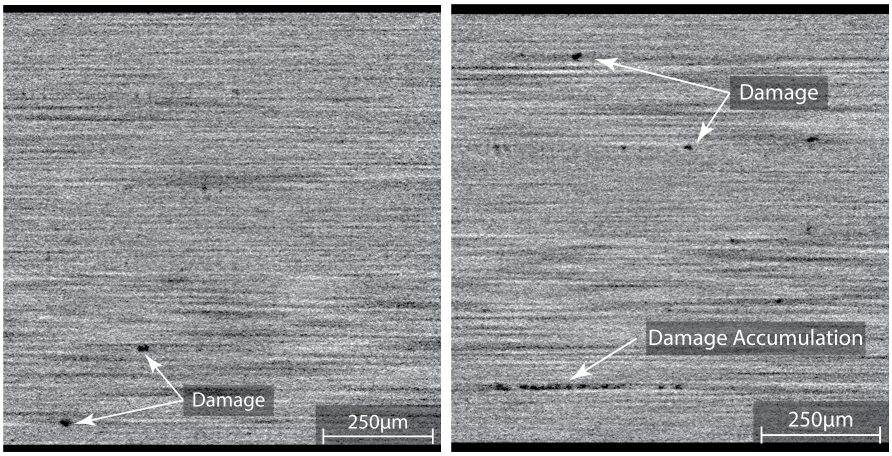

(a) (b)

Figure 17: In-plane views of CT scans of a) Oven heated-24hrs and b) ED-24hrs samples. In both cases thermal damage is visible, but in the case of electrically degraded sample, damage accumulation due to accelerated thermal breakdown can be noticed between 0° and 90° plies.

CHAPTER III

CHARACTERIZING THE UNIDIRECTIONAL ALIGNMENT OF GRAPHENE NANOPLATELETS (GNPs) IN EPOXY USING IN SITU AC CONDUCTIVITY MEASUREMENTS

In this study, we present an in situ technique of measuring the AC current during the alignment of GNPs in epoxy for various concentrations of GNP and study the effect of electric field strength on alignment and correlate the same to its dielectric properties and through-thickness Young's modulus of aligned composites.

3.1 Materials and Methods

3.1.1 Preparation of aligned GNP/epoxy composites

The purpose of these experiments is to understand the alignment process of higher concentrations of GNPs in epoxy. To achieve this, an electrical setup is designed which consists of two conductive aluminum plates that are connected in series to a wideband amplifier (7602M, Krohnite, Brockton, Massachusetts) and it is connected to an AC signal generator (3312A, HP, Alto California). The amplifier was connected in series to a precision multimeter (5491B, BK Precision, Yorba Linda, California) as shown in Fig. 18a. The minuscule changes in AC current were tracked using LabVIEW software interfaced with the digital multimeter. The schematic is represented in Fig. 18b. This is a commonly used setup for AC alignment of carbonaceous materials [53, 54, 139]. During alignment the AC conductivity was measured

at 10 kHz considering the AC current obtained from the precision multimeter, electric field intensity and dimensions of the cured GNP epoxy sample.

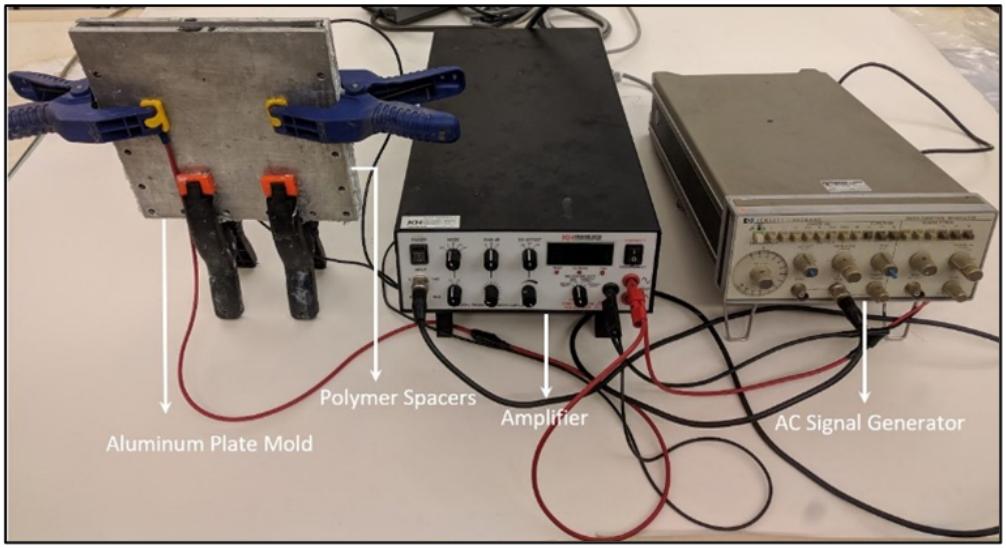

(a)

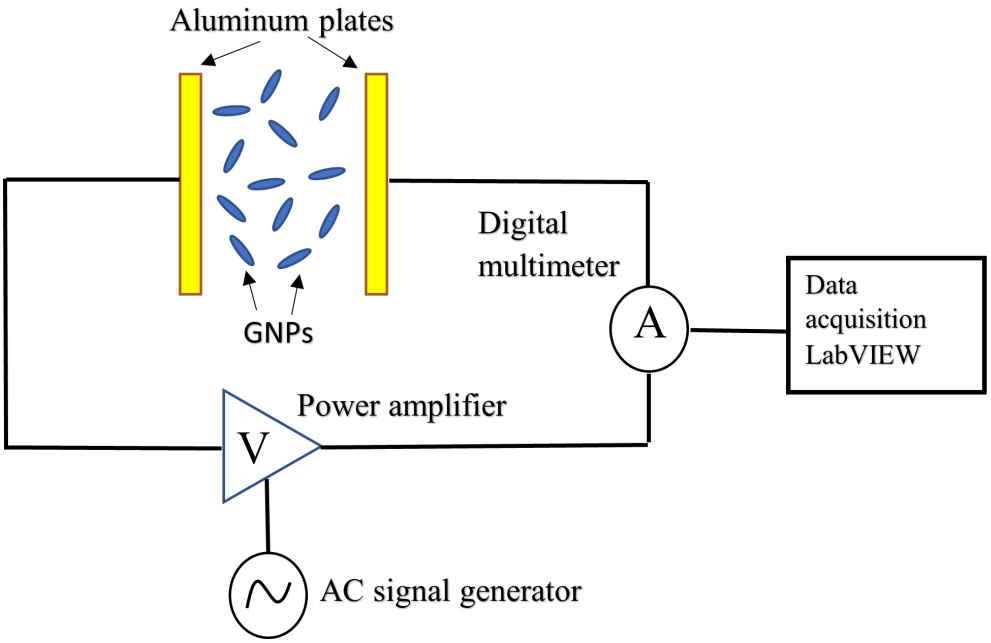

(b)

Figure 18: a) Real experimental setup and b) Schematic of the unidirectional alignment setup.

The GNPs of average diameter of 25 μm were procured from XG Sciences, Lansing, Michigan. They have a average thickness of 6-8 nm and a surface area of 120–150 m^2/g. Epoxy resin (EPON 862) and hardener (EPIKURE 3274) were supplied by Hexion, Columbus, Ohio.

Epoxy and hardener was used as the base polymer for dispersing the GNPs. Epoxy is a low viscosity blend of diglycidyl ether of bisphenol F. The liquid hardener is a low viscosity based aliphatic amine.

GNPs based on weight percent with respect to epoxy and hardener were magnetically stirred for an hour. The GNPs were mechanically exfoliated by passing the mixture through a three-roll mill (T65, Torrey Hills Technologies, San Diego, California) for 15 times at 60 rpm with a roller gap distance of 20 μm. This ensured uniform dispersion of GNPs in epoxy. Stoichiometric ratio of hardener (100:40) was mixed with the epoxy/GNPs mixture according to the manufacturer specifications. The mixture was thoroughly mixed and degassed under vacuum for 30 min. The mixture was poured into a mold made of aluminum plates of size 200 $\times$ 200 mm spaced apart using 3 mm thick insulating polymer strips as shown in Fig. 18a. After the application of electric field the sample was left to cure at room temperature.

Nanocomposites of different weight fractions (0.7, 1.4 and 2.8 wt%) of sample size 150 $\times$ 40 $\times$ 3 mm were aligned at 35 V/mm and 10 kHz, to study the effect of concentration on AC conductivity. Three samples of each were aligned to test repeat-ability. After correlating the AC conductivity data for different concentrations, the effect of electric field was studied. Two samples of similar size were aligned at (25, 35, 45 and 55 V/mm at 10 kHz) electric field intensities for 1.4 wt% concentration. Apart from this, to study the effect of brownian motion on alignment of GNPs, one sample of 1.4 wt% was subjected to an on and off 5 minute cycles of 35 V/mm at 10 kHz electric field intensity for 70 minutes. Finally, the growth of electrical conductivity was studied on 1.4 wt% GNPs at 35 V/mm at 10 kHz. Here, alignment was performed for a specific time (5, 10, 15, 20, 25, 30 ,40, 50, 60 and 70 minutes) and the samples were left to cure at room temperature for 24 hours prior to electrical testing.

3.1.2 Material Analysis and Characterization

Dynamic viscosity of the epoxy with inclusions of GNPs for 0.7, 1.4 and 2.8 wt% concentrations were measured before alignment using a viscometer (LVDVE, Brookfield, Middleboro, Massachusetts) according to ASTM-D2196. After the samples were cured in the aluminum mold, 5 samples of size 10 × 10 × 3 mm were cut from each aligned and unaligned samples using a precision saw. The samples were lightly sanded using 800 grit sandpaper prior to applying electrically conductive silver epoxy paste (Duralco 120, Cotronics, Brooklyn, New York). This ensured uniform electrical contact for electrical testing.

The Young's modulus was measured for both aligned and unaligned samples using a negative square wave pulse-receiver (5077PR, Panametrics, Waltham, Massachusetts). The ultrasonic machine was connected to an oscilloscope (3052, Tektronix, Beaverton, Oregon). The ultrasonic sound wave propagation was measured in the through-thickness direction. Parameters such as density of the sample, and the shear wave and longitudinal wave speeds were used to calculate the Young's modulus.

Dielectric properties were obtained along the through-thickness direction by dielectric spectroscopy using a potentiostat (VersaSTAT 3F, Ametek, Berwyn, Pennsylvania). The frequency was varied from 1 Hz to 1 MHz. Dielectric constant, dielectric loss and AC conductivity were calculated using standard formulations as follows [140].

$$\varepsilon_r^{'} = \frac{-Z''}{2\pi f \varepsilon_o((Z')^2 + (Z'')^2)} \frac{l}{A} \tag{3.1.1}$$

$$\varepsilon_r^{''} = \frac{Z'}{2\pi f \varepsilon_o((Z')^2 + (Z'')^2)} \frac{l}{A} \tag{3.1.2}$$

$$\sigma_{AC} = 2\pi f \varepsilon_o \varepsilon_r^{''} \tag{3.1.3}$$

Here, $\varepsilon_r^{'}$ is the dielectric constant, $\varepsilon_r^{''}$ is the dielectric loss, σ_{AC} is the AC conductivity, ε_o is the permittivity of free space, f is the AC frequency, l and A are sample thickness and surface area respectively and Z' and Z'' are the real and imaginary components of impedance, respectively.

3.2 Results and Discussion

3.2.1 Mechanics of unidirectional GNP alignment

The mechanics of a single GNP/GONP which is surrounded by a dielectric fluid experiencing an external electric field are well documented [53, 59, 63]. The electric field results in the formation of dipoles due to migration of the electron cloud over the sheets of graphene, given that the electrical properties of epoxy differ from that of graphene. It should be noted that the polarizibility of graphene is significantly higher in the in-plane direction as compared to perpendicular direction due to its physical architecture. The resultant dipole moment produces a rotational torque about the center of GNP which is opposed by the viscous torque produced by the liquid epoxy. The resultant torque is responsible to orient the GNP towards the electric field and it is dependant on GNP dimensions, electric field intensity, viscosity and the dielectric constant of the epoxy. The time required for a GNP to orient itself from an initial angle θ_o to a final angle $\theta^{'}$ was devised by Wu *et al.* and is given by the following equation [53]. The schematic of a GNP experiencing an electric field is depicted in Fig. 19.

$$t_r = \frac{1}{A} ln \frac{\tan\theta_o}{\tan\theta'} \tag{3.2.1}$$

Here,

$$A = \frac{\pi}{8\eta} \frac{\varepsilon_m}{\left(\frac{\pi}{2} - \frac{b}{a}\right)} E_o^2 \tag{3.2.2}$$

Here, A is a constant that depends on the viscosity (η) and dielectric constant of the epoxy

(ε_m). It is also varies with electric field intensity (E_o), half thickness (b) and radius of GNP (a).

After the platelets orient themselves towards the electric field direction, they tend to attract towards each other due to the presence of opposite charges on adjacent particles. This translation movement is resisted by translational viscous force acting on the particle due to the epoxy. The translation movement of these particles results in chain formation from one end of the electrode to the other. The schematic of a two GNPs experiencing attraction forces fro the dipole formation due to electric field is depicted in Fig. 20. The time required for end-to-end connection was also devised by Wu *et al.* for GNPs and it is given by the following equations [53].

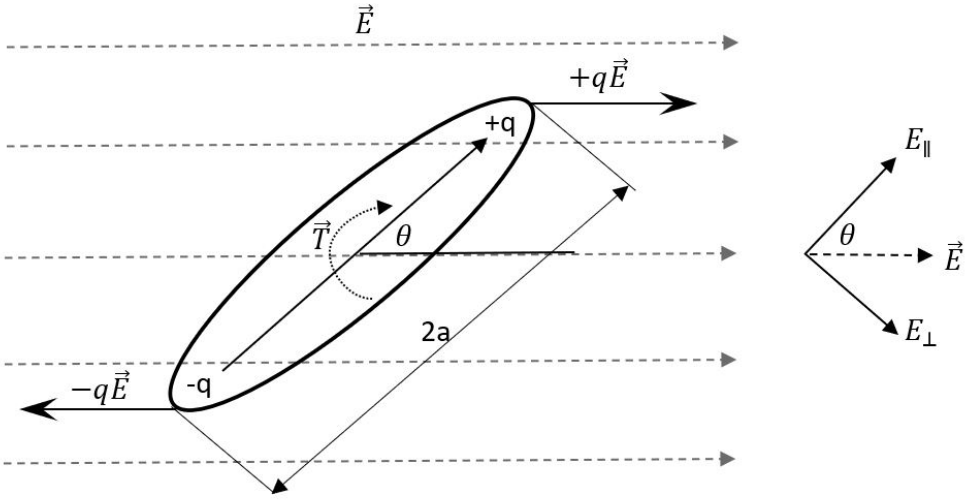

Figure 19: Schematic of a GNP experiencing an electric field $\vec{E}$.

$$t_c = \frac{2x_o^3}{3B} \tag{3.2.3}$$

Here,

$$B = \frac{4\pi a^4}{9\eta k_t \varepsilon_o} \frac{E_o^2 \varepsilon_m^2}{\left(\frac{\pi}{2} - \frac{b}{a}\right)^2} \tag{3.2.4}$$

and,

$$x_o = \frac{1}{\rho}\frac{m_G}{W_G}\frac{1}{4a^2} \tag{3.2.5}$$

Here, t_c is the translation time of the particles, k_t is the translational friction coefficient that depends on the surface area of GNP. The initial perpendicular distance between two adjacent particles x_o depends on the density of the epoxy (ρ), weight fraction of GNPs (W_G), mass of GNP (m_G) and radius of GNP (a). The mass of GNP (m_G) is calculated to be around 2.65 $\times 10^{-14}$ kg for a M25 GNP particle [53]. The radius of the platelet is 12.5 μm. The combined density of epoxy-hardener system was calculated to be around 1.1 g/cm^3. Also, B is a constant that varies with viscosity and dielectric constant of the epoxy, aspect ratio of GNP, translational friction coefficient and electric field strength.

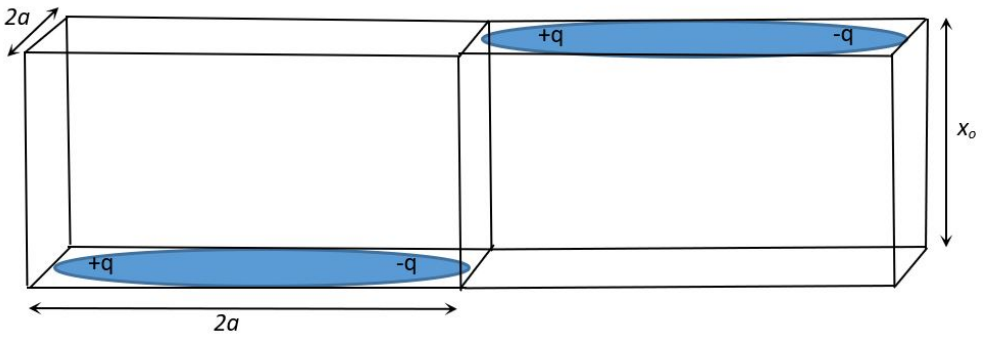

Figure 20: Schematic of two GNPs experiencing dipole attraction after aligning towards the electric field $\vec{E}$.

It is assumed that perfect dispersion takes place and translation happens after the particles are aligned along the electric field. Table 8 shows the variation of rotation time and translation time of GNPs in epoxy based on the experimentally calculated viscosity of the mixture for weight concentrations of 0.7, 1.4 and 2.8 wt%. Although an increase in viscosity increases the time required for chain formation due to increase in viscous forces with concentration, the reduction of proximity of particles ultimately reduces the translation time. It is interesting to note that the translation time decreases drastically as the concentration

of GNP is increased and it is also significantly lower than the rotation time. This shows that translation of GNP is prone to happen prior to rotation and thus making the overall alignment behavior complex. The assumed frictional forces are no longer valid as particles tend to agglomerate and they posses different dipole moments and rotational dynamics [54]. It should also be noted that multiple particle interactions must be considered if the distance between particles is less than the particle diameter (here, the GNP diameter is 25 μm) and the forces acting on the particles are a function of dielectric constant of the epoxy and GNPs [141]. Considering these different criteria, frictional forces acting on the group of particles are not in-line with theoretical predictions of Wu's model when higher concentrations of GNP are considered. In addition to this, viscosity of the system plays an important role in determining the alignment time due to increased particle to particle interactions from the close proximity of GNPs. The increment in rotation time with concentration due to the added effects from viscosity is shown in Table 8. Regardless of the increased rotation time, the total alignment time is expected to be higher due to the complex behavior of different sized GNP agglomerates under an electric field. Hence, a semi-empirical approach is needed to characterize the alignment process for higher weight fractions. Here, higher weight fractions refers to systems where the distance between particles x_o is less than the particle diameter ($2a$). Taking these factors into account, the new model encompasses the indirect effects of viscosity by considering the inter particle distance of GNPs in the mixture. If the distance between the particles x_o is more than the particle diameter ($2a$), additional viscous forces are not generated by particle-particle interaction and viscosity of epoxy and hardener system can be used directly. The next section explains the significance of AC conductivity measurements to capture the complex alignment behavior in the bulk system.

3.2.2 AC conductivity results

Long duration alignment experiments were performed on epoxy and epoxy/GNP samples to determine the effects of alignment, GNP inclusions and curing on the resulting AC con-

Table 8: Rotation time, translation time and spacing between the GNPs predicted using the model proposed by Wu *et al.* [53].The inputs into the model are GNP wt% and experimentally determined viscosity (mPas).

GNP wt%	Viscosity (mPas)	Rotation time (min)	x_o (μm)	Translation time (sec)
0.7	1040	22	5.5	0.77
1.4	1400	30	2.7	0.13
2.8	1900	42	1.3	0.02

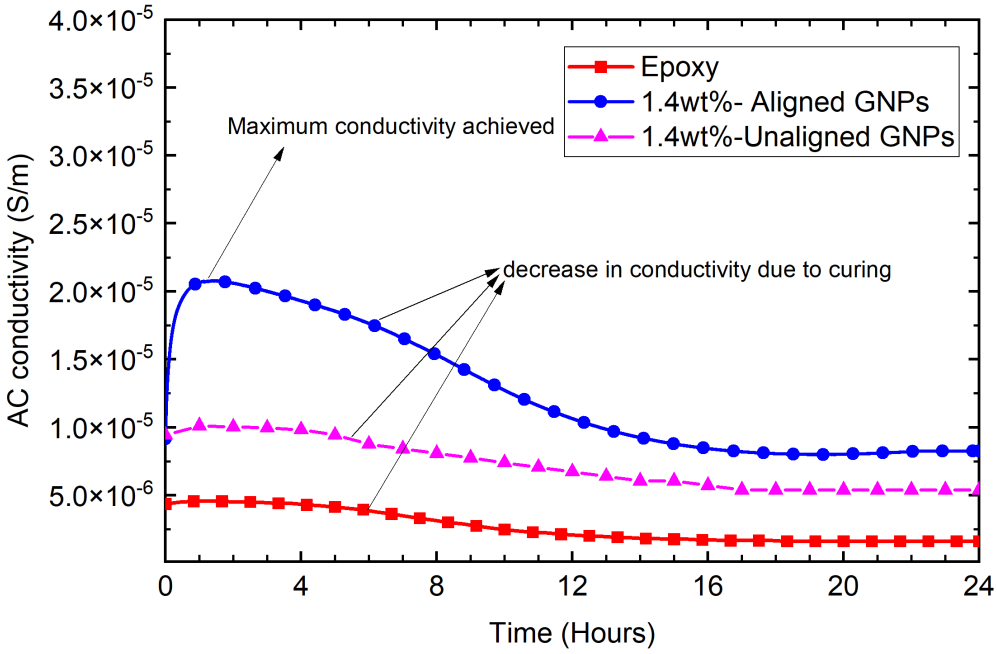

Figure 21: Variation of AC conductivity for 1.4 wt% GNP and epoxy at 35 V/mm during alignment for 24 hours. Measurements for Unaligned 1.4 wt% GNPs in epoxy was taken at intervals of 1 hour for 24 hours. The sampling rate was 40 samples/second, here every 2000^{th} data point is represented except for unaligned sample, where data was taken every hour.

ductivity. The AC conductivity variation for 1.4 wt% of GNP in epoxy which is exposed to an electric field intensity of 35 V/mm at 10 kHz for 24 hours is depicted in Fig. 21. A steep increase in AC conductivity is observed for the first one hour and gradual decrease in AC conductivity for the next 12 hours was noticed and this stabilizes until the end of 24 hours. The initial increase in AC conductivity is primarily due to orientation of particles and subsequent formation of conductive chains which causes an increase in current flow. The flow of current is dictated by the contact conductance with possibility of electron hopping, inter layer conductance of GNP and conductance along the graphene layers [142]. As more

GNPs align towards the electric field and come in contact with other, percolated chains are formed which increases the overall conductivity of the sample. A maximum point is achieved which can qualitatively signify the maximum number of chains possible and further decrease in AC conductivity can be attributed to curing of the epoxy which increases the viscosity making the system less compliant to the flow of electricity.

Figure. 21 also shows the AC conductivity variation for an unaligned 1.4 wt% GNP sample. Due to the possibility of alignment, the measurements were taken at an interval of an hour for 24 hours. Here, we notice a slight increase in AC conductivity between 1–2 hour mark which can be attributed to the exothermic reaction of the cross linking of the epoxy with the hardener that reduces the viscosity of the system and enabling slight increase in current. Similar behavior can be noticed for epoxy which does not contain GNPs. Since the crucial effects of alignment is achieved during the first hour of electric field application, we narrowed the observations of AC conductivity for further experiments to 60–70 minutes.

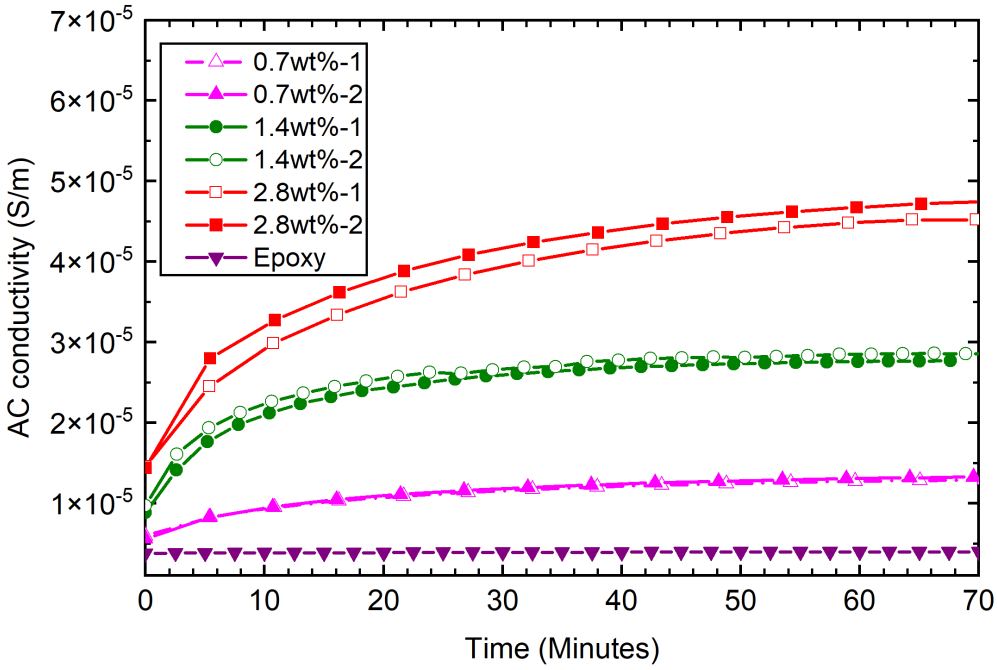

Figure 22: Variation of AC conductivity for different weight fractions of GNP in epoxy. Two samples are depicted to show repeatability.

The AC conductivity variations obtained during the alignment process for various GNP

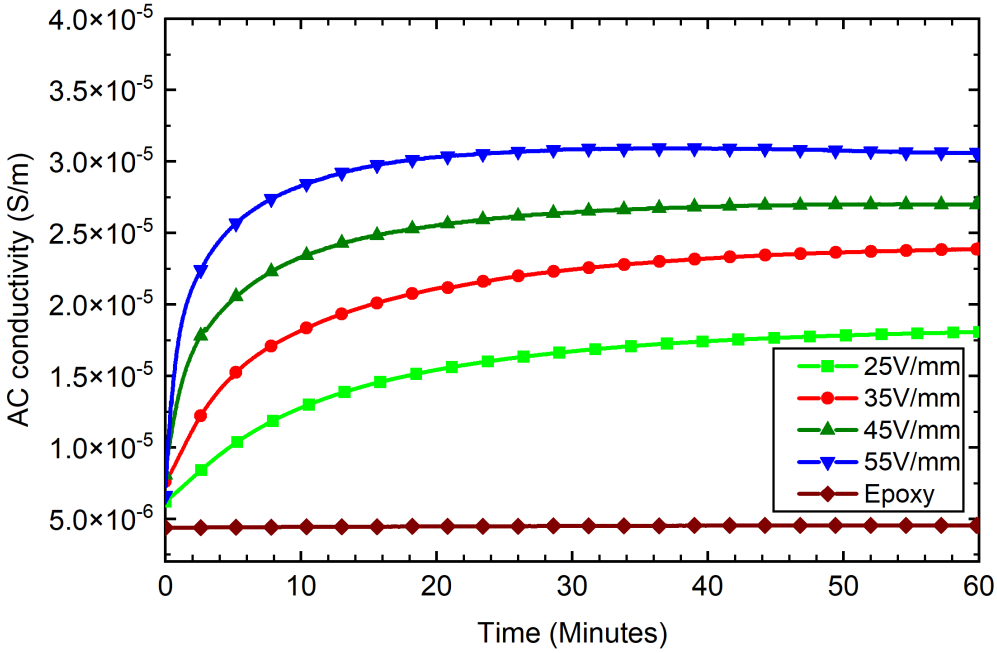

Figure 23: Variation of AC conductivity for 1.4wt% GNPs in epoxy exposed to different intensities of electric fields.

concentrations (0.7, 1.4 and 2.8 wt%) are shown in Fig. 22. Two curves are depicted for each concentration to show repeat-ability of the experiments. Initially, prior to alignment, the conductivity depends on the concentration of the GNP in the system. As alignment occurs, particles rotate and translate to form conductive chains which allows more current to flow through the system. Each concentration of GNP has a distinct curve and the conductivity over time is a function of the amount of particles present and number of conductive chains formed which would be higher for 2.8 wt% compared to 0.7 wt%. We can also notice that the AC conductivity curves tend to plateau after a certain time signifying maximum conductivity increase possible. The maximum conductivity qualitatively implies the number of conducting channels and orientation of GNPs. Any further application of electric field would have negligible effect on the already formed conductive chains. According to the study performed by Wu *et al.*, variation in GNP concentration should not affect the time for alignment as the viscosity is considered to be constant which defines the rotation time and the process of alignment should be completed in 20 minutes. However, from Fig. 22 it is evident that the process of alignment is incomplete at 20 min mark and needs more time

depending on the concentration of GNPs. As concentration increases, the time required to achieve this maximum value of conductivity increases implying the effects of viscosity as shown in 8, increased particle to particle interactions and additional time required for effective rearrangement of chains. When chaining process takes place earlier than rotation, the dipoles close to each other gets disrupted leading to repulsion of the adjacent particles. To reestablish the chains, more time is required to reorient and effective formation of percolated chains.

The effects of various intensities of electric field strength on 1.4wt% GNP in epoxy is presented in Fig. 23. When the electric field intensity is increased, the rotation and translation time decreases in a parabolic form which results in a decrease in the total alignment time. This phenomena can be observed in Fig. 23, where the alignment time for application of electric field intensity of 55 V/mm is noticeably less than 25 V/mm. According to Wu's model, electric field intensity should not affect the quality of alignment but rather the time for alignment [53]. However, we observe that the maximum AC conductivity achieved increases with electric field intensity which implies that more number of percolated chains have been generated. It should be noted that the rotation time calculated from the model is the worst case scenario and majority of the particles take less time to orient themselves along the electric field. Also, the initial orientation of the particles in the system follow normal distribution which indicates 68.2% of particles have an initial angle between 45° and 55°. When particles are capable of rotating faster they form more efficient conductive chains, that can also result in more number of chains due to availability of particles due to decreased agglomeration. This can also be substantiated by considering that the frictional forces increase tremendously when particles bunch together and try to rotate or translate due to their increased surface area which is expected to happen in lower electric fields as their rotation times are relatively lower. This phenomena can be observed for 25 V/mm in Fig. 23. Although, alignment can be completed faster for higher electric fields relative to smaller electric fields, it is imperative to apply the external electric field for 60 minutes

due to brownian motion of GNPs, which distort the orientation of GNPs if the electric field is turned off. This is explained in a later section. and . Maximum level of alignment was assumed to be achieved when the slope of the AC conductivity curve is zero and the rate of change of slope of the AC conductivity curves were determined by Eq. 3.2.6. Based on the predicted time of alignment due to added viscosity effects, 90% of the maximum level of alignment possible was completed for both cases i.e. different concentrations of GNPs and 1.4 wt% GNPs exposed to different electric field intensities.

$$\% \, change = \frac{\frac{\delta \sigma_{AC}}{\delta t}}{(\frac{\delta \sigma_{AC}}{\delta t})_i} \tag{3.2.6}$$

Here, $(\frac{\delta \sigma_{AC}}{\delta t})_i$ refers to the initial slope of the AC conductivity curve.

3.2.3 Dielectric properties of aligned GNP composites

The dielectric constant variations for different weight fractions of unaligned GNPs (0.7,1.4 and 2.8 wt%) with frequency ranging from 1 Hz to 1 MHz is shown in Fig. 24a. For these samples, we noticed a systematic increase in dielectric constant with weight fraction due to increase in number of dipoles which reduces the distance between particles, thereby enhancing the mini-capacitor effect [65]. These capacitors are formed with epoxy acting as the thin dielectric surrounded by GNPs as electrodes. Also, strong interfacial polarization results from the proximity of the particles due to large difference in dielectric constant between the epoxy and GNPs, this effect is known as Maxwell-Wagner-Sillars mechanism (MWS) [91, 92]. Typically, below the percolation threshold, the dielectric constant will not vary with frequency which can be seen in all three unaligned samples.

The dielectric constant variations for different weight fractions of aligned GNPs (0.7,1.4 and 2.8 wt%) with frequency ranging from 1 Hz to 1 MHz is shown in Fig. 24b. Here, we see a significant increase in dielectric constants and they are dependent on frequency which implies

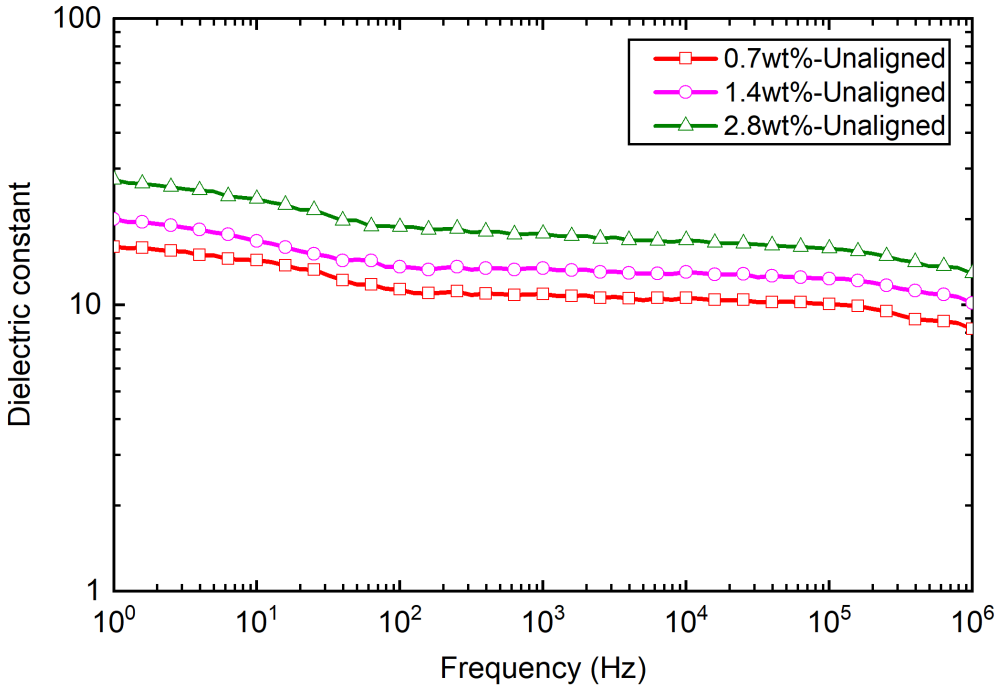

(a)

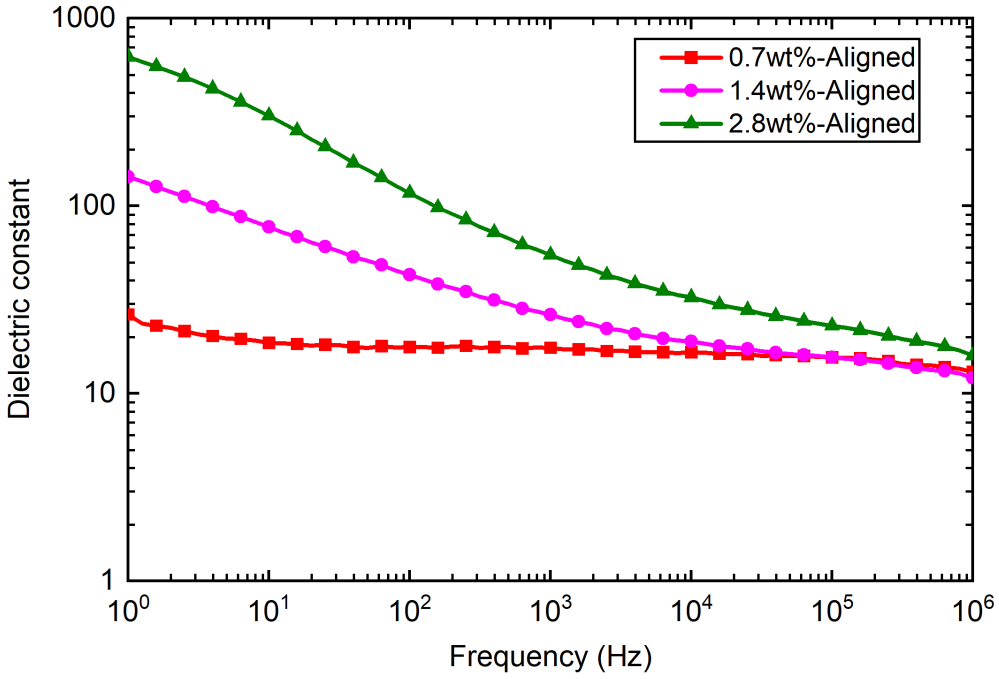

(b)

Figure 24: Dependence of dielectric constant on frequency for a) unaligned and b) aligned GNPs of concentrations 0.7, 1.4 and 2.8 wt% in epoxy. Here, the magnitude of electric field is 35 V/mm at 10 kHz.

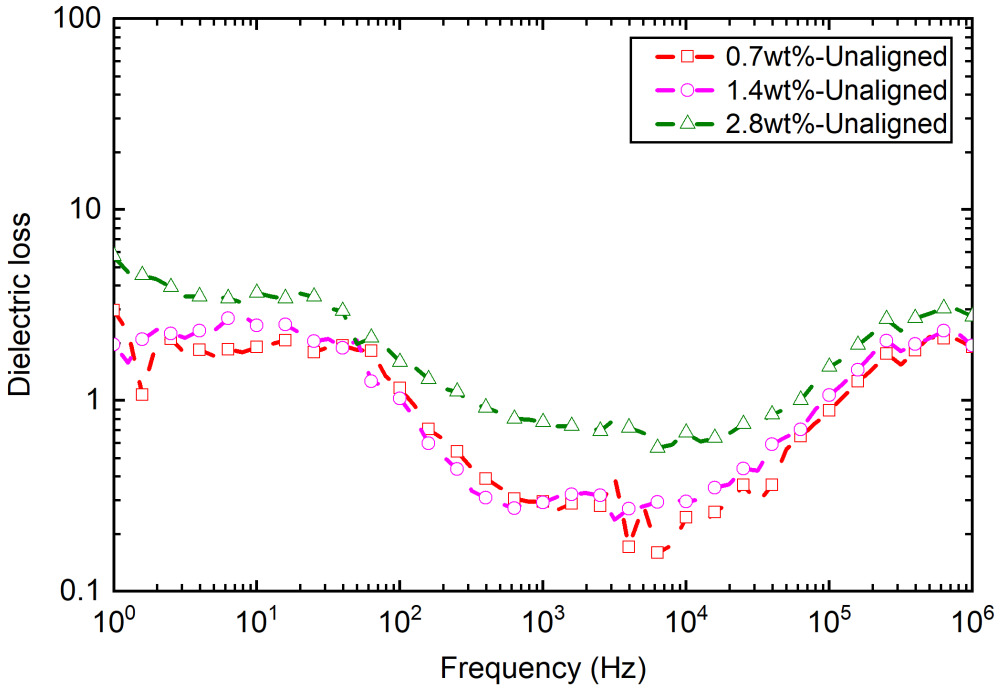

(a)

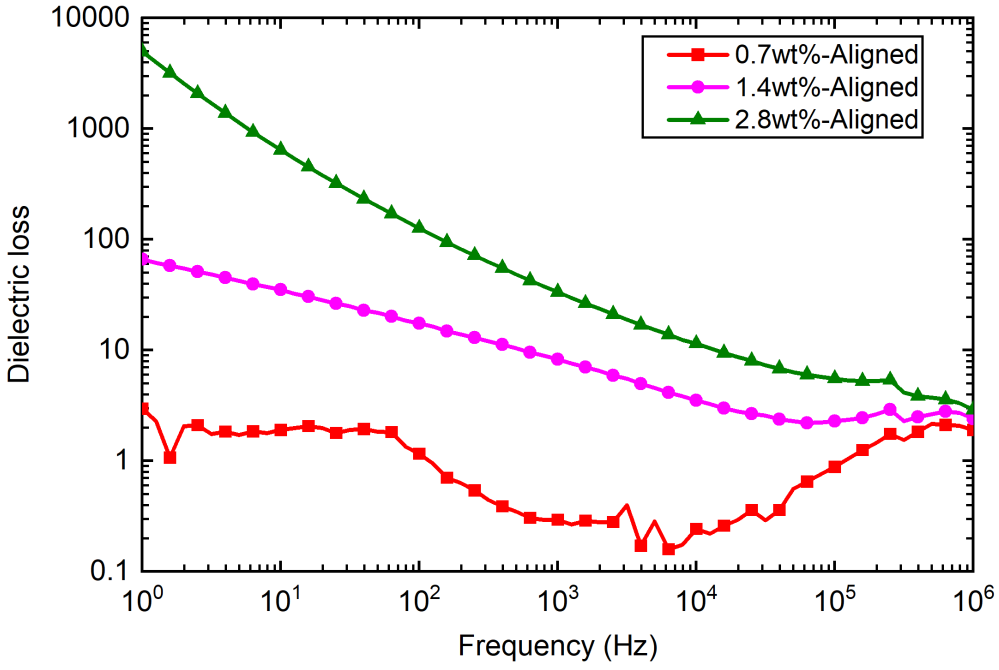

(b)

Figure 25: Dependence of dielectric loss on frequency for a) unaligned and b) aligned GNPs of concentrations 0.7, 1.4 and 2.8 wt% in epoxy. Here, the magnitude of electric field is 35 V/mm at 10 kHz.

percolative behavior. Dielectric constant decreases as frequency increases due to increased non-ohmic conduction which facilitates barrier-tunneling (electron hoping) between GNPs separated by epoxy layer [91]. The increase in dielectric constant can be attributed to the chain formation which results in a highly percolated system which makes the system highly conductive. In addition to this, the orientation of these particles towards the electric field and close proximity of the particles result in high interfacial surface area and polarization density leading to enhanced MWS effects. This can be substantiated with dielectric loss variations shown in Fig. 25b. Alignment and chain formation of GNPs will increase the dielectric loss by several orders of magnitude due to conductive nature of the sample resulting in high leakage current [143]. This can be witnessed in 1.4 wt% and 2.8 wt% aligned samples whose dielectric losses are 80 and 5000 respectively. These increments in dielectric constant can be correlated to the AC conductivity measurements obtained during alignment as seen in Fig. 22. Higher GNP content and alignment will result in increased AC conductivity, which signifies higher dielectric constant due to percolation. We do not see similar behavior for 0.7 wt% aligned sample which implies it was below percolation threshold and its dielectric loss variation with frequency is identical to unaligned samples as shown in Fig. 25a.

The corresponding AC conductivity curves for 0.7, 1.4 and 2.8 %wt aligned and unaligned samples for a frequency range of 1 Hz to 1 MHz are shown in Fig. 26. In both aligned and unaligned cases the AC conductivity increases with frequency due to the propensity of electrons to jump across interfaces (epoxy) due to frequency derived electron hopping. At high frequencies such as 1 MHz, the AC conductivity is dominant which results in negligible difference in AC conductivity for all weight fractions. It should be noted that for lower concentrations of GNPs (below percolation threshold) the distance between GNPs is high and their conductivity is frequency dependant for the entire range from 1 Hz to 1 MHz. This behavior is expected for insulating materials [66]. In Fig. 26b we notice an onset of percolative behavior for 1.4 wt% concentration. As the sample becomes more conductive due to percolated networks the AC conductivity will become frequency independent as depicted

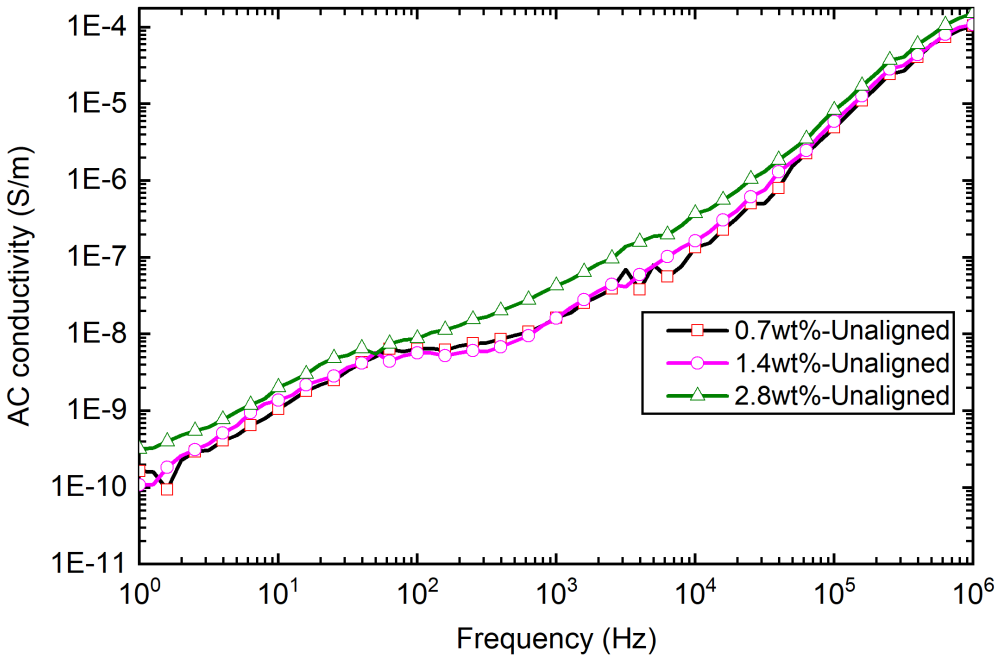

(a)

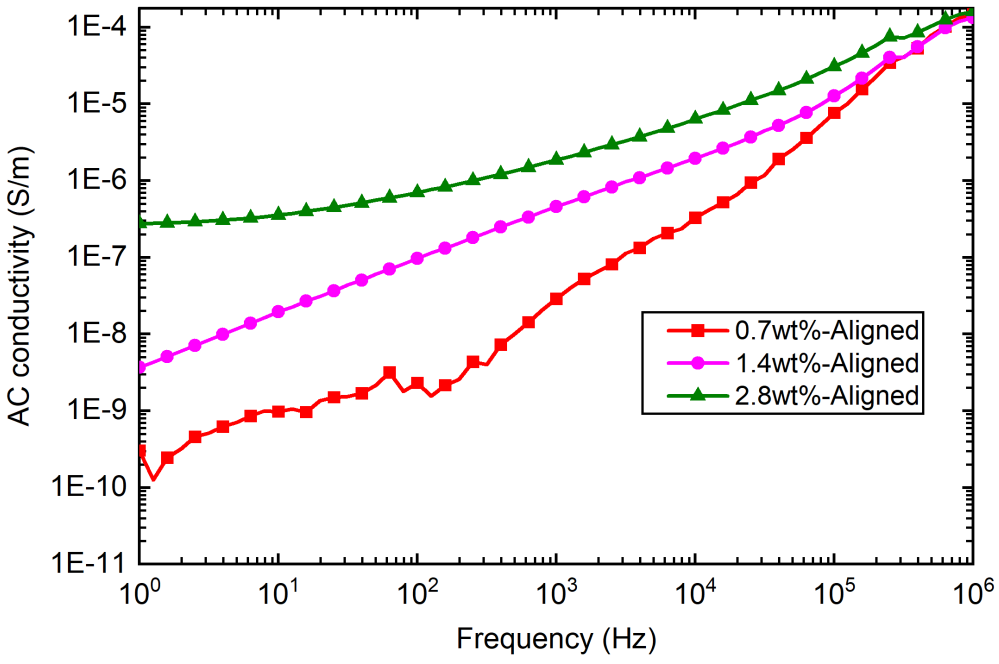

(b)

Figure 26: Dependence of AC conductivity on frequency for a) unaligned and b) aligned GNPs of concentrations 0.7, 1.4 and 2.8 wt% in epoxy. Here, the magnitude of electric field is 35 V/mm at 10 kHz.

in Fig. 26b for 2.8 wt% between 1 Hz and 100 Hz. This happens because of DC conductivity being the major influence during these frequencies. However, after 100 Hz, it becomes a

function of AC frequency due to high frequency phenomena which causes the generated dipoles to have less time to orient towards the external electric field [91]. Based on this, all unaligned and 0.7 wt% aligned samples are below percolation threshold. Table 9 shows the increment of Young's modulus for various concentrations of GNPs compared to unaligned samples. As particles tend to orient and result in chain formation we expect to see an increase in strength since in-plane modulus is significantly higher than through-thickness modulus for a GNP. We observed a (7–15%) increase along the aligned direction for different concentrations tested.

The dielectric constant and dielectric loss variations with frequency for 1.4 wt% GNPs in epoxy exposed to different intensities of electric fields are shown in Fig. 27. Here, we see an increase in dielectric constant and dielectric loss as the applied external electric field during alignment is increased. These increments suggests that the quality of alignment is improved which is not predicted by Wu's study [53]. The dielectric constant increases with increase in electric field strength due to the formation of higher number of efficient chains. The relatively lower dielectric constant and dielectric loss for the sample exposed to 25 V/mm suggests that lesser number of conducting chains have formed. This might be due to increased rotation time caused by GNP agglomeration. These results are in synchronous with the AC conductivity data obtained during the alignment for different electric fields from Fig. 23. However, we notice a steep increment in dielectric constant for 35 V/mm as compared to 25 V/mm. This is due to the parabolic decrease of rotational and translation times as predicted from equations (3.2.1) and (3.2.3). This reflects on the quality of alignment for a specific concentration of GNPs, which implies the chain formation was not as effective as higher electric fields. The increment in dielectric constant at 1 Hz reduces beyond 35 V/mm signifying that the higher amount of electric fields beyond 55 V/mm will lead to saturation point of obtained dielectric constant.

The dielectric loss of sample exposed to 25 V/mm electric field intensity was 10 compared to

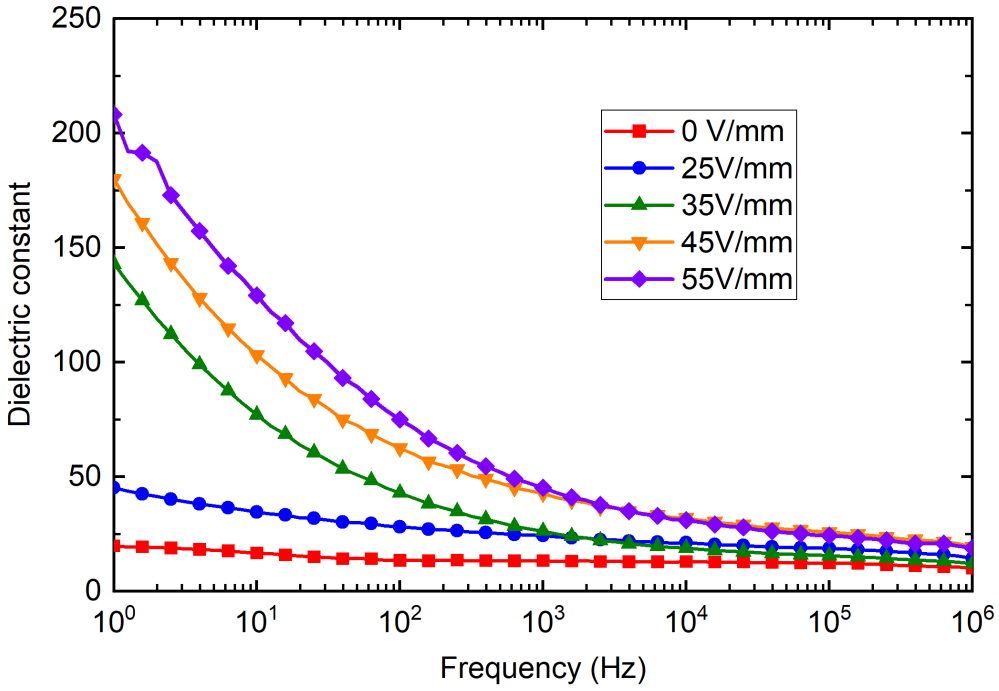

(a)

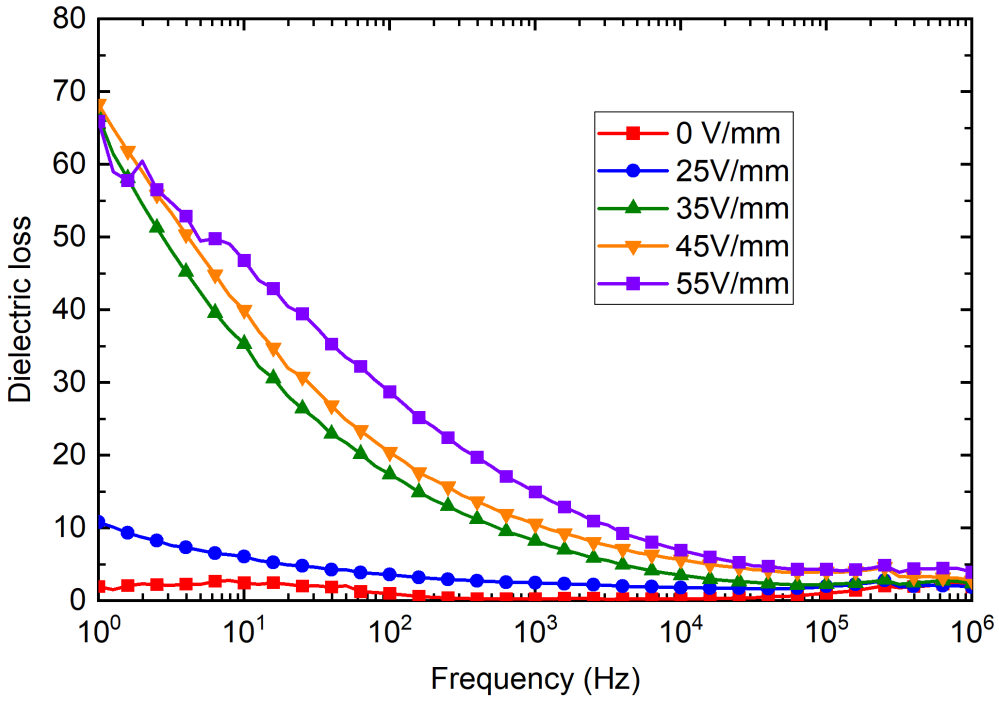

(b)

Figure 27: a) Dielectric constant and b) dielectric loss variation for 1.4 wt% GNPs in epoxy exposed to different intensities of electric fields (Unaligned, 25, 35, 45, 55 V/mm). Here, the external electric field was applied for 60 minutes and samples were left to cure.

Table 9: Increment of Young's modulus in the aligned direction for various weight fractions exposed to 35 V/mm intensity and 1.4 wt% concentration exposed to various electric field intensities.

GNPs (wt%)	Young's modulus Increment (%)	Electric field intensity (V/mm)	Young's modulus for 1.4 wt% GNPs Increment (%)
0.7	7	25	3
1.4	9	35	9
2.8	15	45	11
-	-	55	13

65–68 for higher electric field intensities. There is no difference in dielectric loss for (35–55 V/mm) implying the saturation and also the formation of effective chains which tend to have lesser agglomerations. Table 9 also shows the increment of Young's modulus along the aligned direction for 1.4 wt% GNP samples exposed to different electric field intensities. A similar trend as dielectric properties was observed for Young's modulus in the through-thickness direction of the aligned samples as compared to unaligned samples, the increment is 3% for 25 V/mm and for 35 V/mm the increment is 9% and thereafter the percent change is restricted to 2%. This signifies a saturation point for mechanical strength as well. Comparison of dielectric properties and Young's modulus with in situ AC conductivity curves for various weight fractions and electric field intensities show that this method is a reasonable qualitative technique to monitor the alignment process for GNPs. In the next section the effect of brownian motion is studied using AC conductivity measurements.

3.2.4 Brownian motion of GNPs in epoxy

GNPs suspended in epoxy will not be stationary and these particles are subjected to constant random motion due to collisions from other particles. This phenomenon is known as brownian motion. To study this effect on alignment and chain formation of the GNPs, an experiment was designed to study the variation of AC conductivity for 5 minute electric field on/off cycles. The normalized AC conductivity variation for 1.4 wt% GNPs in epoxy subjected to 35 V/mm electric field intensity is shown in Fig. 28. Here, the electric field was turned on for every 5 minutes until 65 minutes. The AC conductivity was zero when no external field

was applied. It is evident that the orientation/chain formation phenomenon was affected due to brownian motion of GNPs. At time t=0 we see a rise in conductivity for 5 min and the electric field was switched off and when the electric field was applied again at t=10 min we noticed a discontinuity of AC conductivity and this reduction amounts to 22%. At the 60 minute cycle the reduction in AC conductivity decreases to 10%. The effect of brownian motion tends to decrease steadily which could imply that chain formation may lead to stable connections due to static forces, while the free particles are still prone to brownian motion.

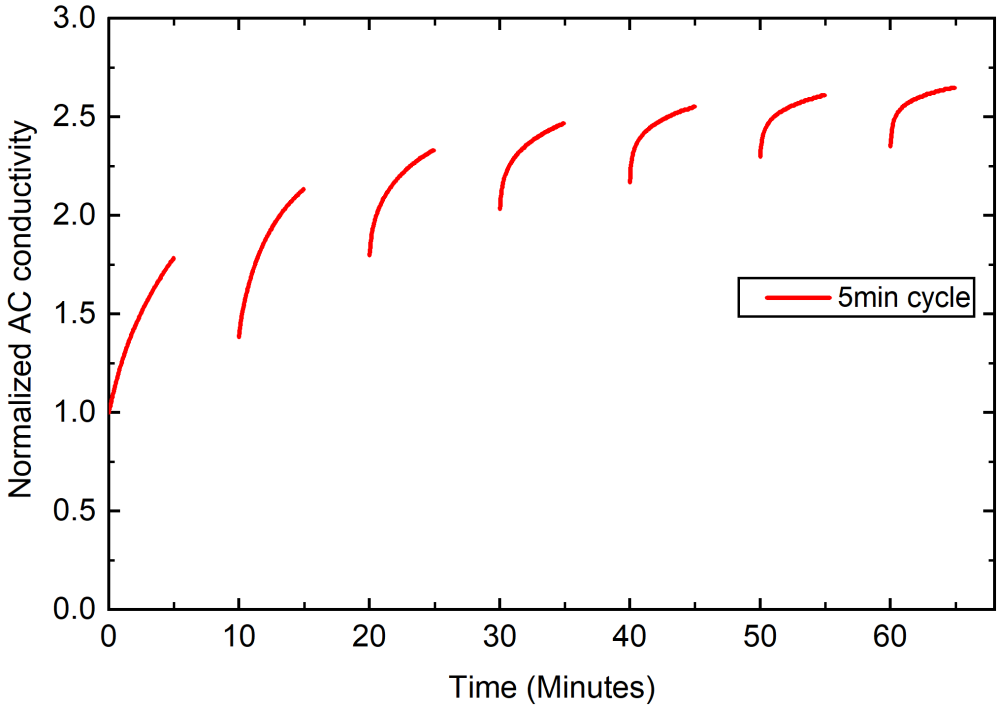

Figure 28: Normalized AC conductivity variation for 1.4 wt% GNPs in epoxy at 35 V/mm. Here, the external electric field is applied every 5 minutes to study the brownian movement.

To further understand the effect of brownian motion on alignment of GNPs, alignment was performed for 1.4 wt% concentration of GNPs in epoxy at 35 V/mm for a limited time between 5-70 minutes and the samples were left to cure at room temperature. The variation of dielectric constant and dielectric loss for these samples are shown in Fig. 29a. The growth of dielectric constant and dielectric loss were synchronous and remain steady until 30 minutes. After that they rapidly increase and stabilize after 60 minutes. The effect of brownian motion is enhanced in the samples that were aligned for less than 30 minutes.

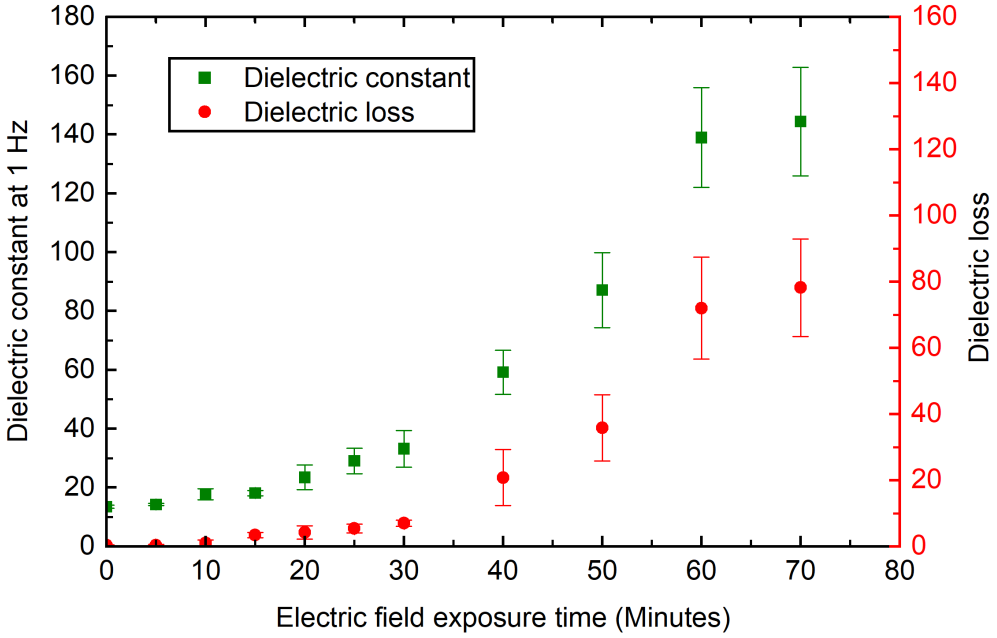

(a)

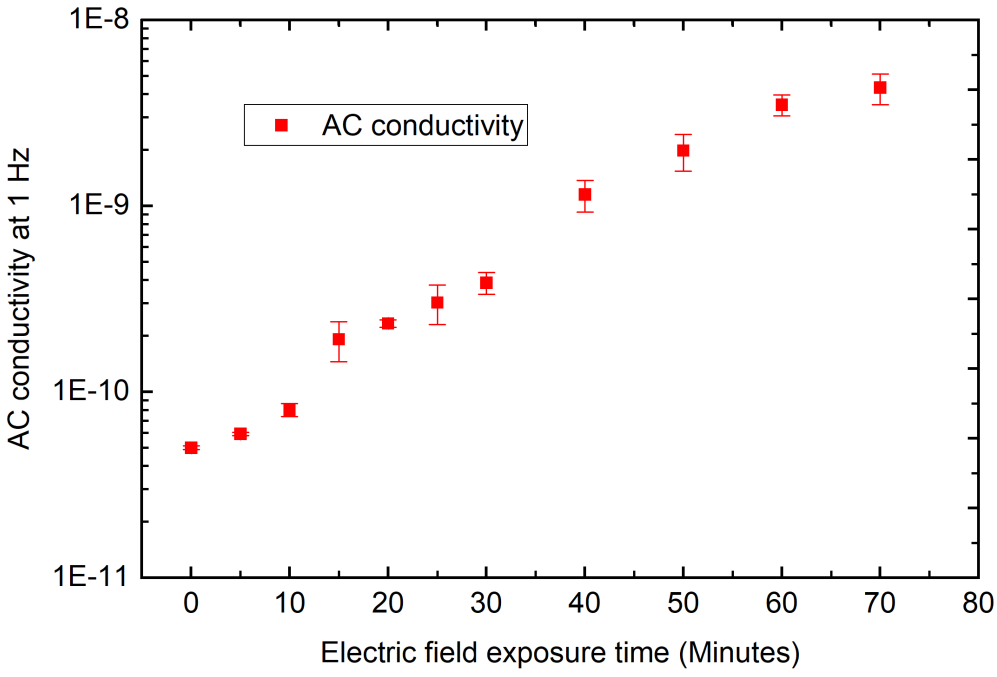

(b)

Figure 29: a) Dielectric constant, dielectric loss and b) AC conductivity variation at 1 Hz for 1.4 wt% GNPs in epoxy at 35 V/mm. Here, the external electric field was applied for a limited amount of time and samples were left to cure.

Although we notice that the AC conductivity during alignment for 1.4 wt% at 30 minute mark in Fig. 21 almost reaches a saturation point, the dielectric constant of the sample

remained low. This can imply that the chain formation was subjected to severe brownian motion that resulted in disruption of these chains and randomizing the orientation of GNPs. The samples that were cured for more than 30 minutes had a significant increase in dielectric constant and dielectric loss. This can be explained by the fact that the effect of brownian motion continues to decrease steadily as seen in Fig. 28. The growth of AC conductivity at 1 Hz for these samples is also shown in Fig. 29b. We see a 2 order magnitude increase in AC conductivity and the rate of increase seems to be steady and tending to saturate after 60 minutes. In Fig. 29a the standard deviations of dielectric constant and dielectric loss are negligible up to 30 minute mark and increases significantly thereafter. We believe that the AC current is dominated by displacement current in the beginning stages of alignment assuming that the system is below percolation threshold and later resistive current takes over due to formation of conductive chains. The formation of these conductive chains will allow the flow of direct current rendering the electric field ineffective in the surrounding regions. Furthermore, the chain formation of GNPs deprives the surrounding regions of GNPs due to continuous attraction of particles, leading to a more concentrated area of percolated chains. Taking these factors into account, the bulk composite becomes in-homogeneous after the application of electric field. Kou *et al.* also observed the localized effects of electric field on GNPs [144]. They performed a statistical analysis on the GNP orientations affected by a strong electric field (400 V_{rms}) and found that the agglomerates were not affected by the electric field and they also observed that the effect of electric field was limited to certain regions in the composite.

3.3 Conclusion

In this study, the alignment of GNPs were successfully characterized using continuous in situ AC conductivity measurements for higher concentrations of GNPs (0.7, 1.4 and 2.8 wt%). AC conductivity observations showed that the time required for alignment has a strong dependence on concentration of GNPs, viscosity of the epoxy/GNP blend and electric field

intensity. Contemporary analytical models fail to address the effects of these parameters for alignment. The quality of alignment predicted by AC conductivity measurements taken during the process of alignment were substantiated by dielectric properties such as dielectric constant, dielectric loss, and AC conductivity, and Young's modulus values obtained from cured samples. It was found that the alignment time increases with concentration due to additional viscous forces created by agglomerations. The AC conductivity measurements of 1.4 wt% GNPs exposed to different electric field intensities showed that the quality of alignment can be improved by using higher electric fields. Higher electric fields will have faster rotation and translation times which reduces the possibility of deleterious agglomerate formations. We noticed a 9–15% increase in Young's modulus compared to unaligned samples for various concentrations and 3–13% increase for various electric field intensities for 1.4 wt% of GNPs. We also noticed a 61-2115% increase in dielectric constant at a frequency of 1 Hz in the aligned direction for 0.7–2.8 wt% concentrations of GNPs. The effect of browninan motion was also studied using AC conductivity measurements and it was found that the brownian motion was prevalent in the early stages and gradually reduces with time as particles were held together as chain formation commenced. The growth of dielectric constant, dielectric loss and AC conductivity with electric exposure time for 1.4 wt% GNPs at 35 V/mm was also studied to further understand the effects of brownian motion. We noticed a negligible growth of dielectric constant and dielectric loss until 30 minutes due to brownian motion and followed by a rapid increase until 60 minutes until they stabilized. Besides this, we also found that the application of alignment results in a heterogeneous composite due to localized effects of electric field, non responsive regions of agglomerations and stacked up percolated chains.

CHAPTER IV

PLANAR ALIGNMENT OF GRAPHENE NANOPLATELETS (GNPs) IN EPOXY

In this study, we align various concentrations (0.175-1.4 wt%) of GNPs of two sizes (M-5 and M-25) along the in-plane directions (x and y) using a rotating electric field in a thermosetting epoxy. In-situ AC conductivity measurements were used to characterize the alignment process. Dielectric constants of the resultant composite was calculated in in-plane and through-thickness directions to substantiate the planar alignment.

4.1 Materials and Methods

4.1.1 Experimental setup

Here, we present an experimental setup to understand the unidirectional alignment process which will be extended to planar alignment of GNPs. For unidirectional alignment, we used a setup that is made of two conductive aluminum plates of size 200 $\times$ 200 mm which are seperated by polymer spacers to prevent shorting. These plates are connected in series to a wideband amplifier (7602M, Krohnite, Brockton, Massachusetts) which is connected to an AC signal generator (3312A, HP, Alto California) and closing the loop in series with a precision multimeter (5491B, BK Precision, Yorba Linda, California). LabVIEW software was connected to the multimeter to track the minuscule changes in AC current. The schematic is represented in Figure 31a. The AC conductivity was measured at 10 kHz considering the AC

current, electric field intensity and dimensions of the sample. AC electric field was applied for 70 minutes depending on the weight fraction of GNP in epoxy and left to cure at room temperature for 24 hours.

For planar alignment we faced three challenges to acquire repeatable results. Firstly, the electrode manufacturing was done by using an aluminum pipe of diameter 9 mm and length 150 mm, which was filled with molding wax. Four horizontal and equally spaced groves were cut in 90 degrees along the length of the pipe using a milling machine. Around 25mm of pipe is left unmachined on each side to provide structural support which was sawed off later. Smaller grove width and accurately spaced groves should be ensured for uniform alignment. The grove width was around 1.5mm. Then fast casting epoxy (JB clear weld epoxy) was applied between the groves to provide structural support by adhering the electrode sections and to insulate the adjacent aluminum sections. After curing for 24 hours at room temperature, the setup was placed in an oven at 60°C to melt the molding wax and subsequently the unmachined part of aluminum pipe was sawed off manually. The result is a composite pipe consisting of equally spaced conductive aluminum sections separated by 1.5mm insulating epoxy sections. The bottom part of the composite pipe electrode was filled with silicone mold-making epoxy to prevent leakage of epoxy/GNP mixture during the process of alignment.

Second challenge was to provide a continuous rotating electric field to the epoxy through the conducting aluminum sections. An electrode holding setup was 3D printed using PLA which can hold the electrode and simultaneously rotate using a stepper motor controlled by Arduino software. The composite pipe can be mounted on the electrode holder. Two spring loaded electrodes were employed to ensure good connection to the aluminum electrodes while rotating and to create an electric field between the parallel composite pipe aluminum sections. The stepper motor rotates the composite pipe so that the two parallel sections will create an electric field alternatively.

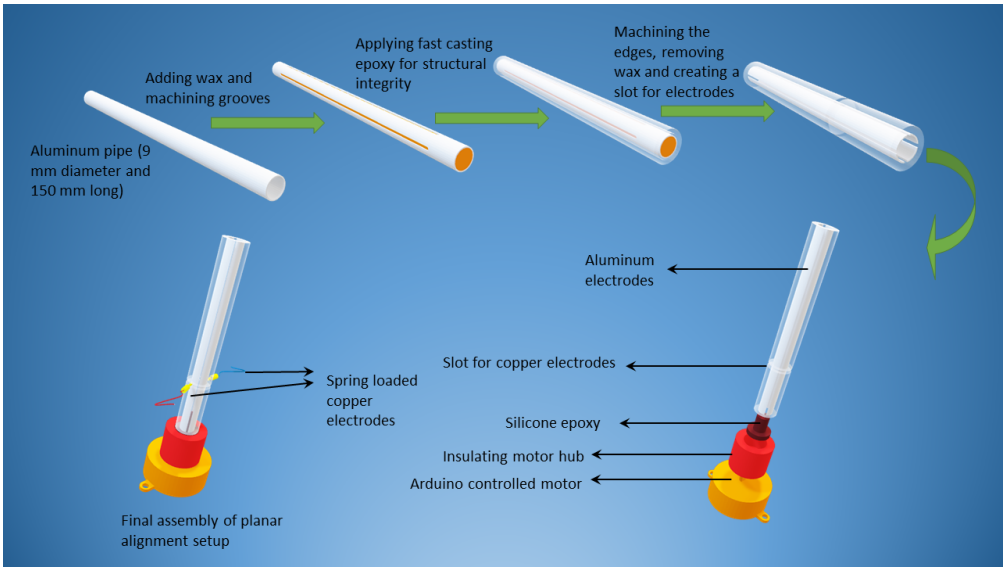

Figure 30: The composite electrode fabrication process for planar alignment

Third challenge was to observe and quantify the alignment process using AC current. This was accomplished using a multi-meter connected in series with the wide-band amplifier (7602 M. Krohn-Hite Corporation, Brockton, Massachusetts), which is connected in series with the spring-loaded electrodes and the composite pipe. The data acquisition of AC current variations was made in LABVIEW to observe the real time alignment process.

4.1.2 Materials and preparation

The GNPs (M5 and M25, XG Sciences, Lansing, Michigan) have an average thickness of 6-8 nm with a surface area of 120-150 m^2/g and an average particle diameter of 5 and 25 µm respectively. Epoxy resin (EPON 862, Hexion, Columbus, Ohio) and hardener (EPIKURE Curing agent 3274, Hexion, Columbus, Ohio) were used for dispersing the GNPs. EPON 862 is low viscosity blend of diglycidyl ether of bisphenol F. The liquid hardener is a moderately reactive low viscosity aliphatic amine.

GNPs in powder form were added to epoxy resin and stirred on a magnetic stirrer for an hour to dissolve and break the larger agglomerates. Then the mixture was passed through a three-roll mill (T65, Torrey Hills Technologies, San Diego, California) for 15 times at 100 rpm with

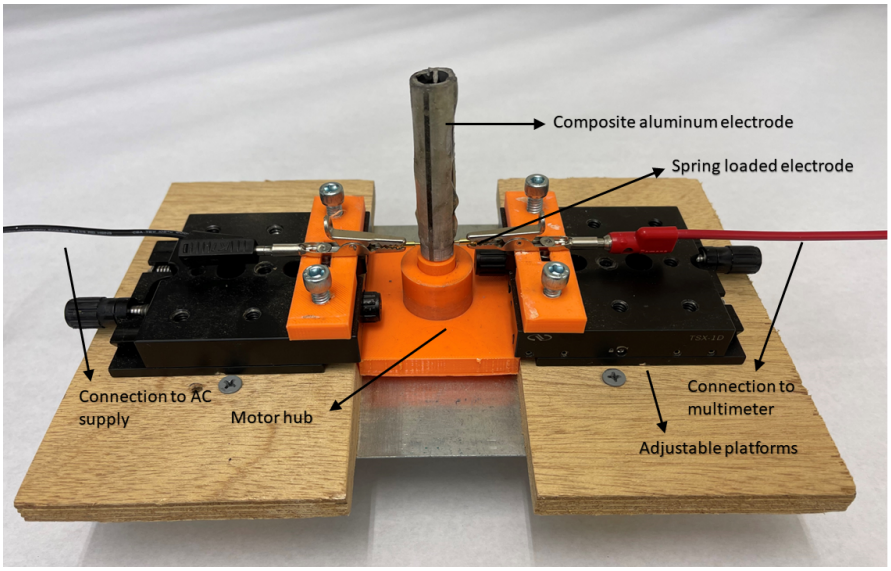

(a)

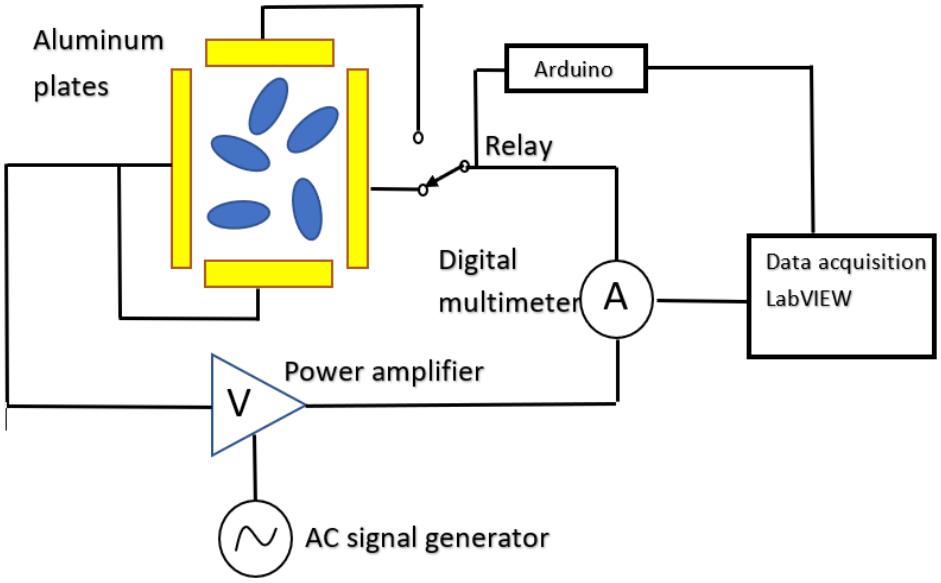

(b)

Figure 31: a) Real experimental setup and b) schematic of planar alignment setup.

a roller-gap distance of 25 µm to exfoliate and obtain uniform dispersion of GNPs in epoxy. After the dispersion process, stoichiometric ratio of hardener (100:40) was added to the mixture and degassed in a vacuum oven for 30 min to remove the trapped air bubbles. The mixture was then poured into a mold made of aluminum plates for unidirectional alignment and aluminum composite pipe electrode for planar alignment. The samples were cured at

room temperature for 24 hours prior to electrical testing.

4.1.3 Alignment of GNPs

Nanocomposites of different weight fractions (0.175, 0.35, 0.7 and 1.4 wt%) of size M5 and weight fractions (0.175, 0.35, 0.7 wt%) of size M25 were unidirectionally aligned at 35 V/mm and 10 kHz, to study the effect of concentration on AC conductivity and to compare with planar aligned samples. The same weight fractions were used for planar alignment. These samples were aligned at 25 V/mm and 10 KHz. Electric field magnitude was reduced to accomodate the larger thickness of the planar electrodes.

4.1.4 Material analysis and characterization

The dynamic viscosity of the GNP and epoxy mixture was measured prior to alignment process using a viscometer (LVDVE, Brookfield, Middleboro, Massachusetts) according to ASTM-D2196. Post alignment and curing, 5 samples of size 10 x 10 x 3 mm for unidirectionally aligned nanocomposite were cut for each weight fraction using a precision saw and were lightly sanded on top and bottom surfaces using 800 grit paper. Where as for planar aligned cylindrical sample, rectangular specimens of size $5 \times 5 \times 2$ mm were cut from 90 degree orientations which resemble 1 and 2 directions and specimens of size $5 \times 5 \times 2$ mm were cut cross sectionally along the z axis which resemble direction 3. The specimens obtained from the cylindrical sample is depicted in figure. Due to the presence of insulating epoxy, the top and bottom surfaces were coated with an electrically conductive epoxy (Duralco 120, Cotronics, Brooklyn, New York) to provide uniform electrical contact.

XRD was performed for each weight concentration of both M5 and M25 planar aligned GNPs in three directions (x,y,z). XRD analysis was done using AXS D8 Discover diffractometer (Bruker, Madison, Wisconsin) with a Cu-$\kappa\alpha$ (40 kV, 40 mA) X-ray source. The XRD data was collected over a 2 θ range of 10 to 50 degrees using refractive mode 2-D detector. The pixel overlap was 30% and each frame was exposed to 30 seconds.

The cylindrical samples were fractured using liquid nitrogen to visually observe the planar aligned GNPs. The surfaces were fractured in two orthogonal directions and the in-plane and out of plane surfaces were viewed under a field emission scanning electron microscope (S-4800 FESEM, Chiyoda city, Tokyo). The surfaces were coated with irridium han using a sputter coater (EM ACE600, Leica Microsystems Inc., Deerfield, Illinois).

The dielectric spectroscopy was performed to obtain dielectric constant and dielectric loss along the aligned direction using a potentiostat (VersaSTAT 3F, Ametek, Berwyn, Pennsylvania). For these properties, the frequency was ranged from 1 Hz to 1 MHz. In all characterization tests, randomly oriented samples were compared to aligned samples. Dielectric constant, dielectric loss and AC conductivity were calculated using standard formulations as follows [140].

$$\varepsilon_r^{'} = \frac{-Z''}{2\pi f \varepsilon_o ((Z')^2 + (Z'')^2)} \frac{l}{A} \tag{4.1.1}$$

$$\varepsilon_r^{''} = \frac{Z'}{2\pi f \varepsilon_o ((Z')^2 + (Z'')^2)} \frac{l}{A} \tag{4.1.2}$$

$$\sigma_{AC} = 2\pi f \varepsilon_o \varepsilon_r^{''} \tag{4.1.3}$$

Here, f is the AC frequency, ε_o is the permittivity of free space, l and A are sample thickness and surface area respectively and Z' and Z'' are the real and imaginary parts of impedance respectively.

4.2 Results and Discussion

4.2.1 Mechanics of planar GNP alignment

A single GNP surrounded by a dielectric fluid will undergo electronic polarization in the presence of an external electric field. The polarization is higher in the in-plane direction compared to the through thickness direction causing a dipole effect. This dipole is typically unaligned in the electric field and it produces a dipole moment at the center of the platelet which causes it to rotate towards the electric field while opposing the rotational viscous force generated by the epoxy. After they are aligned in the fluid, the presence of attraction forces from nearby particles causes a translation motion that results in long chains of particles. This translation force is opposed by the translational viscous force. Depending on the electric field strength, particle size, viscosity of the fluid rotation and translation times vary. Wu *et al.* formulated the rotation time of a GNP experiencing an external electric field (E_o) from an initial angle θ_o to a final angle $\theta_{'}$. This is given by the following equation [53].

$$t_r = \frac{1}{A} ln \frac{\tan \theta_o}{\tan \theta'} \tag{4.2.1}$$

Here,

$$A = \frac{\pi}{8\eta} \frac{\varepsilon_m}{\left(\frac{\pi}{2} - \frac{b}{a}\right)} E_o^2 \tag{4.2.2}$$

Here, A is a function of the viscosity of the epoxy (η), dielectric constant of the epoxy (ε_m), electric field strength (E_o), half thickness of GNP (b) and radius (a).

Subsequently, the particles tend to translate after they are aligned towards the electric field. The translation time was also calculated by Wu *et al.* and it is given by the following equation [53].

$$t_c = \frac{2x_o^3}{3B} \tag{4.2.3}$$

Here,

$$B = \frac{4\pi a^4}{9\eta k_t \varepsilon_o} \frac{E_o^2 \varepsilon_m^2}{\left(\frac{\pi}{2} - \frac{b}{a}\right)^2} \tag{4.2.4}$$

and,

$$x_o = \frac{1}{\rho} \frac{m_G}{W_G} \frac{1}{4a^2} \tag{4.2.5}$$

Here, t_c is the translation time of the particles, k_t is the translational friction coefficient that depends on the surface area of GNP and x_o is the initial perpendicular distance between two adjacent particles which depends on the density of the epoxy (ρ), weight fraction of GNP (W_G), mass of GNP (m_G) and radius of GNP (a). The mass of GNP (m_G) which is calculated to be around 2.65 $\times 10^{-14}$ kg for a M25 GNP particle. The radius of the platelet is 12.5 μm. The density of the epoxy system (1.1 g/cm^3) was calculated from the densities of the epoxy and hardener. Also, B is a constant depending on the viscosity, dimensions of the platelet, dielectric constant of the epoxy and the intensity of electric field.

The above mentioned equations will give an approximate time for alignment, taking into account that the viscosity would remain low for addition of lower weight fractions. Higher weight fractions of GNPs, will lead to drastic increase of viscosity subsequently increasing the particle to particle interactions. A study on polarization forces and conductivity effects in electrorheological fluids showed that multiple particle interactions should be considered if the distance between particles is less than the particle diameter [141]. Based on the above speculation, we do not consider any added viscosity effects for samples whose interparticle

distance is more than the diameter. In other cases we consider the viscosity to be an additional factor in deciding the translational time and rotational time. Table. shows the variation of rotation and translation times of different GNPs size and their concentrations. If the viscosity is assumed to be the same, the particle rotation time does not change, which is true for M5 (0.175, 0.35 and 0.7 wt%) and M25 (0.175 wt%). Where as in other cases, the particle distance is less than the particle diameter, hence there is a slight increase in rotation time. Although the increase seems insignificant, as the weight fraction of GNP increases we see noticeable changes in rotation and translation times that should be accounted for planar alignment. It is assumed that translation of particles takes place after rotation and dispersion is uniform throughout. However, if the particles are close to each other, translation can take place irrespective of its orientation. This is an important consideration for planar alignment, where we define switching time. Translation takes place due to opposite charges present on the nearby particles, and when the electric field rotates 90, the charges on the transversely isotropic platelets switch accordingly as shown in figure. This causes repulsion of the nearby particles and may disorient the particle. Hence, to avoid chain formation we need to rotate the electric field before complete translation of the particles take place. Hence, we consider the switching time to be around 0.5 times translation time. This ensures that the particles rotate uniformly in both x and y directions. However, for lower weight fractions in the case of M5 (0.175 wt%), the switching time is very high compared to rotation time. Here, any arbitrary switching time can be considered provided it is equally distributed between x and y directions. The change in orientation of the GNP and chain formation can be monitored by AC current flowing through the system. The next section explains the AC conductivity behavior for one direction alignment and that will be extended to planar alignment.

Rotation time, translation time and spacing between the GNPs predicted using the model proposed by Wu *et al.*.The inputs into the model are GNP wt% and experimentally determined viscosity (mPas).

Table 10: Rotation time, translation time and spacing between the M5 GNPs predicted using the model proposed by Wu *et al.*.The inputs into the model are GNP wt% and experimentally determined viscosity (mPas). [53]

GNP wt%	x_o (μm)	Rotation time (min)	Translation time (sec)
0.175	22	20	7273
0.35	11	20	910
0.7	5.5	20	114
1.4	2.8	22	16

Table 11: Rotation time, translation time and spacing between the M25 GNPs predicted using the model proposed by Wu *et al.*.The inputs into the model are GNP wt% and experimentally determined viscosity (mPas). [53]

GNP wt%	x_o (μm)	Rotation time (min)	Translation time (sec)
0.175	21	20	34
0.35	11	22	4.7
0.7	5.5	24	0.8

Table 12: GNP wt%, rotation time and switching time variation for different exposures calculated using the analytical model proposed by Wu *et al.* for M5 and M25 GNPs exposed to 25 V/mm 10 kHz electric field [53]. Here, switching time is defined as the time after which the electric field is rotated 90° about z-axis.

	M5		M25	
GNP wt%	Rotation time (min)	Switching time (sec)	Rotation time (min)	Switching time (sec)
0.175	50	6747	50	43
0.35	50	843	52	10
0.7	50	105	56	1
1.4	54	14	-	-

4.2.2 AC conductivity results

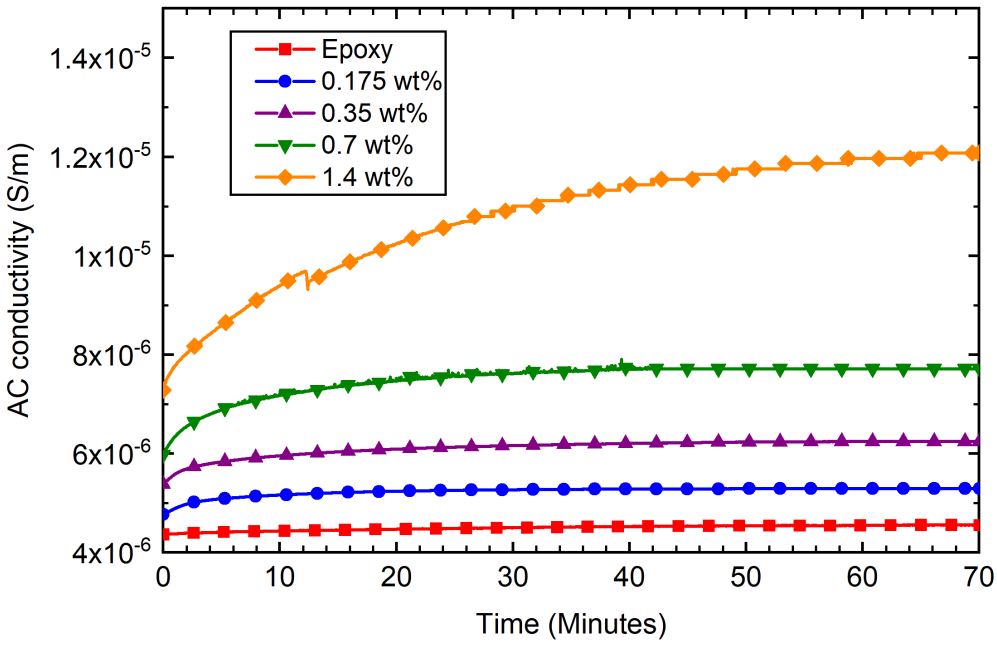

Figure 32: Variation of AC conductivity captured during unidirectional alignment process for M5-(0.135–1.4 wt%) GNP and epoxy at 50 V/mm with time. The sampling rate was 40 samples/second, here every 2000^{th} data point is represented.

The AC conductivity variation for M5- GNP for various concentrations (0.135–1.4 wt%) captured during unidirectional alignment process for 70 minutes is depicted in Fig. 32. For a specific concentration the AC current of the system increases during alignment due to changing orientation of the GNPs and subsequent chain formation leading to percolated chains. The primary mechanisms involved in changing AC current from changing orientation of GNP are interlayer conductance and in-plane conductance of GNP. Whereas chain formation is predominately contact conductance and electron hopping between GNPs [142]. As GNPs orient themselves along the electric field direction, they lead to microstructural changes in resistance that reflects in the overall conductivity of the sample. The AC current is also a function of the concentration of GNPs. More GNPs, will result in increase of AC conductivity as seen in Fig. 32. Also, it is interesting to note that each concentration will have a distinct curve resulting from quantity of percolated chains. Higher concentrations will have the capacity to form chains earlier and will result in a steeper curve. However, all the

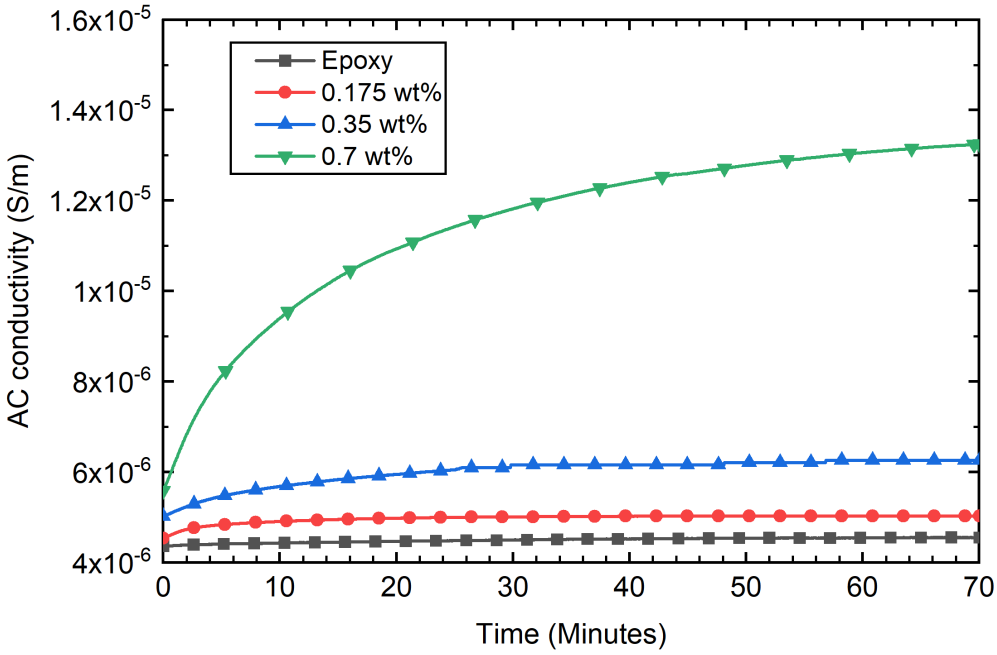

Figure 33: Variation of AC conductivity captured during unidirectional alignment process for M25-(0.135–0.7 wt%) GNP and epoxy at 50 V/mm with time. The sampling rate was 40 samples/second, here every 2000^{th} data point is represented.

AC conductivity curves tend to flatten after a certain time. This signifies the maximum AC conductivity achieved for a specific concentration. Similar behavior can be seen in Fig. 33 for M25-GNPs as well. As concentration increases, the viscosity increases which makes the behavior more complex and will lead to higher saturation times compared to lower weight fractions such as 0.175 and 0.35 wt%. Figure. 21 also shows the AC conductivity variation for epoxy sample which does not contain any GNPs. As expected we do not see any variation in AC current due to lack of conducting particles and microstructural resistance changes. Also, Tables 10 and 12 shows the variation of translation times with concentration for both M5 and M25 GNPs. The translation time for M25 -0.7wt% is 0.8, hence we see a steeper curve compared to M5-0.7wt% . It should also be noted that the diameter of M5 is five times less than M25 and it requires five times more number of particles for a percolated chain. For M5- 0.175 wt%, the translation time is around 100 minutes which is greater than its rotation time and the total alignment time of 70 minutes. This shows that the percolated channels are not possible in the system. However, we see a noticeable increase in AC conductivity

in the early stages. This shows that orientation of these GNPs are primary cause of the increment and it can be captured for the bulk system.

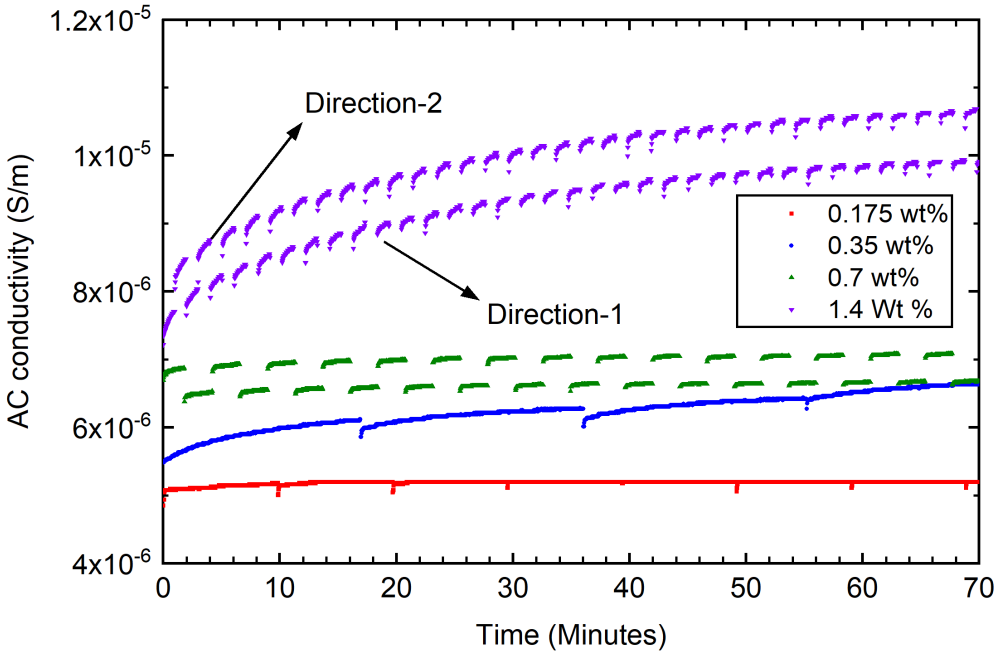

Figure 34: Variation of AC conductivity for M5 planar aligned GNPs. Here, each curve for specific concentration represents AC conductivity in two perpendicular in-plane directions.

The AC conductivity variations for planar alignment for M5 and M25 GNPs are shown in Fig. 34 & Fig. 35 respectively. For each concentration two curves represent the AC conductivity in direction-1 and direction-2. It should be emphasized that the alignment take place in direction-1 has negligible influence on direction-2. This can be substantiated by observing the discontinuities of AC conductivity for M5-15-1.4 wt% in directions 1 or 2. If the alignment in direction-1 is affecting direction-2, we would notice a larger discontinuity between subsequent alignment curves as shown in Fig. 34. For M5-1.4 wt% the switching time is around 60 seconds. The AC conductivity is first measured in direction-1 and after 60 seconds, the electric field is rotated 90° about direction-3 and AC conductivity is measured in direction-2 for 60 seconds. This repeats for 70 minutes. Hence, for this concentration we see 35 smaller curves for each direction which resembles the change in orientation of the GNPs. We also notice a similar increase in conductivity over time which signifies uniform alignment taking place in both directions. It should be noted that the slight difference between the

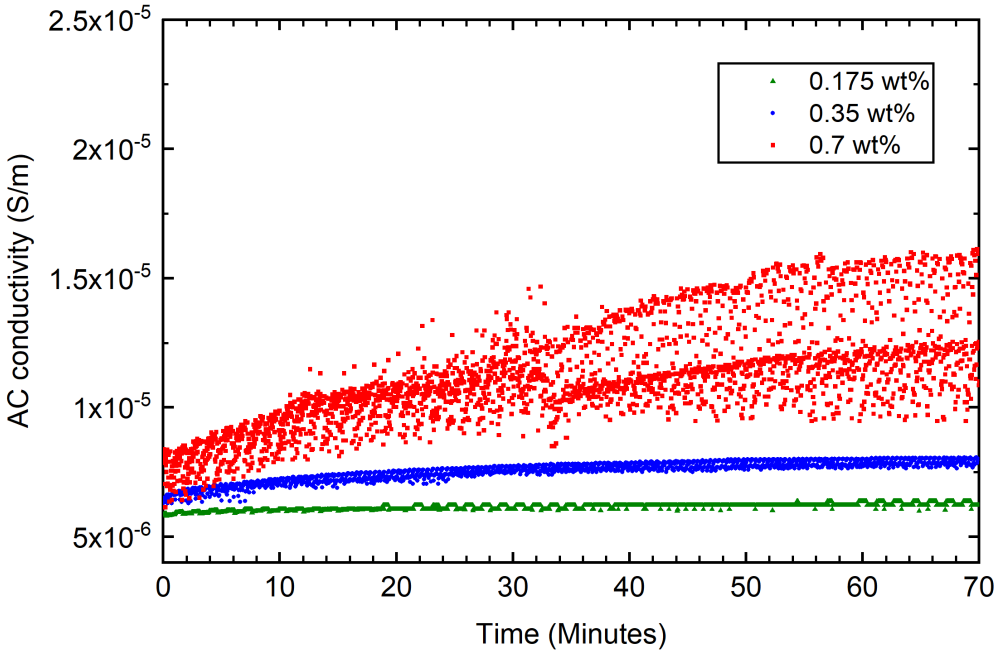

Figure 35: Variation of AC conductivity for M25 planar aligned GNPs. Here, each curve for specific concentration represents AC conductivity in two perpendicular in-plane directions.

direction-1 and direction-2 curves is due to geometric error during the manufacturing of the electrodes. Similar to unidirectional curves as shown in Fig. 32, we see the effect on concentrations on the AC curves obtained. M5-1.4wt% showed the highest increment of conductivity over time, due to close proximity and higher number of particles. It is also interesting to see that the maximum conductivity achieved for planar aligned samples is lower than than unidirectional aligned samples. For the case of unidirectional samples, chain formation takes place which allows uninterrupted direct current to flow through the system. However, the alignment behavior of GNPs in planar alignment are configured to not touch each other, which results restriction of dominating conducting behaviour to in-plane and interlayer conductance. Nevertheless, higher weight fractions such as M5-1.4 wt% has the possibility to exhibit electron tunnelling for particles closer than 1.4 nm. For the case of M5-0.175 wt% the predicted electric field switching time was more than 150 minutes which is greater than rotation time. Hence, an arbitrary switching time of 10 minutes was considered so that alignment in both directions can transpire.

Similar behaviour can be noticed for planar aligned M25 GNP composites as shown in Fig. 35. M25-0.7 wt% experiences a larger increase in conductivity compared to 0.175 and 0.35 wt% due to the possibility of electron hopping apart from other mechanisms of conductance as mentioned in the previous passage. The electric field switching time for M25-0.7 wt% was 1 second and the AC conductivity data of the two directions show a slight deviation which could imply faster rotation of electric fields is necessary. When the switching time is so low, the rotation speed of the motor which ultimately defines the rotation of electric field should be taken into consideration. Apart from this, more detailed study of the transition of dipoles along the surface of the GNP must be done to better understand the behaviour at higher rotation speeds. For concentrations of 0.175 and 0.35 wt% we see a noticeable increase in AC conductivity for the first 5 minutes and 20 minutes respectively, and stabilizes thereafter. However, the increment in AC conductivity was relatively higher for the same concentrations that were aligned unidirectionally as shown in Fig. 33. This due to lack of chain formation which is responsible for the proportional increase of conductivity over time. Nonetheless, the small increments can be associated with orientation changes in GNPs and based on the AC conductivity curves, uniform alignment is taking place. The next section talks about the validation of planar alignment using dielectric spectroscopy.

4.2.3 XRD results

The XRD patterns obtained for planar aligned samples for a 2θ range of 10° to 50° for M5 and M25 GNPs of different concentrations (0.175, 0.35 and 0.7 wt%) are shown in Fig. 36. Here, direction 1 and 2 resemble in-plane directions and direction-3 refers to the through-thickness direction. In all the samples, we see the broad amorphous region exhibited by epoxy. The XRD spectra also shows (002) diffraction peak at 2θ=26.5°, indicating the distance between graphene layers. The application of Bragg's equation gives rise to d-spacing of 3.35 nm, which is the typical distance between graphene layers[]. The (10) diffraction peak indicates a d-spacing of 0.21 nm according to Bragg's equation and this corresponds to the short range

order of stacked graphene sheets [145, 146]. The measured lattice spacing of 0.213 was also observed in HR-TEM imaging of a graphene quantum dot by [147, 148]. In all the XRD spectra, direction-3 does not have the (10) peak and (002) peak is more prominent compared to other directions. However, direction 1 and 2 contains the (10) peak which is only captured when the graphene layers are aligned perpendicular to the incident X-rays. The consistency of this peak in all the samples for in-plane directions provides additional validation of planar alignment transpiring.

4.2.4 Dielectric properties of planar GNP composites

The dielectric constant dependence on frequency for planar aligned, unaligned and unidirectionally aligned M5 and M25 for various concentrations are shown in Fig. 37. Here, for each concentration, directional dielectric constant for three directions is also depicted for planar aligned samples. The presence of GNPs typically increases the dielectric constant of the material due to formation of mini capacitors that utilizes the thin layer of epoxy present between two GNPs as the dielectric material [65]. Unidirectional alignment of GNPs increases the dielectric constant due to orientation of GNPs, chain formation, reduction in proximity of the particles. The later mechanism results in strong interfacial polarization due to the large difference in dielectric constant between epoxy and GNPs, which is widely known as Maxwell-Wagner-Sillars effect [91, 92]. The dielectric constant predominantly remains constant with frequency, suggesting that there is no percolating behavior.

The planar aligned samples showed consistent behavior for all three directions tested. The dielectric constant in direction-1 and direction-2 is equal. Due to the transversely isotropic nature of GNP, this is an expected behavior and confirms the in-plane isotropy of the sample. Compared to unidirectional aligned samples, planar aligned samples have a higher dielectric constant along the in-plane direction. This can be explained by the increased availability of particles to enhance the mini capacitor effect and planar orientation which utilizes the maximum directional effects. In unidirectional alignment, the GNPs tend to form agglomerated

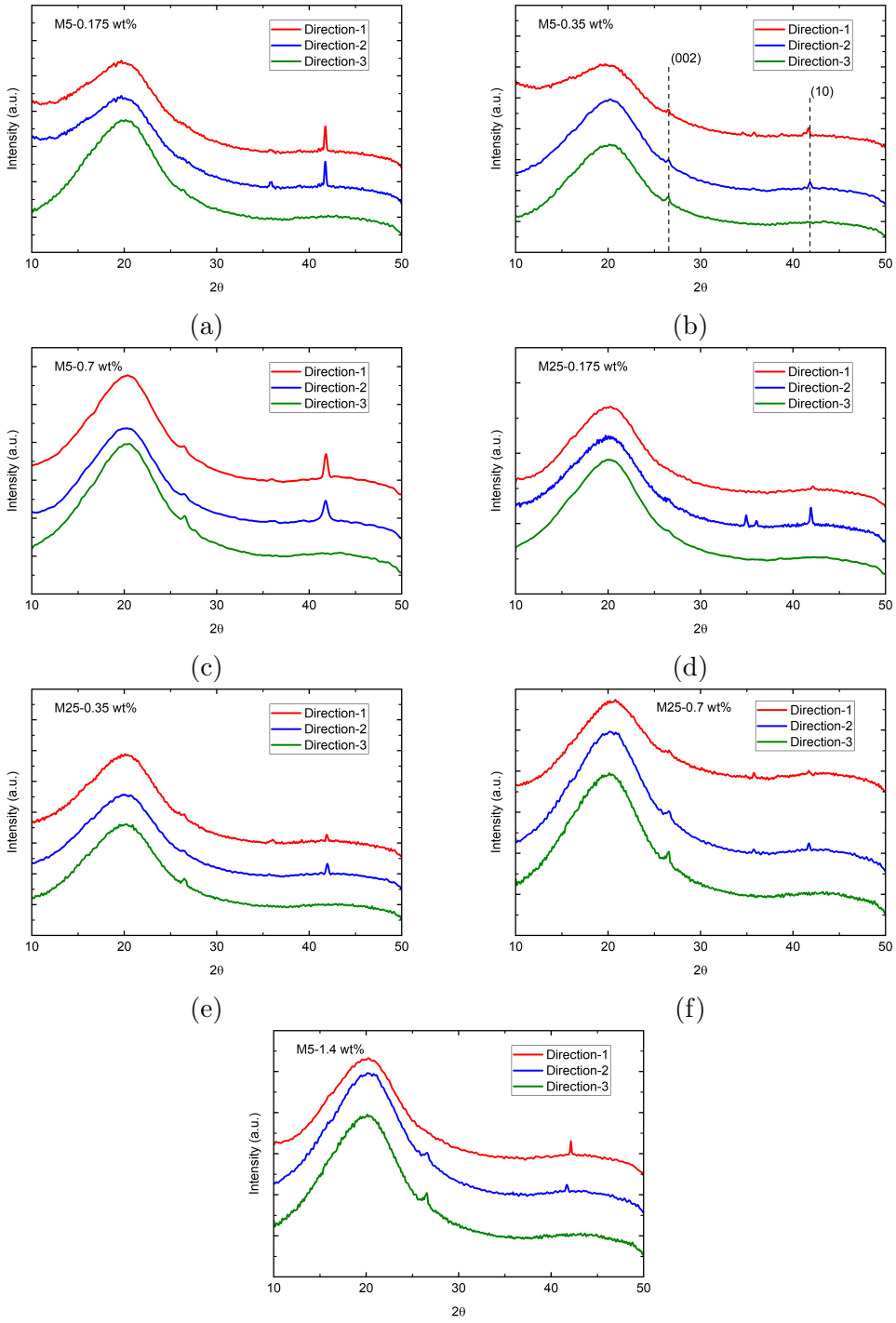

Figure 36: XRD patterns corresponding to planar aligned GNP composites of M5 and M25 for 0.175, 0.35 and 0.7 wt% concentrations. Two significant peaks ((002) & (10)) are highlighted which resemble graphene inter spacing distance and lattice constant respectively.

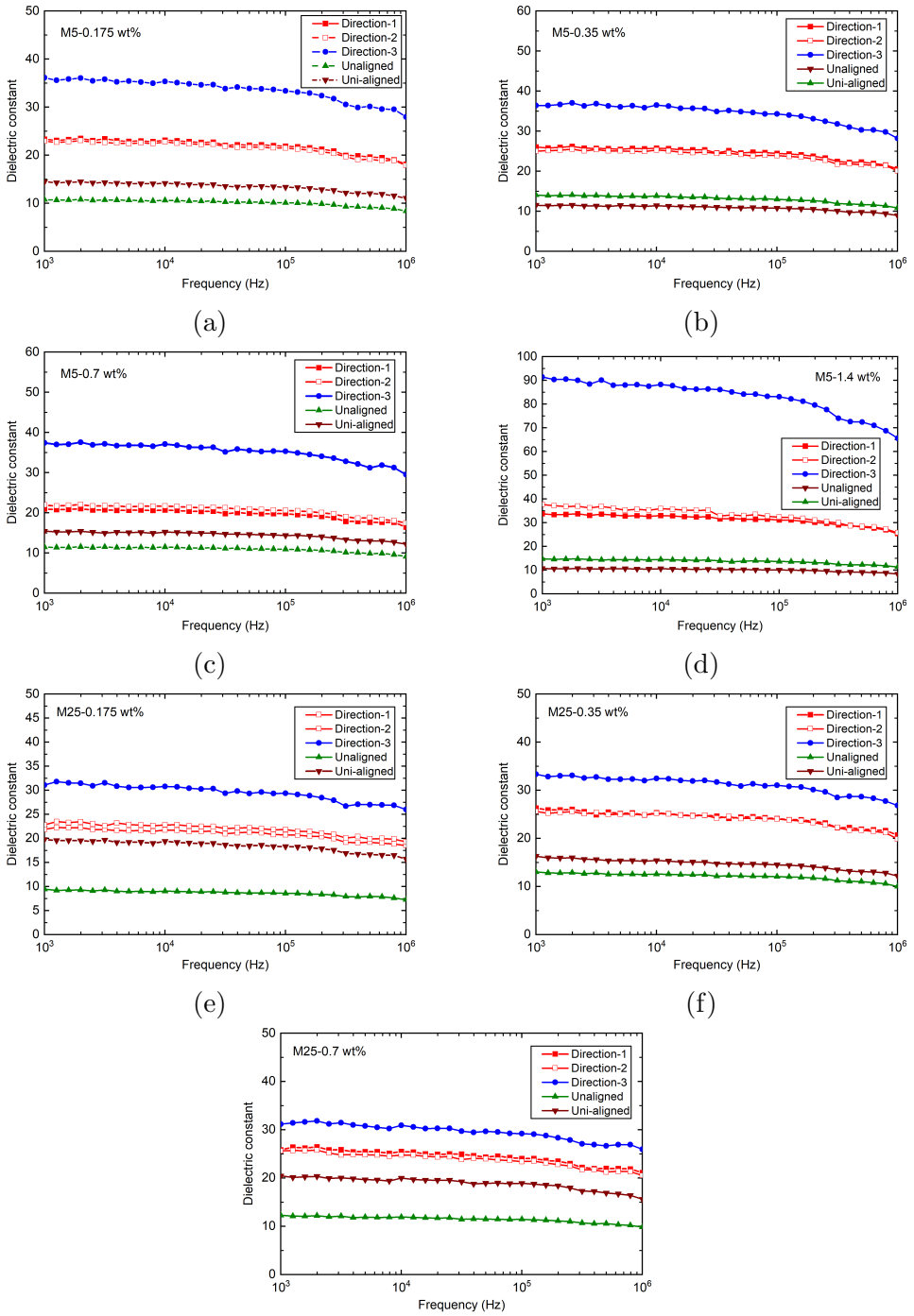

Figure 37: Dependance of dielectric constant on frequency for a) M5-0.175 wt%, b) M5-0.35 wt%, c) M5-0.7 wt%, d) M5-1.4 wt%, e) M25-0.175 wt%, f) M25-0.35 wt% and g) M25-0.7 wt% planar aligned GNPs in 3 orthogonal directions

chains which render ineffective regions that do not contribute to the dielectric constant. The mechanism of planar alignment process prevents the agglomerations due to constant attrac-

tion and repulsion of adjacent particles. Nevertheless, the dielectric constant in direction-3 is relatively higher than in-plane dielectric constants (directions 1 and 2) for all concentrations. This confirms that planar alignment has materialized for both M5 and M25 GNPs.

A previous study regarding anisotropic dielectric constant of GO sheets showed that the through-thickness dielectric constant was less than in-plane value [93]. The high in-plane dielectric constant of GO can be attributed to the abundant oxygen functional groups present on the edges and basal planes which induces a higher electronegative charge relative to positive charge density of carbon and hydrogen atoms [149]. Apart from this, GO contains defects and polarized groups such as water intercalating between its layers. The conductivity phenomena through the GO layers reduces rapidly due to functional groups and intercalating molecules [150]. However, for graphene the mechanism of dielectric behavior is purely attributed to displacement of electron cloud over the layers or along the plane of graphene. Santos and Kaxiras found that the polarization along the thickness of graphene layers is twice that of in-plane and graphene behaves as a metal along the plane and as a semiconductor perpendicular to the plane [94]. They also found that the dielectric constant was higher in through-thickness compared to in-plane direction which validates the peculiar increment in direction-3 dielectric constant of planar aligned GNPs. Apart from the intrinsic anisotropy of dielectric constant of graphene, we believe that the greater surface area of the GNPs which leads to greater interfacial polarization, relatively lower proximity of GNPs in direction-3 and lower conductivity along through-thickness direction has an influence in the higher value of dielectric constant obtained. Apart form this, we noticed a greater increment in dielectric constant for unidirectionally aligned composites of M25 compared to M5. This is due to the higher diameter of M25 GNPs which facilitates easier chain formation that results in increased dielectric constant [68].

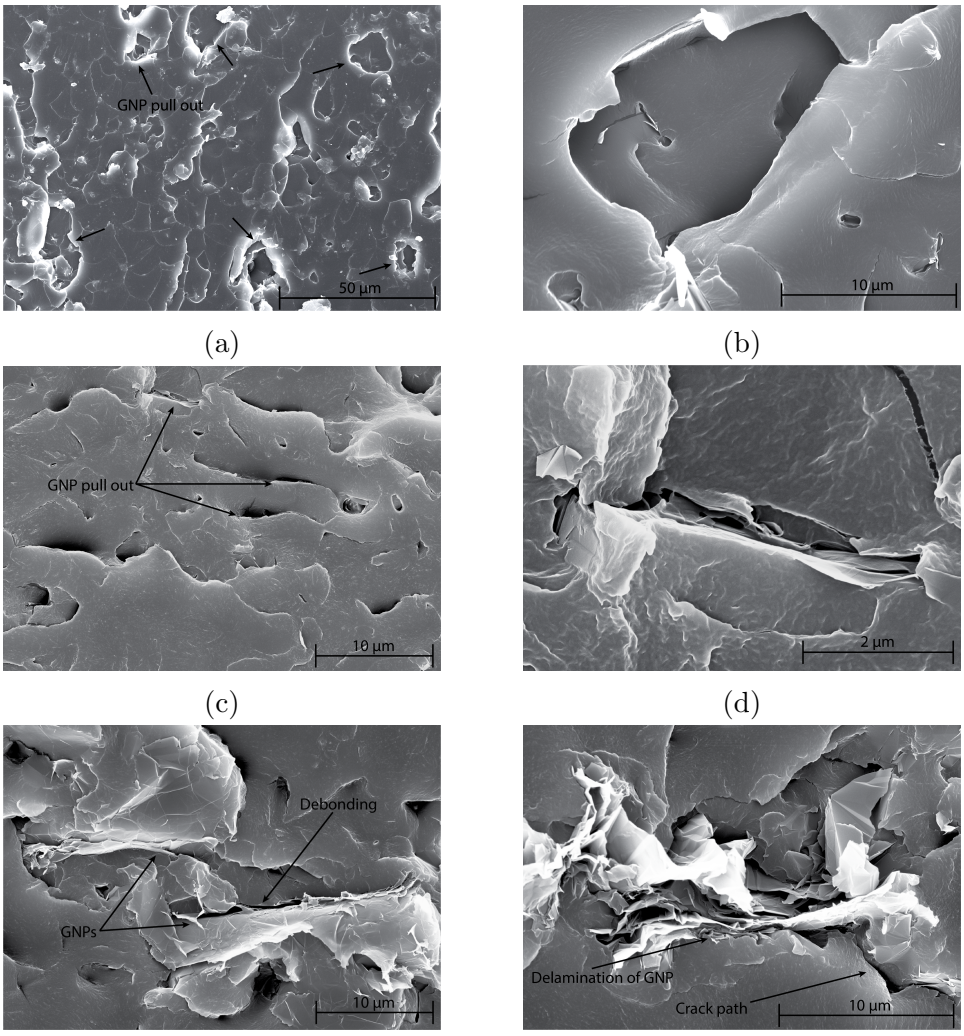

Figure 38: SEM images of fractured surfaces of planar aligned GNPs. a) planar view of 0.35 wt% M5 GNP showing various sites of GNP pull out, and b) zoomed in planar view showing the GNP pull out regions, c) out of plane view of planar aligned 0.7 wt% M25 showing multiple pull out of GNPs, d) magnified view of a GNP embedded in epoxy in the 0.7 wt% M25 sample, e) out of plane view of planar aligned 0.7 wt% M25 GNP sample showing two GNPs in close proximity and debonding during fracture and f) out of plane view of M25 GNP showing the micro crack path and delamination of GNP.

4.2.5 Fractographic analysis

Fractographic analysis was performed for the planar aligned samples. The cylindrical specimen obtained after the alignment was fractured in two different ways, parallel and perpendicular to the planar direction of oriented GNPs. Figure. 38 shows the fracture surfaces of M5-0.35 wt% and M25-0.7 wt%. Figure. 38a shows the fracture surface along the planar

direction. Here, we noticed multiple GNP pull out regions whose diameter is between 4-10 μm, which ascertains the planar alignment of GNPs. Figure. 38b shows the magnified view of the pull out sections which correspond to a GNP diameter of around 10 μm. Figure. 38c shows the fracture surface perpendicular to the planar direction. Here, The GNP pull out sections were deeper and the length of the sections correspond to the diameter of GNP. Also, the sections were aligned along the planar direction, further proving the planar alignment of GNPs. Figure. 38d shows a single GNP embedded in the epoxy aligned along the 1-3 and 2-3 planes. Debonding between epoxy and GNP, micro cracks around GNPs and delamination of GNPs are also depicted for planar aligned M25-0.7wt% GNPs in the Figs. 38f and 38e.

4.3 Conclusion

In this study transversely isotropic GNPs were successfully aligned along the in-plane directions in a in-house developed composite electrode setup capable of using a rotating electric field. The rotation speed of electric field was dependant on electric field strength, concentration and size of GNPs. Two different sizes, M5 and M25 of different concentrations i.e. 0.175, 0.35, 0.7 and 1.4 wt% were aligned along the planar direction. The alignment of GNPs was initially characterized by the AC current flowing the system in two perpendicular in-plane directions. The systematic and periodic increase of AC conductivity showed that alignment along these directions was taking place uniformly. XRD analysis of these cured samples along the three orthogonal directions identified the graphene and lattice constant of graphene. The interlaminar distance peak was more pronounced in the through-thickness XRD analysis. The two in-plane XRD patterns were comparable and they featured the peak that captures the lattice constant of graphene and this can only be recognizable in the in-plane direction, thus signifying the planar orientation of GNPs. In addition to this, dielectric spectroscopy of the planar aligned samples in three orthogonal directions showed the indistinguishable pattern of dielectric constant variation along the two in-plane directions with frequency for each concentration. Due to the inherent anisotropy exhibited by GNPs, we noticed an increase of dielectric constant along the through thickness direction. The dielectric constants of planar aligned samples were compared with unaligned and unidirectionally aligned samples. Planar aligned samples demonstrated higher dielectric constants due to availability of GNPs, lack of conduction pathways and uniform distribution of oriented GNPs. Fracture surfaces viewed under an SEM further provided proof of the planar orientation of GNPs and showed the different surface morphologies obtained by fracturing in two perpendicular orientations. The planar aligned GNP samples can also exhibit anisotropic fracture toughness.

CHAPTER V

GRAPHENE OXIDE (GO) BASED STRUCTURAL SUPERCAPACITORS (SSCs)

In this study, we develop structural supercapacitors (SSCs) capable of storing electrical energy while demonstrating structural integrity using grpahene oxide (GO) as nano fillers. The SSCs are made using a hand layup technique using various concentrations of polyethylene glycol (PEG) and lithium based ionic liquid. SSCs are made from highly activated carbon fibers as electrodes and glass fibers and polypropylene membranes as separators. The SSCs are characterized by electrochemical impedance spectroscopy (EIS), cyclic voltammetry (CV) and constant current charge discharge (CCCD).

5.1 Materials and Methods

5.1.1 Materials

The GO was procured from Nanoshel UK limited, United Kingdom. The GO was obtained in black gray powder form (1.9-2.2 g/cm^3) and the lateral size of the platelets is 10 µm while the thickness of the platellet is 1.6 nm. The content of carboxylic groups (COOH) is 1 wt%. PEG of molecular weight of 600 and 200 was purchased from Acros organics, Waltham, MA. Lithium bis(trifluoromethylsulphonyl)imide (LiTFSI) was also obtained from Acros organics, Waltham, MA. Epoxy resin (EPON 862, Hexion, Columbus, Ohio) and hardener (EPIKURE Curing agent 3274, Hexion, Columbus, Ohio) were used for dispersing the GNPs. EPON 862

is low viscosity blend of diglycidyl ether of bisphenol F. The liquid hardener is a moderately reactive low viscosity aliphatic amine. The activated carbon fibers (Kynol, Kynol Europa GmbH, Hamburg, Germany) have a surface area of 2000 m^2/g. The glass fibers (Style 120 E-glass, Fiberglast Brookville, Ohio) have a stain weave with a thickness of 0.07–0.15 mm and weighs 93 g/m. The polypropylene membrane (Celgard 3501, Celgard, Charlotte, NC) has a thickness of 25 µm and a prorsity of 55%. Acetone, Sulphuric acid (H_2SO_4), N, N-Dimethylformamide (DMF), Propylene carbonate (PC) and potassium permanganate ($KMnO_4$), were purchased from Sigma Aldrich, St. Louis, Missouri.

5.1.2 Electrolyte preparation

Initially 0.5 wt% of GO with respect to PEG was mixed with DMF with a ratio of 1 mg/ml with respect to GO weight and PEG on a magnetic stirrer at 40°C for an hour for proper dispersion. Then the solution was probe sonicated for 15 min using a ultra sound probe sonicator to break the larger agglomerates. The solution was maintained at 0°C using an ice bath to avoid unnecessary overheating of PEG. The solution was then moved to a bath sonicator for 30 minutes to exfoliate the GO sheets. The bath was maintained at 35–40°C using a mid level intensity. The DMF/PEG/GO dispersion was transferred to a vacuum oven at 60°C and the DMF was removed over a period of 12 hours by solvent extraction using dry ice. The PEG/GO mixture was transferred to a glove box. Here, LITFSi was added wit PC and stirred vigorously at 40°C until the salt was dissolved. This completes the procedure for the ionic liquid. For the structural part, epoxy is poured into a separate beaker, and is mixed with the hardening agent in a 5:2 ratio. The epoxy and ionic liquid were poured into a single beaker and mixed thoroughly. The solid polymer electrolyte (SPE) is then degassed and measured appropriately for SSC fabrication. Apart from this SPE was added to rectangular molds of 1 mm thickness for SPE chracterization.

5.1.3 Structural supercapacitor preparation

Surface activation of celgard membrane was necessary since PP membrane is highly inert and lacks good adhesion. The membrane was surface treated using microwaves and an oxidizing agent [151]. Acetone was applied to a 8 × 8" celgard separator by a brush and allowed to dry at room temperature for five minutes. The membrane was submersed in 20% (H_2SO_4) solution to clean the surface and remove any impurities. A 0.5 M solution of ($KMnO_4$) was then prepared and the celgard membrane was immersed and microwaved for 120 seconds. The microwave irradiation caused the surface to oxidize in the presence of (H_2SO_4). This makes the surface hydrophilic and also improves the wet-ability.

Two activated carbon fabric of size (6 × 3 inches) was cut and conductive copper tape was applied on one side of both the fabrics. The fabrics were then hot pressed at 100°C to ensure strong adhesion between the copper tape and the carbon fabric. The SSC was made by hand layup technique. First the carbon fabric was placed and a layer of the SPE was brushed and then the fabric was placed under vacuum to remove the air bubbles present on the surface. Then the seperator (GF or celgard) of size (7 × 4 inches) was placed and then more SPE was added and then degassed. Finally, the second carbon fabric was added with SPE penetrating the other side. The laminate was then cured in the oven at 60°C for 24 hours.

5.1.4 Summary of experiments

The advantages of GO addition towards the ionic conductivity was identified using a liquid electrolyte system. Exfoliated GO was added in 0.05 wt% increments to PEG until 1 wt% and the ionic conductivity of the liquid was tested at every increment.

SPEs were prepared for various concentrations of structural element and ionic elements. They also include incorporation of PC and lower molecular weight PEG-200.

Finally, SSCs were prepared using hand lay up technique using combinations of separators

Table 13: Summary of structural supercapacitors fabricated and their constituents. Two separators were used for glass fiber based SSCs, while celgard based SSSs have a single separator.

SSC	Seperator type	PEG+Li %	Epoxy %	PC %	GO %
SSC-GF-PC	GF	50	40	10	-
SSC-GF-PC-GO	GF	50	40	10	0.5
SSC-C	celgard	50	50	-	-
SSC-C-PC	celgard	50	40	10	-
SSC-C-PC-GO	celgard	50	40	10	0.5

and the addition of PC and the epoxy to ionic components ratio was maintained at 40:60 for all the SSCs prepared. Two glass fiber fabrics were used to ensure symmetry and preventing shorting between carbon fabric electrodes [152]. One layer of celgard separator was sufficient since the pores were small enough to prevent the electrodes from making contact with each other.

5.1.5 Material analysis and characterization

X-ray diffraction (XRD) was performed on powder samples of GO at ambient temperature using a Bruker D8 AXS (Bruker, Millerica, Massachusetts). XRD was used to determine the interlayer spacing between the nanosheets using Bragg's law.

$$d = \frac{n\lambda}{2\sin\theta} \tag{5.1.1}$$

Where d is the distance between the nanosheets, λ is the wavelength of the x-ray, and θ is the diffraction angle. The powder sample was then scanned from 10° to 40° for 30 seconds. CuKα (λ=0.154nm) radiation was generated at a voltage of 40 kV and a current of 40 mA was used as the X-ray source.

The electrochemical characterization was performed on a potentiostat (VersaSTAT 3F, Princeton applied research, Oak Ridge, Tennessee). The ionic conductivity was measured at am-

bient room temperature (20°C) and is calculated based on the electrochemical impedance spectroscopy (EIS) measurements. The ionic liquid conductivity was measured using a two probe method with square stainless steel electrodes for a frequency range of 0.01 Hz to 1 MHz. The ionic conductivity of the SPE was measured for circular samples cut by a die which are sandwiched between two stainless steel electrodes. The amplitude of signal was 100 mV. The ionic conductivity was calculated from the electrolyte resistance (R) from the impedance curve, thickness of the electrolyte or distance between electrodes for liquid electrolyte (t) and the area of the contact between the SPE or liquid with the electrodes (A). It is given by the following formula

$$\sigma = \frac{t}{R \times A} \tag{5.1.2}$$

Cyclic voltammetry (CV) was performed on the SSCs with a two-electrode system between a potential window of -1V to +1V and a scan rates of 1, 0.1, 0.01 and 0.001V/s and the electrochemical responses were recorded. Constant current charge discharge (CCCD) measurements were performed with charging currents ranging between 5–10 mA. The active mass takes into the weight of carbon fibers, seperators and SPE. The following equations were used to calculate the specific capacitance, energy density and power density of the SSCs.

$$C_p = \frac{I_m \Delta t}{\Delta V} \tag{5.1.3}$$

$$E_g = 0.5 C_p \Delta V^2 \tag{5.1.4}$$

$$P_g = \frac{E_g}{\Delta t} \tag{5.1.5}$$

Here, I_m is the current density, Δt is the discharge time, $DeltaV$ is the voltage drop of the discharge cycle, E_g is the energy density and P_g is the power density.

5.2 Results and Discussion

5.2.1 Influence of GO on ionic conductivity of ionic liquid

GO is a carbon-based material with a two-dimensional honeycomb lattice structure that shows a strong diffraction peak at $2\theta \approx 26.4^{\circ}$. This gives us an interlayer spacing of 3.36 Å between the graphene layers. This ensures the carboxylic groups are present on the outer edges on the GO plane [59].

The variation of ionic conductivity of non exfoliated GO particles is depicted in Fig. 39. GO particles have abundant carboxylic and hydroxyl groups on the edges of the basal plane of the graphene. We noticed a one order increase in ionic conductivity at 0.2 wt% of GO inclusion. This is due to the presence of the functional groups aiding in the ion transfer. After 0.2wt%, further increments of 0.05 wt% of GO to the solution decreased the ionic conductivity steadily until it plateaus at 0.6 wt%. Further addition of GO will cause the particles to agglomerate which reduces the access of lithium ions to the functional groups. It should also be noted that the GO used here is non exfoliated, hence the peak ionic conductivity was attained at lower wt%. A separate study of exfoliated GO was performed by using 0.7 wt% GO and the liquid ionic conductivity attained was 2.8 x 10^{-3} S/cm. This shows the beneficial effects of exfoliated GO and the natural tendency of GO to agglomerate due to van der Waals forces between the functional groups.

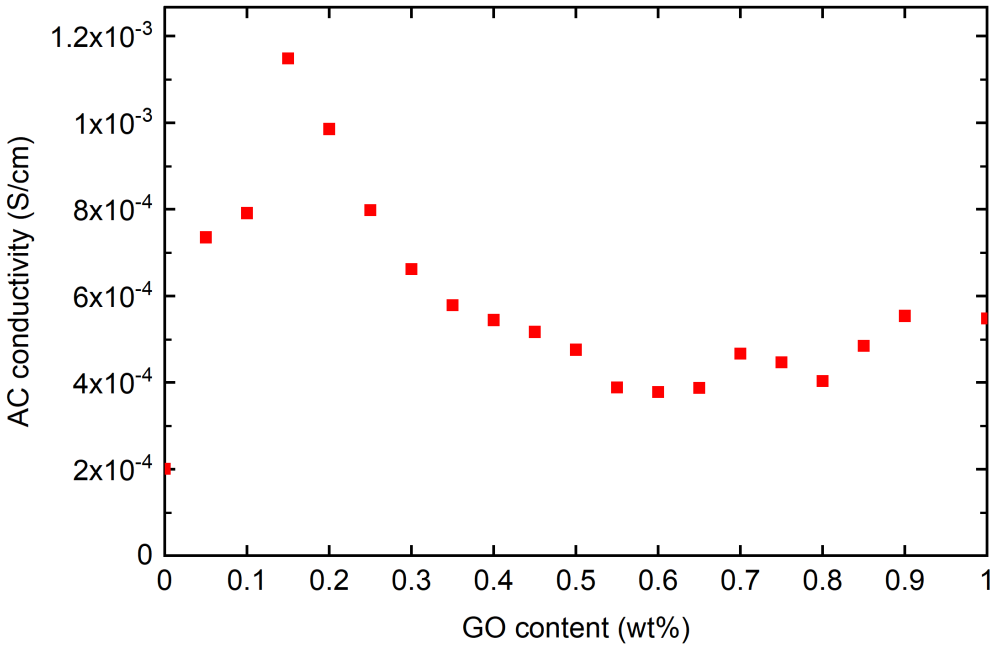

Figure 39: Variation of ionic conductivity of PEG-600 liquid electrolyte with 10 wt% LITFSI with increments of non exfoliated GO.

5.2.2 Influence of GO on ionic conductivity of solid polymer electrolyte (SPE)

Figure. 40 shows the ionic conductivity variation for 50:50 epoxy and ionic component SPE with GO wt%. Here, normal samples are prepared using bath and probe sonication according to the method specified in the materials and methods section. Additionally, some samples underwent centrifugation for 15 minutes at 10,000 RPM. Physical observation showed that the supernatant samples were well dispersed did not contain larger agglomerates of GO. Hence, the ionic conductivities of supernatant samples were relatively higher than its counter part normal samples as seen Fig. 40 . We also noticed at 0.5 wt%, the ionic conductivity was the highest. This is due to good phase separation of ionic and epoxy components because GO increases the viscosity and negatively affects phase separation which is required for achieving optimum ionic conductivity [153]. Hence, 0.5 wt% GO was chosen for fabrication of SSCs as the optimum amount to achieve good ionic properties.

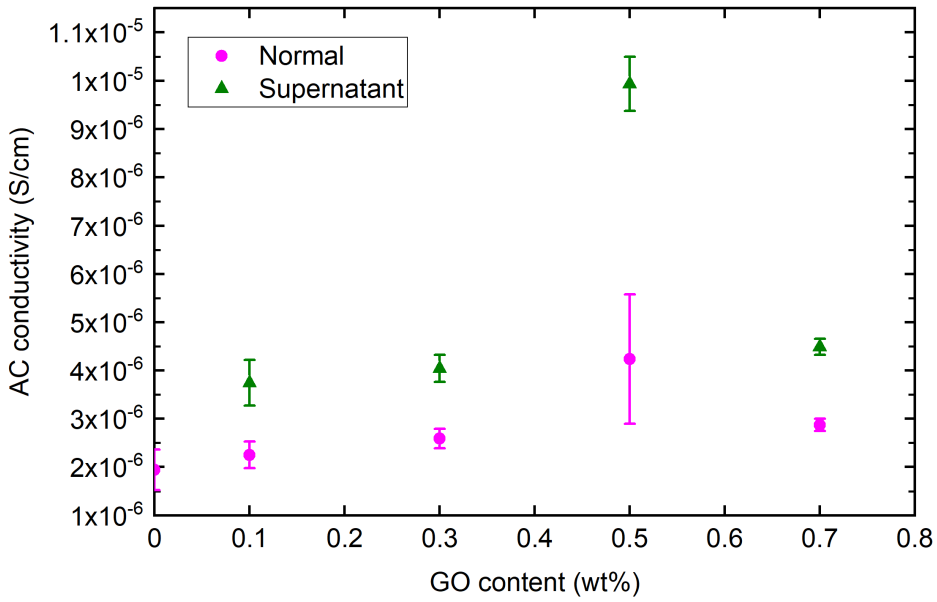

Figure 40: Variation of ionic conductivity of PEG-600 SPE with epoxy to ionic component ratio (50:50) with 10 wt% LITFSI. Here, normal sample has undergone probe and bath sonicated, whereas the supernatant sample has undergone additional 15 minutes of centrifuging.

5.2.3 GO based structural supercapacitors (SSCs)

Figure. 41 shows the SSCs prepared using handlay up technique. Figure. 42 shows the nyquist plots for various SSCs fabricated. The equivalent series resistance (ESR) obtained from the plots are reasonable for structural supercapacitor applications. Typically, the ESR depends on the electrode resistance, ionic resistance of the SPE and the characteristics of the separator. Here, the celgard has a lower ESR compared to glass fiber SSCs due to the thickness of the separators layers and also the amount of pores are higher for celgard separator. We also noticed a greater decrease in ESR as PC is added for celgard SSC compared to glass fiber SCCs. PP is a plasticzer which aids in improvement of the ionic conductivity by reducing the viscosity of the SPE. However, we noticed negligible effect of PC in regards to ESR for glass fiber SSCs. Morever, when GO was introduced to the celgard SSC, the ESR rose slightly. This maybe due to GO size being larger then the celgard pores which result in blockage and reduction in amount of accessible pores. The presence of GO

would not affect GF SCCs due to the gaps in glass fiber mat are larger than GO particles.

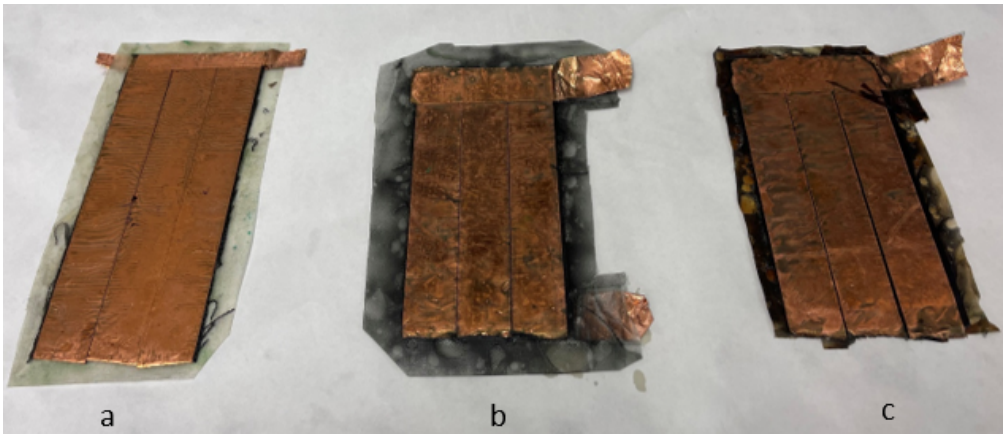

Figure 41: Photographs of SSCs. a) SSC-GF, b) SSC-GF-PC-GO and c) SSC-C-PC-GO

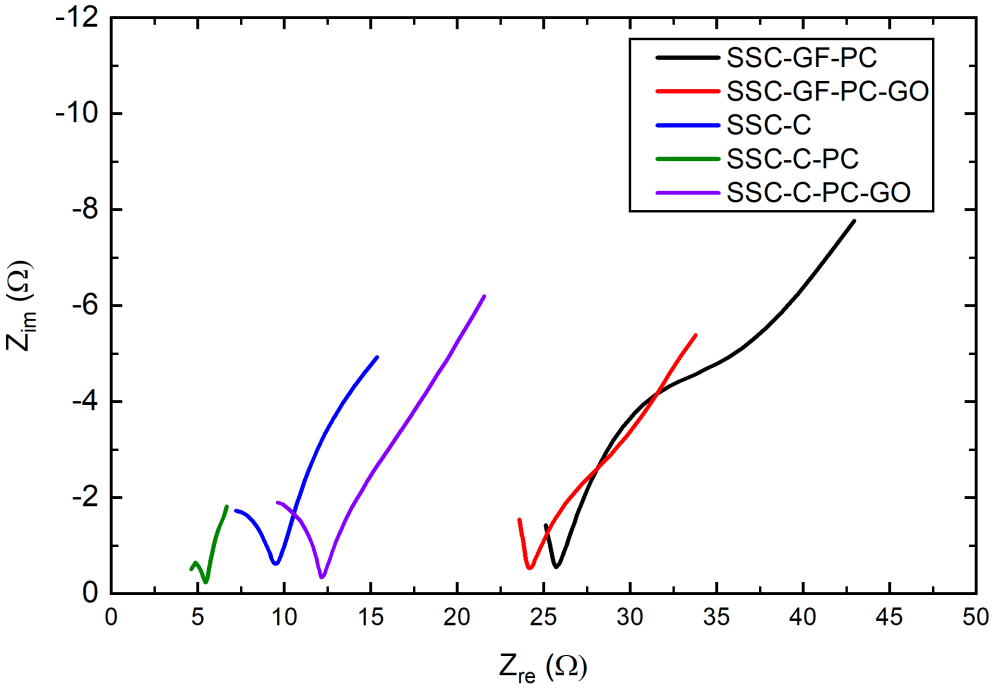

Figure 42: Nyquist plots of the EIS data obtained from the potentiostat for various SSCs.

Figure. 43 shows the cyclic voltammograms obtained between for a voltage window of 0 and 1 V for glass fiber based SSCs. The CV curves showed good cyclability for all the scan rates tested. The area under the CV curve was low for SSC-GF-PC, since the GF is a poor ion conductor. However, The CV area and the current density improved upon adding GO, proving the ionic conductivity improvements as well as plasticizing the SPE to allow more current flow. Figure. 44 shows the rate-dependant cyclic voltammograms obtained for

Table 14: Comparison of electrical properties of glass fiber and celgard based SSCs.

SSC	Volumetric capacitance mF/cm^3	Specific capacitance mF/g	Energy density mWh/kg	Power density mW/kg
SSC-GF-PC	20.4	161.0	3.1	181.2
SSC-GF-PC-GO	36.6	258.0	2.4	142.3
SSC-C	28.9	174.0	4.9	183.2
SSC-C-PC	36.2	220.7	5.3	187.0
SSC-C-PC-GO	45.3	329.3	5.8	208.3

celgard based SSCs. Here, good cyclability is seen and at lower scan rates the ions have enough time to intercalate into the carbon fabric. The CV curves improved upon addition of PC as expected. The volumetric and specific capacitance were calculated based on the 0.001 V/s CV curve which exhibits the highest capacitance as seen in Table.14. Although incorporating GO increased the ESR of the SSCs, it had a positive effect on capacitance for both glass fiber and celgrard based SSCs due to its ion transfer properties associated with its higher surface area. SSC-C-PC-GO has the highest capacitance amongst the fabricated SSCs. This can be associated with higher number of pores and lower thickness allowing ions to pass through easily.

Figure. 45 shows the charge discharge curves for glass fiber based SSCs for three different currents (2, 5 and 10 mA). The capacitors were allowed to chrage to 2 V and discharged to 0 V. Five cycles were performed for each SSC but only the final cycle is depicted. When high current such as 10 mA is applied the ions have higher enegry to dissociate and move through the separator membrane. It took less than 10 seconds to charge the SSC-GF-PC SSC as seen in Fig. 45a. As the current is lowered the SSC takes more time to reach 2 V due to lower threshold for ion dissociation. The SSC was able to charge successfully when the current was 5 mA and 10 mA, whereas for the case of 2 mA, the SSC had reached its maximum voltage capability. This can be explained by the formation of a double layer near the carbon fibers, which resists further accumulation of charge for a given low current. Figure. 45b shows the charge discharge curves when GO is introduced. Despite having an increment in specific capacitance, GO had a negative effect on the energy and power densities for glass

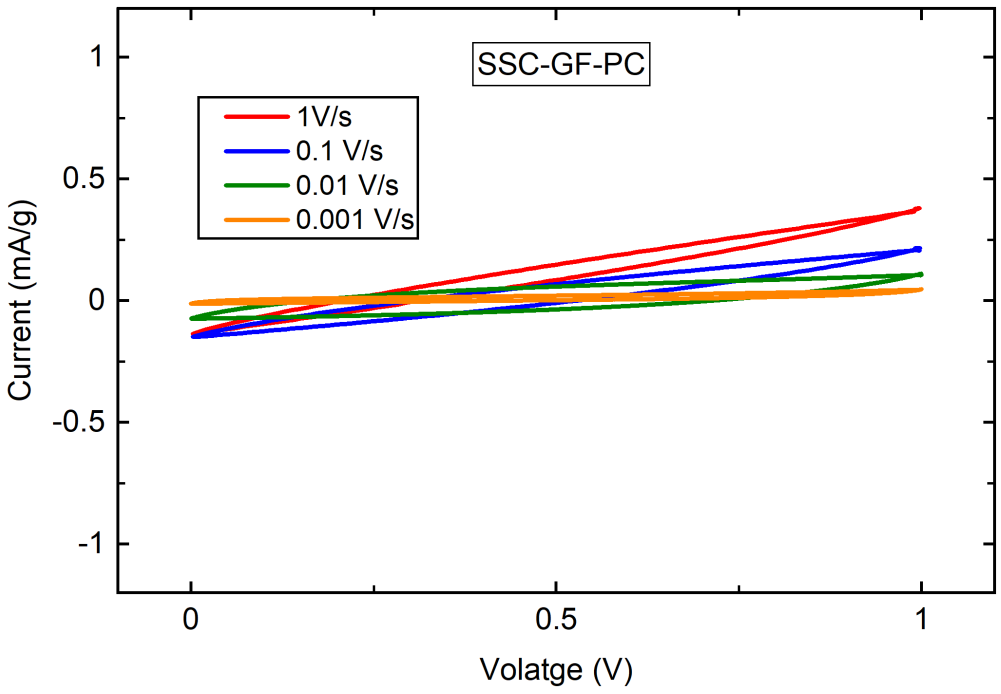

(a)

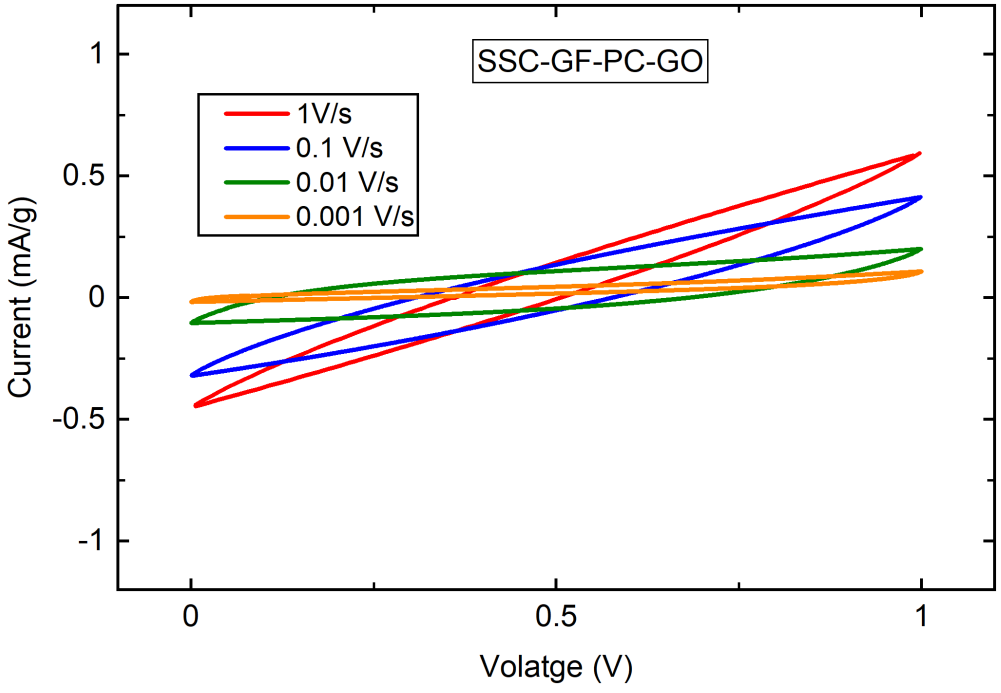

(b)

Figure 43: Cyclic voltammograms of glass fiber based SSCs. a) SSC with PC b) SSC with PC and 0.5 wt% of GO with respect to PEG

fiber based SSC as seen in Table.14. A study on tetraethylammonium tetrafluoroborate ($TEABF_4$)/PC based supercapacitors also showed higher capacitance due to incorporation

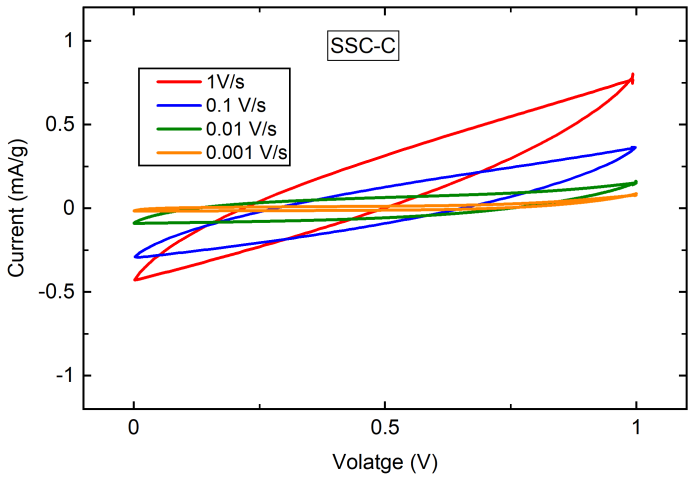

(a)

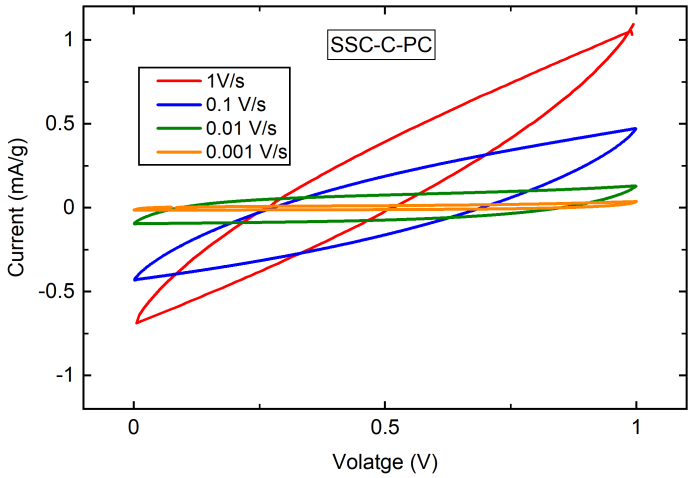

(b)

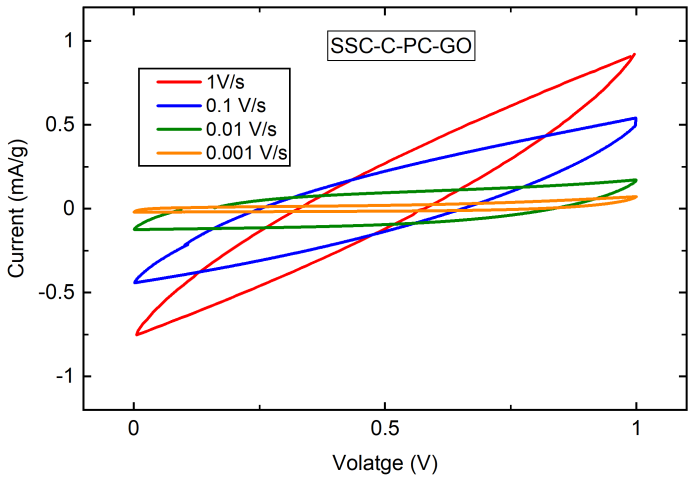

(c)

Figure 44: Cyclic voltammograms of celgard based SSCs. a) Plain SSC b) SSC with PC and c) SSC with PC and 0.5 wt% of GO with respect to PEG

of PC but it slowed down the ion transport leading to lower power density. This phenomenon was associated with the increase of solvated cation size which reduces the ability of ions to penetrate into the slits of carbon fibers and also the van der Walls forces increase which lowers the ion transport [154]. Regardless of current, the SSC was not able to charge to the expected 2 V. This may be related to the agglomeration of GO in the system. This issue needs more clarity and have to be looked into further.

Figure. 46 shows the charge discharge curves for glass fiber based SSCs for three different currents (2, 5 and 10 mA). The lower thickness and high porosity of celgard separator allowed better ion transfer compared to glass fiber separator. The lower proximity of electrodes also creates a stronger double layer which increases the energy and power densities as seen in Table.14. The effect of PC is clearly visible which shows the effect of improvement of ionic conductivity has on its CD characteristics. For a low current of 2 mA, the SSC was able to charge up to 1.8 V. Similar to glass fiber SSC, the effect of GO seems to have a negative effect on its maximum charge capacity. However, the discharge time was comparable for SSC-C-PC-GO and SSC-C-PC which was 100 seconds. However, SSC-C-PC-GO had a lower voltage drop and also was only charged to 1.8 V. This manifested a higher performance amongst the celgard SSCs with the highest power and energy densities of 201.3 mW/kg and 5.6 mWh/kg respectively. Further analysis has to be made regarding the pore blockage due to GO agglomerates.

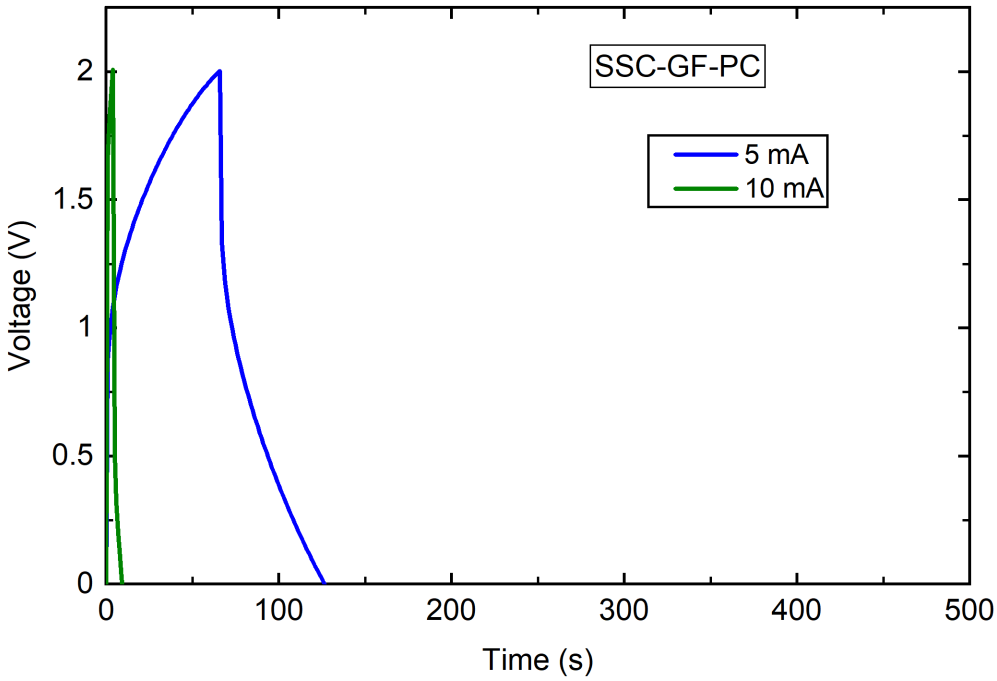

(a)

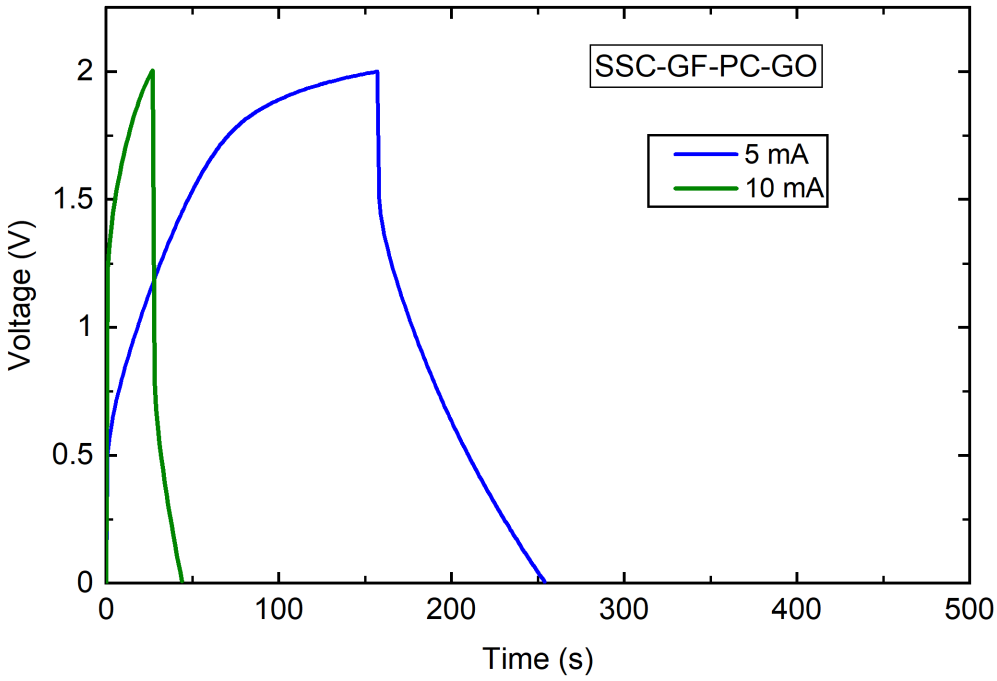

(b)

Figure 45: Constant current charge discharge cycles of glass fiber based SSCs for various currents. a) SSC with PC b) SSC with PC and 0.5 wt% of GO with respect to PEG

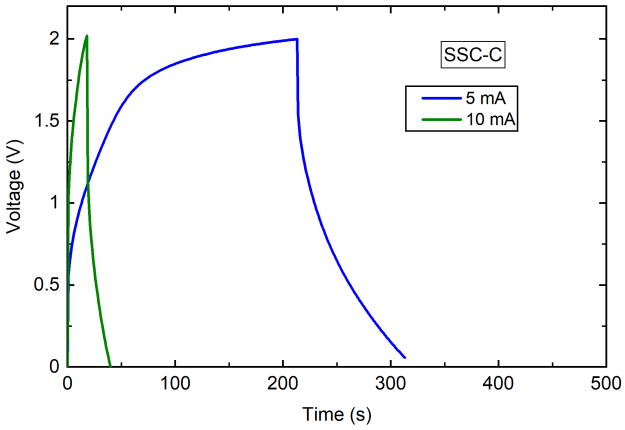

(a)

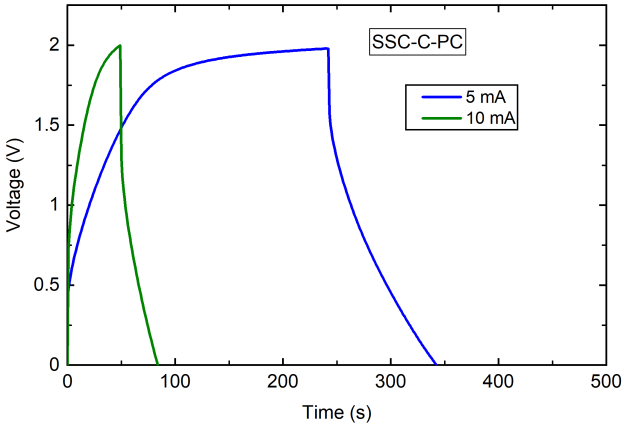

(b)

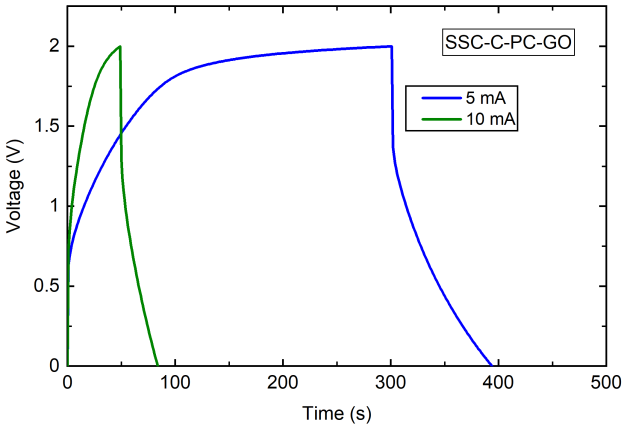

(c)

Figure 46: Constant current charge discharge cycles of celgard based SSCs for various currents. a) Plain SSC b) SSC with PC and c) SSC with PC and 0.5 wt% of GO with respect to PEG

5.3 Conclusion

In this study structural supercapacitors based on glass fiber and celgrad separators were developed using hand layup technique. Highly activated carbon fiber fabrics were used as electrodes and graphene oxide was added to the PEG based ionic liquid to improve its ionic and structural properties. We noticed a one order increase in ionic conductivity when 0.15 wt% non exfoliated GO was introduced in PEG-600 ionic liquid. The solid polymer electrolyte based on 0.5 wt% GO saw a 100% increase when it was compared to SPE which does not include GO. However, when the SPE was made of supernatant, we noticed an order increase in ionic conductivity. This is due to presence of hydroxyl and carboxyl fucntional gruops on GO for ion transfer as well as plasticizing effects demonstrated by GO. The SPE formulation of 50 wt% ionic component 50 wt% structural component was used to manufacture SSCs for glass fiber and celgard separators. The amount of LITFSI of 10 wt% with respect to PEG was found to be optimum. The SPE formulation had to be modified for GF and celgard based SSCs by incorporating 10 wt% propylene carbonate (PC), which showed promising results in reducing the electrochemical series resistance (ESR) of SSCs. The volumetric capacitance for celgard based SSC without PC was 28.9 mF/cm^3 and with PC was 36.2 mF/cm^3. Specific capacitance also increased from 174.0 to 220.7 mF/g for the same. Celgard proved to be a better separator due to its high porosity (55%) and lower thickness (25μm) compared to glass fiber separator whose thickness was 4 times higher. Introduction of GO to glass fiber composites had a detrimental effect on the energy and power densities. However, the specific capacitance of glass fiber SSC increased after adding GO from 161.0 to 258 mF/g. This peculiar effect needs more research on the agglomeration effects on charge discharge cycles. On the contrary, adding GO to celgard based SSCs proved to be fruitful and we achieved a specific capacitance, energy density and power density of 329.3 mF/g, 5.8 mWh/kg and 201.3 mW/kg respectively. The structural properties of these SSCs have to be determined and further fabrication of SSCs should be made using supernantant of ionic liquid which could eliminate the larger agglomerates of GO that are unfavourable to both

ionic and structural properties.

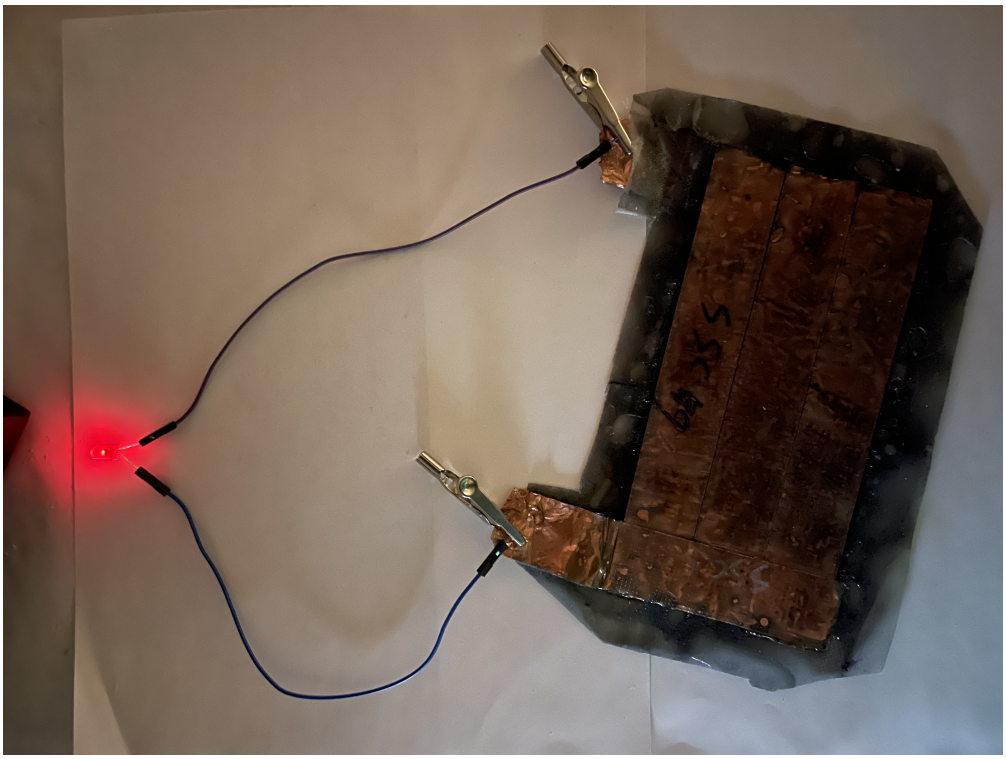

(a)

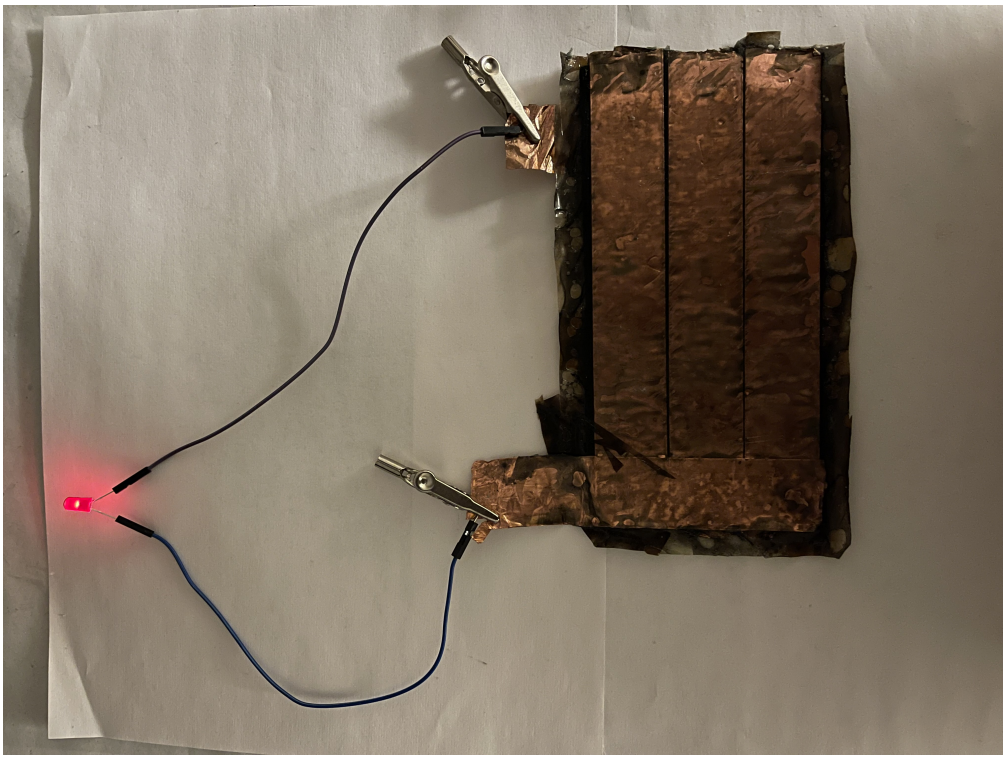

(b)

Figure 47: Structural supercapacitors powering a LED at 2V a) SSC-GF-PC-GO b) SSC-celgrad-PC-GO

CHAPTER VI

SUMMARY

The major conclusions from this study are summarized below:

- Extensive literature review was completed to obtain information on electrical conduction through carbon fiber reinforced polymer (CFRP) composites. The need to study the behavior under constant low direct currents and its significance to lightning strikes and structural supercapacitors was highlighted.

- Mechanical strength degradation of CFRP laminates due to low-density direct current and pertaining mechanisms involved have been identified. Experimental results show that the electrical degradation in CFRP is a cumulative effect of thermal and electrical effects and the damage occurs very early under these circumstances. The observed degradation is caused by the following phenomenon, thermal decomposition of the epoxy due to resistive heating, dielectric breakdown at the carbon fiber–epoxy interface and thermal mismatch during heating and cooling of the laminates.

- A reduction in ultimate compressive strength, Young's modulus in the thickness direction, glass transition temperature and an increment of $\tan\delta$ values was observed for degraded samples. The through-thickness resistivity measurements showed the extent of delamination in degraded samples and in-plane resistivity changes revealed the effects of Joule heating and subsequent reduction of resistance due to dielectric break-

down of polymer leading to a more conductive but degraded sample over time. CT scan images showed the extent of dielectric breakdown between plies that led to delamination and matrix decomposition caused by the heat generated by Joule heating of carbon fibers.

- Significant variation between in-plane and through-thickness electrical and thermal conductivity played a dominant role towards the electrical degradation of CFRP laminates. Incorporation of aligned graphene between CFRP plies can significantly improve the through-thickness properties that will aid in suppressing the damaging effects of electrical conduction. Aligned GNPs are also responsible for manifesting multifunctional properties.

- A novel semi-empirical method using AC conductivity measurements to qualitatively assess the degree of alignment for higher weight concentrations of GNPs was discovered. AC conductivity observations showed that the time required for alignment has a strong dependence on concentration of GNPs, viscosity of the epoxy/GNP blend and electric field intensity. Contemporary analytical models fail to address the effects of these parameters for alignment.

- The quality of alignment predicted by AC conductivity measurements taken during the process of alignment were substantiated by dielectric properties such as dielectric constant, dielectric loss, and AC conductivity, and Young's modulus values obtained from cured samples. Higher electric fields will have faster rotation and translation times which reduces the possibility of deleterious agglomerate formations.

- The effect of browninan motion was also studied using AC conductivity measurements and it was found that the brownian motion was prevalent in the early stages and gradually reduces with time as particles were held together as chain formation commenced. Besides this, we also found that the application of alignment results in a heterogeneous

composite due to localized effects of electric field, non responsive regions of agglomerations and stacked up percolated chains.

- Transversely isotropic GNPs were successfully aligned along the in-plane directions in a in-house developed composite electrode setup capable of using a rotating electric field. The rotation speed of electric field was dependant on electric field strength, concentration and size of GNPs.

- The alignment of GNPs was initially characterized by the AC current flowing the system in two perpendicular in-plane directions. The systematic and periodic increase of AC conductivity showed that alignment along these directions was taking place uniformly.

- Dielectric spectroscopy of the planar aligned samples in three orthogonal directions showed the indistinguishable pattern of dielectric constant variation along the two in-plane directions with frequency for each concentration. Due to the inherent anisotropy exhibited by GNPs, we noticed an increase of dielectric constant along the through thickness direction. Planar aligned samples demonstrated higher dielectric constants due to availability of GNPs, lack of conduction pathways and uniform distribution of oriented GNPs. The low value of loss tangent acquired for planar GNPs demonstrates the benefits for charge storage applications.

- XRD analysis of the planar aligned samples performed along three orthogonal directions identified the graphene interlayer distance and lattice constant of graphene. The interlayer distance was more pronounced in the through-thickness XRD analysis. The two in-plane XRD patterns were comparable and the peak for lattice constant of graphene was identified which was absent in the through-thickness XRD results.

- SEM images of the fractured surfaces in two perpendicular directions showed the different surface morpohologies and the pull out of GNPs were unique in both surfaces

and further proved the manifestation of the planar alignment in epoxy.

CHAPTER VII

FUTURE WORK

The prospective work is summarized below:

- Study of electrical degradation on cross-ply CFRP laminates highlighted the damage mechanisms such as thermal mismatch, dielectric breakdown and thermal decomposition. These mechanisms led to micro delamination as evidenced from micro CT scans and through thickness resistivity measurements. To counter these detrimental damage GNPs can be incorporated in the epoxy. To benefit from the anistropic properties experienced by GNPs such as electrical and thermal conductivity, alignment of GNPs can be performed during composite manufacturing. The aligned GNPs can form a conductive path between the carbon fiber plies and has the potential to reduce electrothermal effects leading to micro delamination.

- Unidirectional alignment of GNPs identified the factors affecting alignment such as viscosity of the epoxy/GNP, dimensions of GNP and electric field strength. The alignment kinetics of GNPs in higher weight fractions are different compared to lower concentrations. Due to high possibility of establishing conductive chains prior to alignment for higher concentrations, which fades the electric field in that region. This prevents alignment from taking place in this local region. Alignment also results in migration of GNPs depriving some regions of particles leading to a heterogeneous nanocomposite. These phenomena needs more understanding and small scale samples can be fabri-

cated with controlled alignment. This allows micro scale testing of chain formation and migration.

- Planar alignment has led to developing a nanocomposite capable of depicting transversely isotropic properties. It also utilizes the maximum surface area of the nanoparticles added into epoxy. The structured distribution of these GNPs improved the dielectric constant of the material due to mini capacitor effect. This study can be extended to particles that possess higher dielectric constants which has a higher emphasis on energy storage and energy dispersion in flexible electronics. Planar alignment of GNPs also exhibits anisotropic mechanical and fracture properties. GNPs have been researched tremendously due to their ability to resist fracture and improve the toughness of the materials. More research can done to study the fracture behaviour of these materials which may be suitable for high strain rate applications.

- Future work for structural supercapacitors (SSCs) include mechanical testing of laminates to understand the effects of graphene oxide (GO) on its mechanical properties. Tensile, compression and three point bend tests can be performed. The glass fiber separator thickness which is 120μm has a detrimental effect on the capacitance and energy properties of SSC. The relatively larger weave gaps promote shorting. Hence, more efficient glass fiber separators must be utilized which have lower thickness and tighter weave. In addition to this, SSCs should be fabricated with supernatant of exfoliated GO so the effects of GO agglomeration can be minimized. The ionic conductivity of present SPE with addition of GO was suitable but not optimum for SSCs. Hence, more conductive polymer or bi-phase polymer systems must be looked into.

REFERENCES

[1] N. Forintos, T. Czigany, Multifunctional application of carbon fiber reinforced polymer composites: Electrical properties of the reinforcing carbon fibers – A short review, Composites Part B: Engineering 162 (August 2018) (2019) 331–343. doi:10.1016/j.compositesb.2018.10.098.

[2] M. Gagné, D. Therriault, Lightning strike protection of composites, Progress in Aerospace Sciences 64 (2014) 1–16. doi:10.1016/j.paerosci.2013.07.002.

[3] F. A. Fisher, A. J. Plumer, R. A. Perala, Aircraft lightning protection handbook. Techincal Report, US Department of Transportation - federal Aviation Administration, Tech. Rep. September (1989).

[4] C. C. Goodloe, Lightning Protection Guidelines for Aerospace Vehicles. National Aeronautics and Space Administration, Tech. Rep. May (1999).
URL `http://ntrs.nasa.gov/archive/nasa/casi.ntrs.nasa.gov/20000004589.pdf`

[5] Lightning qualification test techniques for aerospace vehicles and hardware, Tech. rep. (1983).

[6] V. Kumar, T. Yokozeki, C. Karch, A. A. Hassen, C. J. Hershey, S. Kim, J. M. Lindahl, A. Barnes, Y. K. Bandari, V. Kunc, Factors affecting direct lightning strike damage to fiber reinforced composites: A review, Composites Part B: Engineering 183 (October 2019) (2020) 107688. doi:10.1016/j.compositesb.2019.107688.

[7] S. Mall, B. L. Ouper, J. C. Fielding, Compression strength degradation of nanocom-

posites after lightning strike, Journal of Composite Materials 43 (24) (2009) 2987–3001. doi:10.1177/0021998309345337.

[8] I. Y. Telitchev, R. L. Sierakowski, O. I. Zhupanska, Low-velocity impact testing of electrified composites: Part I - Application of electric current, Experimental Techniques 32 (2) (2008) 35–38. doi:10.1111/j.1747-1567.2007.00223.x.

[9] I. Y. Telitchev, R. L. Sierakowski, O. I. Zhupanska, Low-velocity impact testing of electrified composites: Part II - Experimental setup and preliminary results, Experimental Techniques 32 (3) (2008) 53–57. doi:10.1111/j.1747-1567.2007.00244.x.

[10] A. M. Amaro, P. N. Reis, J. B. Santos, M. J. Santos, M. A. Neto, Effect of the electric current on the impact fatigue strength of CFRP composites, Composite Structures 182 (September) (2017) 191–198. doi:10.1016/j.compstruct.2017.09.032.

[11] M. F. Haider, P. K. Majumdar, S. Angeloni, K. L. Reifsnider, Nonlinear anisotropic electrical response of carbon fiber-reinforced polymer composites, Journal of Composite Materials 52 (8) (2018) 1017–1032. doi:10.1177/0021998317719999.

[12] Q. Zhao, K. Zhang, S. Zhu, H. Xu, D. Cao, L. Zhao, R. Zhang, W. Yin, Review on the electrical resistance/conductivity of carbon fiber reinforced polymer, Applied Sciences (Switzerland) 9 (11). doi:10.3390/app9112390.

[13] A. E. Zantout, O. I. Zhupanska, On the electrical resistance of carbon fiber polymer matrix composites, Composites Part A: Applied Science and Manufacturing 41 (11) (2010) 1719–1727. doi:10.1016/j.compositesa.2010.08.010.

[14] Y. Chekanov, R. Ohnogi, S. Asai, M. Sumita, Electrical properties of epoxy resin filled with carbon fibers, Journal of Materials Science 34 (22) (1999) 5589–5592. doi:10.1023/A:1004737217503.

[15] R. F. Gibson, A review of recent research on mechanics of multifunctional composite materials and structures, Composite Structures 92 (12) (2010) 2793–2810. doi:10.1016/j.compstruct.2010.05.003.

[16] K. Chung, J. Seferis, J. Nam, Investigation of thermal degradation behavior of polymeric composites: Prediction of thermal cycling effect from isothermal data, Composites Part A: Applied Science and Manufacturing 31 (9) (2000) 945–957. doi:10.1016/S1359-835X(00)00043-9.

[17] D. Chung, Thermal analysis of carbon fiber polymer-matrix composites by electrical resistance measurement, Thermochimica Acta 364 (1-2) (2000) 121–132. doi:10.1016/S0040-6031(00)00631-6.

[18] P. E. Irving, C. Thiagarajan, Fatigue damage characterization in carbon fibre composite materials using an electrical potential technique, Smart Materials and Structures 7 (4) (1998) 456–466. doi:10.1088/0964-1726/7/4/004.

[19] S. Wang, D. D. L. Chung, Self-sensing of flexural strain and damage in carbon fiber polymer-matrix composite by electrical resistance measurement, Carbon 44 (13) (2006) 2739–2751. doi:10.1016/j.carbon.2006.03.034.

[20] D. C. Seo, J. J. Lee, Damage detection of CFRP laminates using electrical resistance measurement and neural network, Composite Structures 47 (1-4) (1999) 525–530. doi:10.1016/S0263-8223(00)00016-7.

[21] Z. Xia, T. Okabe, J. B. Park, W. A. Curtin, N. Takeda, Quantitative damage detection in CFRP composites: Coupled mechanical and electrical models, Composites Science and Technology 63 (10) (2003) 1411–1422. doi:10.1016/S0266-3538(03)00083-6.

[22] S. T. Kotikalapudi, R. P. Singh, Mechanical strength degradation of carbon fiber polymer matrix composites exposed to constant low-density direct current, ASME In-

ternational Mechanical Engineering Congress and Exposition, Proceedings (IMECE) 12 (November 2019). doi:10.1115/IMECE2019-12259.

[23] P. Feraboli, M. Miller, Damage resistance and tolerance of carbon/epoxy composite coupons subjected to simulated lightning strike, Composites Part A: Applied Science and Manufacturing 40 (6-7) (2009) 954–967. doi:10.1016/j.compositesa.2009.04.025.

[24] P. Feraboli, H. Kawakami, Damage of carbon/epoxy composite plates subjected to mechanical impact and simulated lightning, Journal of Aircraft 47 (3) (2010) 999–1012. doi:10.2514/1.46486.

[25] D. R. Dhakal, P. Lamichhane, K. Mishra, T. L. Nelson, R. K. Vaidyanathan, Influence of graphene reinforcement in conductive polymer: Synthesis and characterization, Polymers for Advanced Technologies 30 (9) (2019) 2172–2182. doi:10.1002/pat.4650.

[26] H. Kawakami, P. Feraboli, Lightning strike damage resistance and tolerance of scarf-repaired mesh-protected carbon fiber composites, Composites Part A: Applied Science and Manufacturing 42 (9) (2011) 1247–1262. doi:10.1016/j.compositesa.2011.05.007.

[27] P. Lamichhane, D. R. Dhakal, S. Chaudhari, I. N. Jayalath, T. Nelson, C. Park, K. Yousefpour, F. D. Blum, R. Vaidyanathan, Polyaniline doped graphene thin film to enhance the electrical conductivity in carbon fiber-reinforced composites for lightning strike mitigation, Journal of Composite Materials 55 (29) (2021) 4445–4455. doi:10.1177/00219983211041751.

[28] W. Qin, F. Vautard, L. T. Drzal, J. Yu, Mechanical and electrical properties of carbon fiber composites with incorporation of graphene nanoplatelets at the fiber-matrix interphase, Composites Part B: Engineering 69 (2015) 335–341. doi:10.1016/j.compositesb.2014.10.014.

[29] E. Kandare, A. A. Khatibi, S. Yoo, R. Wang, J. Ma, P. Olivier, N. Gleizes, C. H. Wang, Improving the through-thickness thermal and electrical conductivity of car-

bon fibre/epoxy laminates by exploiting synergy between graphene and silver nanoinclusions, Composites Part A: Applied Science and Manufacturing 69 (2015) 72–82. doi:10.1016/j.compositesa.2014.10.024.

[30] Y. Li, H. Zhang, Z. Huang, E. Bilotti, T. Peijs, Graphite Nanoplatelet Modified Epoxy Resin for Carbon Fibre Reinforced Plastics with Enhanced Properties, Journal of Nanomaterials 2017. doi:10.1155/2017/5194872.

[31] K. A. Imran, K. N. Shivakumar, Graphene-modified carbon/epoxy nanocomposites: Electrical, thermal and mechanical properties, Journal of Composite Materials 53 (1) (2019) 93–106. doi:10.1177/0021998318780468.

[32] S. G. Prolongo, A. Jimenez-Suarez, R. Moriche, A. Ureña, In situ processing of epoxy composites reinforced with graphene nanoplatelets, Composites Science and Technology 86 (2013) 185–191. doi:10.1016/j.compscitech.2013.06.020.

[33] J. R. Potts, D. R. Dreyer, C. W. Bielawski, R. S. Ruoff, Graphene-based polymer nanocomposites, Polymer 52 (1) (2011) 5–25. doi:10.1016/j.polymer.2010.11.042.

[34] P. Barber, S. Balasubramanian, Y. Anguchamy, S. Gong, A. Wibowo, H. Gao, H. J. Ploehn, H. C. Z. Loye, Polymer composite and nanocomposite dielectric materials for pulse power energy storage, Materials 2 (4) (2009) 1697–1733. doi:10.3390/ma2041697.

[35] K. Subhani, X. Jin, P. J. Mahon, A. Kin Tak Lau, N. V. Salim, Graphene aerogel modified carbon fiber reinforced composite structural supercapacitors, Composites Communications 24 (December 2020) (2021) 100663. doi:10.1016/j.coco.2021.100663.

[36] Y. Cheng, S. Lu, H. Zhang, C. V. Varanasi, J. Liu, Synergistic effects from graphene and carbon nanotubes enable flexible and robust electrodes for high-performance supercapacitors, Nano Letters 12 (8) (2012) 4206–4211. doi:10.1021/nl301804c.

[37] J. Liang, Y. Wang, Y. Huang, Y. Ma, Z. Liu, J. Cai, C. Zhang, H. Gao, Y. Chen, Electromagnetic interference shielding of graphene/epoxy composites, Carbon 47 (3) (2009) 922–925. doi:10.1016/j.carbon.2008.12.038.

[38] T. Kuilla, S. Bhadra, D. Yao, N. H. Kim, S. Bose, J. H. Lee, Recent advances in graphene based polymer composites, Progress in Polymer Science (Oxford) 35 (11) (2010) 1350–1375. doi:10.1016/j.progpolymsci.2010.07.005.

[39] H. Kim, K. Y. Park, J. Hong, K. Kang, All-graphene-battery: Bridging the gap between supercapacitors and lithium ion batteries, Scientific Reports 4 (2014) 1–8. doi:10.1038/srep05278.

[40] K. S. Novoselov, V. I. Fal'Ko, L. Colombo, P. R. Gellert, M. G. Schwab, K. Kim, A roadmap for graphene, Nature 490 (7419) (2012) 192–200. doi:10.1038/nature11458.

[41] D. G. Papageorgiou, I. A. Kinloch, R. J. Young, Mechanical properties of graphene and graphene-based nanocomposites, Progress in Materials Science 90 (2017) 75–127. doi:10.1016/j.pmatsci.2017.07.004.

[42] S. T. Kotikalapudi, R. Akula, R. P. Singh, Degradation mechanisms in carbon fiber–epoxy laminates subjected to constant low-density direct current, Composites Part B: Engineering 233 (March 2022). doi:10.1016/j.compositesb.2021.109516.

[43] B. J. Adohi, D. Bychanok, B. Haidar, C. Brosseau, Microwave and mechanical properties of quartz/graphene-based polymer nanocomposites, Applied Physics Letters 102 (7). doi:10.1063/1.4793411.

[44] A. Masouras, D. Giannopoulos, B. Hasa, A. Katsaounis, V. Kostopoulos, Hybrid graphene nanoplatelet/manganese oxide electrodes for solid-state supercapacitors and application to carbon fiber composite multifunctional materials, Journal of Energy Storage 23 (April) (2019) 515–525. doi:10.1016/j.est.2019.04.025.

[45] H. Wu, L. T. Drzal, Graphene nanoplatelet paper as a light-weight composite with excellent electrical and thermal conductivity and good gas barrier properties, Carbon 50 (3) (2012) 1135–1145. doi:10.1016/j.carbon.2011.10.026.

[46] J. Keyte, K. Pancholi, J. Njuguna, Recent Developments in Graphene Oxide/Epoxy Carbon Fiber-Reinforced Composites, Frontiers in Materials 6 (October) (2019) 1–30. doi:10.3389/fmats.2019.00224.

[47] X. Du, I. Skachko, A. Barker, E. Y. Andrei, Approaching ballistic transport in suspended graphene, Nature Nanotechnology 3 (8) (2008) 491–495. doi:10.1038/nnano.2008.199.

[48] Y. Li, H. Zhang, H. Porwal, Z. Huang, E. Bilotti, T. Peijs, Mechanical, electrical and thermal properties of in-situ exfoliated graphene/epoxy nanocomposites, Composites Part A: Applied Science and Manufacturing 95 (2017) 229–236. doi:10.1016/j.compositesa.2017.01.007.

[49] XGsciences.com.

[50] S. Chatterjee, J. W. Wang, W. S. Kuo, N. H. Tai, C. Salzmann, W. L. Li, R. Hollertz, F. A. Nüesch, B. T. Chu, Mechanical reinforcement and thermal conductivity in expanded graphene nanoplatelets reinforced epoxy composites, Chemical Physics Letters 531 (2012) 6–10. doi:10.1016/j.cplett.2012.02.006.

[51] A. S. Krieg, J. A. King, D. C. Jaszczak, I. Miskoglu, O. P. Mills, G. M. Odegard, Tensile and conductivity properties of epoxy composites containing carbon black and graphene nanoplatelets, Journal of Composite Materials 52 (28) (2018) 3909–3918. doi:10.1177/0021998318771460.

[52] S. Stankovich, D. A. Dikin, G. H. Dommett, K. M. Kohlhaas, E. J. Zimney, E. A. Stach, R. D. Piner, S. B. T. Nguyen, R. S. Ruoff, Graphene-based composite materials, Nature 442 (7100) (2006) 282–286. doi:10.1038/nature04969.

[53] S. Wu, R. B. Ladani, J. Zhang, E. Bafekrpour, K. Ghorbani, A. P. Mouritz, A. J. Kinloch, C. H. Wang, Aligning multilayer graphene flakes with an external electric field to improve multifunctional properties of epoxy nanocomposites, Carbon 94 (2015) 607–618. doi:10.1016/j.carbon.2015.07.026.

[54] O. M. Kwon, H. Watanabe, K. H. Ahn, S. J. Lee, Growths of mechanical elasticity and electrical conductance of graphene nanoplatelet/poly(lactic acid) composites under strong electric field: correlation with time evolution of higher order structure of graphene nanoplatelets, Rheologica Acta 56 (11) (2017) 871–885. doi:10.1007/s00397-017-1042-z.

[55] F. Wang, H. Wang, J. Mao, Aligned-graphene composites: a review, Journal of Materials Science 54 (1) (2019) 36–61. doi:10.1007/s10853-018-2849-4.

[56] G. H. Kim, Y. M. Shkel, Polymeric composites tailored by electric field, Journal of Materials Research 19 (4) (2004) 1164–1174. doi:10.1557/JMR.2004.0151.

[57] Z. Fan, A new approach to the electrical resistivity of two-phase composites, Acta Metallurgica Et Materialia 43 (1) (1995) 43–49. doi:10.1016/0956-7151(95)90259-7.

[58] S. T. Kotikalapudi, R. P. Singh, In Situ Measurement of AC Conductivity to Quantify Unidirectional Alignment of Graphene Nanoplatelets (GNPs) in Epoxy, Conference Proceedings of the Society for Experimental Mechanics Series 5 (2023) 79–86. doi:doi:10.1007/978-3-031-17445-2.

[59] H. Khoramishad, S. M. Hosseini Vafa, Effect of aligning graphene oxide nanoplatelets using direct current electric field on fracture behaviour of adhesives, Fatigue and Fracture of Engineering Materials and Structures 41 (12) (2018) 2514–2529. doi:10.1111/ffe.12852.

[60] E. T. Thostenson, T.-w. Chou, Aligned multi-walled carbon nanotube-reinforced com-

posites : processing and mechanical characterization, Journal of Physics D: Applied Physics 35 (2002) 77–80.

[61] A. I. Oliva-Avilés, F. Avilés, V. Sosa, A. I. Oliva, F. Gamboa, Dynamics of carbon nanotube alignment by electric fields, Nanotechnology 23 (46). doi:10.1088/0957-4484/23/46/465710.

[62] X. F. Zhang, R. S. Qin, Preparation of surface coatings on a conductive substrate by controlled motion of graphene nanoflakes in a liquid medium, Applied Surface Science 329 (2015) 276–280. doi:10.1016/j.apsusc.2014.12.171.

[63] F. Besharat, M. Manteghian, G. Gallone, A. Lazzeri, Electric field induced alignment of graphene oxide nanoplatelets in polyethersulfone matrix, Nanotechnology 31 (15). doi:10.1088/1361-6528/ab646b.

[64] L. S. Su, J. L. Tsai, Characterizing the mechanical properties of nanocomposites with aligned graphene, Polymer Composites 42 (8) (2021) 4005–4014. doi:10.1002/pc.26112.

[65] A. C. Patsidis, K. Kalaitzidou, G. C. Psarras, Graphite nanoplatelets/polymer nanocomposites: Thermomechanical, dielectric, and functional behavior, Journal of Thermal Analysis and Calorimetry 116 (1) (2014) 41–49. doi:10.1007/s10973-014-3704-8.

[66] A. A. Khurram, S. A. Rakha, P. Zhou, M. Shafi, A. Munir, Correlation of electrical conductivity, dielectric properties, microwave absorption, and matrix properties of composites filled with graphene nanoplatelets and carbon nanotubes, Journal of Applied Physics 118 (4). doi:10.1063/1.4927617.

[67] N. Yousefi, X. Lin, Q. Zheng, X. Shen, J. R. Pothnis, J. Jia, E. Zussman, J. K. Kim, Simultaneous in situ reduction, self-alignment and covalent bonding in graphene oxide/epoxy composites, Carbon 59 (2013) 406–417. doi:10.1016/j.carbon.2013.03.034.

[68] A. R. Ravindran, C. Feng, S. Huang, Y. Wang, Z. Zhao, J. Yang, Effects of graphene nanoplatelet size and surface area on the AC electrical conductivity and dielectric constant of epoxy nanocomposites, Polymers 10 (5) (2018) 19–35. doi:10.3390/polym10050477.

[69] N. M. Figueiredo, A. Cavaleiro, Dielectric Properties of Shape-Distributed Ellipsoidal Particle Systems, Plasmonics 15 (2) (2020) 379–397. doi:10.1007/s11468-019-01051-3.

[70] J. Li, J. K. Kim, Percolation threshold of conducting polymer composites containing 3D randomly distributed graphite nanoplatelets, Composites Science and Technology 67 (10) (2007) 2114–2120. doi:10.1016/j.compscitech.2006.11.010.

[71] X. Xia, Z. Zhong, G. J. Weng, Maxwell–Wagner–Sillars mechanism in the frequency dependence of electrical conductivity and dielectric permittivity of graphene-polymer nanocomposites, Mechanics of Materials 109 (2017) 42–50. doi:10.1016/j.mechmat.2017.03.014.

[72] X. Liu, Y. Wu, X. Wang, R. Li, Z. Zhang, Effect of interphase on effective permittivity of composites, Journal of Physics D: Applied Physics 44 (11). doi:10.1088/0022-3727/44/11/115402.

[73] G. M. Tsangaris, G. C. Psarras, N. Kouloumbi, Electric modulus and interfacial polarization in composite polymeric systems, Journal of Materials Science 33 (8) (1998) 2027–2037. doi:10.1023/A:1004398514901.

[74] M. G. Todd, F. G. Shi, Complex permittivity of composite systems: A comprehensive interphase approach, IEEE Transactions on Dielectrics and Electrical Insulation 12 (3) (2005) 601–611. doi:10.1109/TDEI.2005.1453466.

[75] M. Ezzat, N. A. Sabiha, M. Izzularab, Accurate model for computing dielectric constant of dielectric nanocomposites, Applied Nanoscience (Switzerland) 4 (3) (2014) 331–338. doi:10.1007/s13204-013-0201-5.

[76] C. F. Kuan, C. L. Chiang, S. H. Lin, W. G. Huang, W. Y. Hsieh, M. Y. Shen, Characterization and properties of graphene nanoplatelets/XNBR nanocomposites, Polymers and Polymer Composites 26 (1) (2018) 59–67. doi:10.1177/096739111802600107.

[77] M. R. Zakaria, M. H. Abdul Kudus, H. Md. Akil, M. Z. Mohd Thirmizir, Comparative study of graphene nanoparticle and multiwall carbon nanotube filled epoxy nanocomposites based on mechanical, thermal and dielectric properties, Composites Part B: Engineering 119 (2017) 57–66. doi:10.1016/j.compositesb.2017.03.023.

[78] A. A. Balandin, S. Ghosh, W. Bao, I. Calizo, D. Teweldebrhan, F. Miao, C. N. Lau, Superior thermal conductivity of single-layer graphene, Nano Letters 8 (3) (2008) 902–907. doi:10.1021/nl0731872.

[79] A. A. Balandin, Thermal properties of graphene and nanostructured carbon materials, Nature Materials 10 (8) (2011) 569–581. doi:10.1038/nmat3064.

[80] Z. Li, R. J. Young, N. R. Wilson, I. A. Kinloch, C. Vallés, Z. Li, Effect of the orientation of graphene-based nanoplatelets upon the Young's modulus of nanocomposites, Composites Science and Technology 123 (2016) 125–133. doi:10.1016/j.compscitech.2015.12.005.

[81] R. J. Nicholl, H. J. Conley, N. V. Lavrik, I. Vlassiouk, Y. S. Puzyrev, V. P. Sreenivas, S. T. Pantelides, K. I. Bolotin, The effect of intrinsic crumpling on the mechanics of free-standing graphene, Nature Communications 6. doi:10.1038/ncomms9789.

[82] H. Yan, Y. Tang, W. Long, Y. Li, Enhanced thermal conductivity in polymer composites with aligned graphene nanosheets, Journal of Materials Science 49 (15) (2014) 5256–5264. doi:10.1007/s10853-014-8198-z.

[83] P. Composites, C. N. Aligned, M. Field, Polymer Composites of Carbon Nanotubes, October (19) (2002) 1380–1383.

[84] B. W. Smith, Z. Benes, D. E. Luzzi, J. E. Fischer, D. A. Walters, M. J. Casavant, J. Schmidt, R. E. Smalley, Structural anisotropy of magnetically aligned single wall carbon nanotube films, Applied Physics Letters 77 (5) (2000) 663–665. doi:10.1063/1.127078.

[85] O. M. Kwon, H. Watanabe, K. H. Ahn, S. J. Lee, Interplay between structure and property of graphene nanoplatelet networks formed by an electric field in a poly(lactic acid) matrix, Journal of Rheology 61 (2) (2017) 291–303. doi:10.1122/1.4975335.

[86] N. Yousefi, X. Sun, X. Lin, X. Shen, J. Jia, B. Zhang, B. Tang, M. Chan, J. K. Kim, Highly aligned graphene/polymer nanocomposites with excellent dielectric properties for high-performance electromagnetic interference shielding, Advanced Materials 26 (31) (2014) 5480–5487. doi:10.1002/adma.201305293.

[87] Y. Wu, X. Lin, X. Shen, X. Sun, X. Liu, Z. Wang, J. K. Kim, Exceptional dielectric properties of chlorine-doped graphene oxide/poly (vinylidene fluoride) nanocomposites, Carbon 89 (2015) 102–112. doi:10.1016/j.carbon.2015.02.074.
URL http://dx.doi.org/10.1016/j.carbon.2015.02.074

[88] Y. Huang, J. Liang, Y. Chen, An overview of the applications of graphene-based materials in supercapacitors, Small 8 (12) (2012) 1805–1834. doi:10.1002/smll.201102635.

[89] A. Maniadi, M. Vamvakaki, M. Suchea, I. V. Tudose, M. Popescu, C. Romanitan, C. Pachiu, O. N. Ionescu, Z. Viskadourakis, G. Kenanakis, E. Koudoumas, Effect of graphene nanoplatelets on the structure, the morphology, and the dielectric behavior of low-density polyethylene nanocomposites, Materials 13 (21) (2020) 1–12. doi:10.3390/ma13214776.

[90] N. Yousefi, M. M. Gudarzi, Q. Zheng, S. H. Aboutalebi, F. Sharif, J. K. Kim, Self-alignment and high electrical conductivity of ultralarge graphene oxide-

polyurethane nanocomposites, Journal of Materials Chemistry 22 (25) (2012) 12709–12717. doi:10.1039/c2jm30590a.

[91] C. Min, D. Yu, J. Cao, G. Wang, L. Feng, A graphite nanoplatelet/epoxy composite with high dielectric constant and high thermal conductivity, Carbon 55 (2013) 116–125. doi:10.1016/j.carbon.2012.12.017.

[92] Y. C. Li, S. C. Tjong, R. K. Li, Electrical conductivity and dielectric response of poly(vinylidene fluoride)-graphite nanoplatelet composites, Synthetic Metals 160 (17-18) (2010) 1912–1919. doi:10.1016/j.synthmet.2010.07.009.

[93] Y. Y. Stehle, E. Robertson, R. Cortez, R. B. Bucinell, I. V. Vlassiouk, In-plane and through-plane dielectric properties of graphene oxide membrane: Effect of Al3+ modification, Materialia 23 (December 2021). doi:10.1016/j.mtla.2022.101442.

[94] E. J. Santos, E. Kaxiras, Electric-field dependence of the effective dielectric constant in graphene, Nano Letters 13 (3) (2013) 898–902. doi:10.1021/nl303611v.

[95] T. Pereira, Zhanhu Guo, S. Nieh, J. Arias, H. T. Hahn, Energy Storage Structural Composites: A Review, Journal of Composite Materials 43 (5) (2009) 549–560. doi:10.1177/0021998308097682.

[96] C. González, J. J. Vilatela, J. M. Molina-Aldareguía, C. S. Lopes, J. LLorca, Structural composites for multifunctional applications: Current challenges and future trends, Progress in Materials Science 89 (2017) 194–251. doi:10.1016/j.pmatsci.2017.04.005.

[97] S. Ekstedt, M. Wysocki, L. E. Asp, Structural batteries made from fibre reinforced composites, Plastics, Rubber and Composites 39 (3-5) (2010) 148–150. doi:10.1179/174328910X12647080902259.

[98] L. E. Asp, S. Leijonmarck, T. Carlson, G. Lindbergh, Realisation of structural battery

composite materials, ICCM International Conferences on Composite Materials 2015-July (July) (2015) 19–24.

[99] D. E. Fenton, J. M. Parker, P. V. Wright, Complexes of alkali metal ions with poly(ethylene oxide), Polymer 14 (11) (1973) 589. doi:10.1016/0032-3861(73)90146-8.

[100] M. B. Armand, P. G. Bruce, M. Forsyth, B. Scrosati, W. Wieczorek, Polymer Electrolytes, no. February, 2011. doi:10.1002/9780470977798.ch1.

[101] E. Quartarone, P. Mustarelli, A. Magistris, PEO-based composite polymer electrolytes, Solid State Ionics 110 (1-2) (1998) 1–14. doi:10.1016/s0167-2738(98)00114-3.

[102] H. S. Kim, K. S. Kum, W. I. Cho, B. W. Cho, H. W. Rhee, Electrochemical and physical properties of composite polymer electrolyte of poly(methyl methacrylate) and poly(ethylene glycol diacrylate), Journal of Power Sources 124 (1) (2003) 221–224. doi:10.1016/S0378-7753(03)00592-5.

[103] S. R. Raghavan, M. W. Riley, P. S. Fedkiw, S. A. Khan, Composite Polymer Electrolytes Based on Poly(ethylene glycol) and Hydrophobic Fumed Silica: Dynamic Rheology and Microstructure, Chemistry of Materials 10 (1) (1998) 244–251. doi:10.1021/cm970406j.

[104] K. S. Ngai, S. Ramesh, K. Ramesh, J. C. Juan, A review of polymer electrolytes: fundamental, approaches and applications, Ionics 22 (8) (2016) 1259–1279. doi:10.1007/s11581-016-1756-4.

[105] J. Shim, D. G. Kim, H. J. Kim, J. H. Lee, J. H. Baik, J. C. Lee, Novel composite polymer electrolytes containing poly(ethylene glycol)-grafted graphene oxide for all-solid-state lithium-ion battery applications, Journal of Materials Chemistry A 2 (34) (2014) 13873–13883. doi:10.1039/c4ta02667e.

[106] K. Xu, Nonaqueous Liquid Electrolytes for Lithium-Based Rechargeable Batteries, Chem Rev (104) (2004) 4303–4417.

[107] R. C. Agrawal, G. P. Pandey, Solid polymer electrolytes: Materials designing and all-solid-state battery applications: An overview, Journal of Physics D: Applied Physics 41 (22). doi:10.1088/0022-3727/41/22/223001.

[108] D. R. Dreyer, S. Park, C. W. Bielawski, R. S. Ruoff, The chemistry of graphene oxide, Chemical Society Reviews 39 (1) (2010) 228–240. doi:10.1039/b917103g.

[109] F. Barroso-Bujans, A. Alegría, J. A. Pomposo, J. Colmenero, Thermal stability of polymers confined in graphite oxide, Macromolecules 46 (5) (2013) 1890–1898. doi:10.1021/ma302407v.

[110] Y. C. Cao, C. Xu, X. Wu, X. Wang, L. Xing, K. Scott, A poly (ethylene oxide)/graphene oxide electrolyte membrane for low temperature polymer fuel cells, Journal of Power Sources 196 (20) (2011) 8377–8382. doi:10.1016/j.jpowsour.2011.06.074.

[111] M. S. Khan, A. Shakoor, Ionic conductance, thermal and morphological behavior of PEO-graphene oxide-salts composites, Journal of Chemistry 2015. doi:10.1155/2015/695930.

[112] M. Yuan, J. Erdman, C. Tang, H. Ardebili, High performance solid polymer electrolyte with graphene oxide nanosheets, RSC Advances 4 (103) (2014) 59637–59642. doi:10.1039/c4ra07919a.

[113] L. E. Asp, E. S. Greenhalgh, Structural power composites, Composites Science and Technology 101 (2014) 41–61. doi:10.1016/j.compscitech.2014.06.020.
URL http://dx.doi.org/10.1016/j.compscitech.2014.06.020

[114] J. F. Snyder, E. D. Wetzel, C. M. Watson, Improving multifunctional behavior in structural electrolytes through copolymerization of structure- and conductivity-promoting

monomers, Polymer 50 (20) (2009) 4906–4916. doi:10.1016/j.polymer.2009.07.050.
URL http://dx.doi.org/10.1016/j.polymer.2009.07.050

[115] S. Wang, K. Min, Solid polymer electrolytes of blends of polyurethane and polyether modified polysiloxane and their ionic conductivity, Polymer 51 (12) (2010) 2621–2628. doi:10.1016/j.polymer.2010.04.038.
URL http://dx.doi.org/10.1016/j.polymer.2010.04.038

[116] N. Shirshova, H. Qian, M. S. Shaffer, J. H. Steinke, E. S. Greenhalgh, P. T. Curtis, A. Kucernak, A. Bismarck, Structural composite supercapacitors, Composites Part A: Applied Science and Manufacturing 46 (2013) 96–107. doi:10.1016/j.compositesa.2012.10.007.
URL http://dx.doi.org/10.1016/j.compositesa.2012.10.007

[117] A. Javaid, K. K. Ho, A. Bismarck, J. H. Steinke, M. S. Shaffer, E. S. Greenhalgh, Carbon fibre-reinforced poly(ethylene glycol) diglycidylether based multifunctional structural supercapacitor composites for electrical energy storage applications, Journal of Composite Materials 50 (16) (2016) 2155–2163. doi:10.1177/0021998315602324.

[118] S. Kim, S. J. Park, Preparation and electrochemical properties of composite polymer electrolytes containing 1-ethyl-3-methylimidazolium tetrafluoroborate salts, Electrochimica Acta 54 (14) (2009) 3775–3780. doi:10.1016/j.electacta.2009.01.070.

[119] J. F. Snyder, R. H. Carter, E. D. Wetzel, Electrochemical and mechanical behavior in mechanically robust solid polymer electrolytes for use in multifunctional structural batteries, Chemistry of Materials 19 (15) (2007) 3793–3801. doi:10.1021/cm070213o.

[120] R. L. Sierakowski, I. Y. Telitchev, O. I. Zhupanska, On the impact response of electrified carbon fiber polymer matrix composites: Effects of electric current intensity and duration, Composites Science and Technology 68 (3-4) (2008) 639–649. doi:10.1016/j.compscitech.2007.09.019.

[121] P. E. Deierling, O. I. Zhupanska, Experimental study of high electric current effects in carbon/epoxy composites, Composites Science and Technology 71 (14) (2011) 1659–1664. doi:10.1016/j.compscitech.2011.07.017.

[122] R. Schapery, Thermal Expansion Coefficients of Composite Materials Based on Energy Principles, Journal of Composite Materials 2(3) (1968) 380–404. doi:https://doi.org/10.1177/002199836800200308.

[123] M. Miller, P. Feraboli, Electrical Characterization of Electrified Composite Plates, in: 49th AIAA/ASME/ASCE/AHS/ASC Structures, Structural Dynamics, and Materials, no. April, 2008, pp. 1–10. doi:https://doi.org/10.2514/6.2008-1917.

[124] ASTM, Standard Test Method for Determining the Compressive Properties of Polymer Matrix Composite Laminates Using a Combined Loading Compression (CLC) Test Fixture, Tech. rep. (2001). doi:10.1520/D6641.

[125] G. R. Dong S, Application of dynamic mechanical analysis for the study of the interfacial region in carbon fiber/epoxy composite materials, Polymer Composites 14 (5) (1993) 414–420. doi:10.1002/pc.750140508.

[126] A. Todoroki, M. Tanaka, Y. Shimamura, Measurement of orthotropic electric conductance of CFRP laminates and analysis of the effect on delamination monitoring with an electric resistance change method, Composites Science and Technology 62 (5) (2002) 619–628. doi:10.1016/S0266-3538(02)00019-2.

[127] J. C. Abry, S. Bochard, A. Chateauminois, M. Salvia, G. Giraud, In situ detection of damage in CFRP laminates by electrical resistance measurements, Composites Science and Technology 59 (6 SPEC. SEC.) (1999) 925–935. doi:10.1016/S0266-3538(98)00132-8.

[128] S. Wang, Z. Mei, D. D. Chung, Interlaminar damage in carbon fiber polymer-matrix

composites, studied by electrical resistance measurement, International Journal of Adhesion and Adhesives 21 (6) (2001) 465–471. doi:10.1016/S0143-7496(01)00023-9.

[129] S. Wang, D. D. Chung, Mechanical damage in carbon fiber polymer-matrix composite, studied by electrical resistance measurement, Composite Interfaces 9 (1) (2002) 51–60. doi:10.1163/156855402753642890.

[130] J. Wen, Z. Xia, F. Choy, Damage detection of carbon fiber reinforced polymer composites via electrical resistance measurement, Composites Part B: Engineering 42 (1) (2011) 77–86. doi:10.1016/j.compositesb.2010.08.005.

[131] Y. Chekanov, R. Ohnogi, S. Asai, M. Sumita, Positive temperature coefficient effect of epoxy resin filled filled with short carbon fibers, Polymer Journal 30 (5) (1998) 381–387. doi:https://doi.org/10.1295/polymj.30.381.

[132] I. M, Dielectric Breakdown Processes of Polymers, IEEE Transactions on Electrical Insulation 206-24. doi:10.1002/9783527680870.ch8.

[133] R. J. Hart, Characterization Of Carbon Fiber Polymer Matrix Composites Subjected To Simultaneous Application Of Electric Current Pulse And Low Velocity Impact, University of Iowa, Thesis (July) (2011) 160. arXiv:arXiv:1011.1669v3, doi:10.1017/CBO9781107415324.004.

[134] V. A. Zakrevskii, N. T. Sudar, A. Zaopo, Y. A. Dubitsky, Mechanism of electrical degradation and breakdown of insulating polymers, Journal of Applied Physics 93 (4) (2003) 2135–2139. doi:10.1063/1.1531820.

[135] M. Nagao, Electrical breakdown of polymeric insulating materials, in: Proceedings of the IEEE International Conference on Properties and Applications of Dielectric Materials, 2015, pp. 22–29. doi:10.1109/ICPADM.2015.7295200.

[136] L. Vouyovitch, N. D. Alberola, L. Flandin, A. Beroual, J. L. Bessede, Dielectric breakdown of epoxy-based composites: Relative influence of physical and chemical aging, IEEE Transactions on Dielectrics and Electrical Insulation 13 (2) (2006) 282–291. doi:10.1109/TDEI.2006.1624273.

[137] N. Saba, M. Jawaid, O. Y. Alothman, M. T. Paridah, A review on dynamic mechanical properties of natural fibre reinforced polymer composites, Construction and Building Materials 106 (2016) 149–159. doi:10.1016/j.conbuildmat.2015.12.075.

[138] R. Murugan, R. Ramesh, K. Padmanabhan, Investigation on static and dynamic mechanical properties of epoxy based woven fabric glass/carbon hybrid composite laminates, Procedia Engineering 97 (2014) 459–468. doi:10.1016/j.proeng.2014.12.270.

[139] M. Monti, M. Rallini, D. Puglia, L. Peponi, L. Torre, J. M. Kenny, Morphology and electrical properties of graphene-epoxy nanocomposites obtained by different solvent assisted processing methods, Composites Part A: Applied Science and Manufacturing 46 (1) (2013) 166–172. doi:10.1016/j.compositesa.2012.11.005.
URL http://dx.doi.org/10.1016/j.compositesa.2012.11.005

[140] O. V. Lozitsky, L. L. Vovchenko, L. Y. Matzui, Y. S. Milovanov, Dielectric properties of epoxy composites with mixed fillers including graphite nanoplatelets/BaTiO3, Molecular Crystals and Liquid Crystals 671 (1) (2018) 67–77. doi:10.1080/15421406.2018.1542086.

[141] L. C. Davis, Polarization forces and conductivity effects in electrorheological fluids, Journal of Applied Physics 72 (4) (1992) 1334–1340. doi:10.1063/1.351743.

[142] C. Fang, J. Zhang, X. Chen, G. J. Weng, Calculating the electrical conductivity of graphene nanoplatelet polymer composites by a monte carlo method, Nanomaterials 10 (6) (2020) 1–15. doi:10.3390/nano10061129.

[143] Z. M. Dang, M. S. Zheng, J. W. Zha, 1D/2D Carbon Nanomaterial-Polymer Dielectric Composites with High Permittivity for Power Energy Storage Applications, Small 12 (13) (2016) 1688–1701. doi:10.1002/smll.201503193.

[144] Y. Kou, X. Cheng, C. W. Macosko, Degradation and Breakdown of Polymer/-Graphene Composites under Strong Electric Field, Journal of Composites Science 6 (5). doi:10.3390/jcs6050139.

[145] L. Stobinski, B. Lesiak, A. Malolepszy, M. Mazurkiewicz, B. Mierzwa, J. Zemek, P. Jiricek, I. Bieloshapka, Graphene oxide and reduced graphene oxide studied by the XRD, TEM and electron spectroscopy methods, Journal of Electron Spectroscopy and Related Phenomena 195 (2014) 145–154. doi:10.1016/j.elspec.2014.07.003.

[146] Z. Q. Li, C. J. Lu, Z. P. Xia, Y. Zhou, Z. Luo, X-ray diffraction patterns of graphite and turbostratic carbon, Carbon 45 (8) (2007) 1686–1695. doi:10.1016/j.carbon.2007.03.038.

[147] J. Lee, K. Kim, W. I. Park, B. H. Kim, J. H. Park, T. H. Kim, S. Bong, C. H. Kim, G. Chae, M. Jun, Y. Hwang, Y. S. Jung, S. Jeon, Uniform graphene quantum dots patterned from self-assembled silica nanodots, Nano Letters 12 (12) (2012) 6078–6083. doi:10.1021/nl302520m.

[148] K. Habiba, V. I. Makarov, J. Avalos, M. J. Guinel, B. R. Weiner, G. Morell, Luminescent graphene quantum dots fabricated by pulsed laser synthesis, Carbon 64 (2013) 341–350. doi:10.1016/j.carbon.2013.07.084.

[149] K. Y. Chan, A. Baktash, B. Demir, E. L. Mayes, D. Yang, D. Q. Pham, K. T. Lin, A. P. Mouritz, A. S. Ang, B. Fox, B. Zhu, H. Lin, B. Jia, K. T. Lau, Tailoring mechanical and electrical properties of graphene oxide film for structural dielectric capacitors, Journal of Power Sources 482 (May 2020) (2021) 229020. doi:10.1016/j.jpowsour.2020.229020.

[150] G. Eda, A. Nathan, P. Wöbkenberg, F. Colleaux, K. Ghaffarzadeh, T. D. Anthopoulos, M. Chhowalla, Graphene oxide gate dielectric for graphene-based monolithic field effect transistors, Applied Physics Letters 102 (13). doi:10.1063/1.4799970.

[151] S. M. Mirabedini, H. Rahimi, S. Hamedifar, S. Mohsen Mohseni, Microwave irradiation of polypropylene surface: A study on wettability and adhesion, International Journal of Adhesion and Adhesives 24 (2) (2004) 163–170. doi:10.1016/j.ijadhadh.2003.09.004.

[152] H. Qian, A. R. Kucernak, E. S. Greenhalgh, A. Bismarck, M. S. Shaffer, Multifunctional Structural Supercapacitor Composites Based on Carbon Aerogel Modified High Performance Carbon Fiber Fabric, Applied materials and interfaces (ACS) 2013-July (2013) 2238–2243.

[153] A. J. Austin, S. T. Kotikalapudi, P. Rao, R. P. Singh, How Graphene Oxide Content in Poly (Ethylene Glycol) Affects Phase Separation in Epoxy Matrix for High-Performance Structural Supercapacitor Applications, Conference Proceedings of the Society for Experimental Mechanics Series 5 (2023) 87–92.

[154] R. Reece, C. Lekakou, P. A. Smith, A High-Performance Structural Supercapacitor, ACS Applied Materials and Interfaces 12 (23) (2020) 25683–25692. doi:10.1021/acsami.9b23427.

APPENDICES

Publications

Published research

- Kotikalapudi, Sai Tharun, Ravi Akula, and Raman P. Singh. "Degradation mechanisms in carbon fiber–epoxy laminates subjected to constant low-density direct current." Composites Part B: Engineering 233 (2022): 109516.

- Kotikalapudi, Sai Tharun, and Raman P. Singh. "Mechanical Strength Degradation of Carbon Fiber Polymer Matrix Composites Exposed to Constant Low-Density Direct Current." ASME International Mechanical Engineering Congress and Exposition. Vol. 59490. American Society of Mechanical Engineers, 2019.

- Kotikalapudi, Sai Tharun, and Raman P. Singh. "In situ measurement of AC conductivity to quantify unidirectional alignment of graphene nanoplatelets (GNPs) in epoxy" Mechanics of Composite, Hybrid & Multi-functional Materials, Volume 5, Conference Proceedings of the Society for Experimental Mechanics Series.

- Alan J Austin, Kotikalapudi, Sai Tharun, Padmanapan Rao, and Raman P. Singh. "How Graphene Oxide Content in Poly (Ethylene Glycol) Affects Phase Separation in Epoxy Matrix for High-Performance Structural Supercapacitor Applications" Mechanics of Composite, Hybrid & Multi-functional Materials, Volume 5, Conference Proceedings of the Society for Experimental Mechanics Series.

Planned journal publications

- Characterizing the unidirectional alignment of graphene nanoplatelets (GNPs) in epoxy using in situ AC conductivity measurements.
- Characterizing the planar alignment of graphene nanoplatelets (GNPs) in epoxy using external electric field.
- Effects of Graphene Oxide (GO) content on the phase separation of PEG/epoxy based solid polymer electrolyte (SPE).

Code for unidirectional alignment of GNPs

```
clc
clear all
density_epoxy= 1174.3;
density_hardener=950.22;
density_heloxy=910;
m_epoxy=100;
m_hardener=40;
m_heloxy=0;
m_tot=m_epoxy+m_hardener+m_heloxy;
mf_epoxy=m_epoxy/m_tot;
mf_hardener=m_hardener/m_tot;
mf_heloxy=m_heloxy/m_tot;
V_tot=m_epoxy/density_epoxy+m_hardener/density_hardener+m_
heloxy/density_heloxy;
Vf_epoxy=mf_epoxy/density_epoxy/(mf_epoxy/density_epoxy+mf_
hardener/density_hardener+mf_heloxy/density_heloxy);
Vf_hardener=mf_hardener/density_hardener/(mf_epoxy/density_
epoxy+mf_hardener/density_hardener+mf_heloxy/density_heloxy);
Vf_heloxy=1-(Vf_hardener+Vf_epoxy);
density=Vf_hardener*density_hardener+Vf_epoxy*density_epoxy+
Vf_heloxy*density_heloxy;
density_1=m_tot/V_tot;


a=(25e-6)/2; % radius of GNP (um)
b=(8e-9)/2; % half thickness of GNP (nm)
mg=2.65e-14;%mass of graphene in Kg
```

```
Wg=0.7/100;%weight fraction of graphene
t_electrodes=3e-3; %thickness of electrodes (m)
Eo=105; %Applied electric feild (V)
E=Eo/t_electrodes;%Electric feild strength (V/m)
Neta=1.1
mu_epon=7.2;%Pa.s
mu_heloxy=1.5/1000;%Pa.s
mu_epikure=0.05;

Epsilon=8.8e-12; %permitivity of vacuum
Epsilon_m=3.6*Epsilon; %permitivity of polymer

A=(pi*Epsilon_m*E^2)/((8*Neta)*((pi/2)-(b/a)));
theta_i=0:pi/200:pi/2.000005;
theta_f=0.01*pi/180;
t=(log(tan(theta_i)/tan(theta_f)))/A;
figure
plot(theta_i*180/pi,t/60,'lineWidth',5)
%title('Rotation time Vs Intitial angle')
set(gca,'FontSize', 18)
xlabel('Angle in degrees')
ylabel('Time (Minutes)')

kt=6*pi*((a^2)*b)^(1/3)*(abs((b/a)^2-1)^0.5)/
atan(abs((b/a)^2-1)^0.5/(b/a));
%Translational friction coeff
```

```
x0=mg/(Wg*density*2*a*2*a)%paper
x=0:x0/100:x0;
B=4*pi*a^4*E^2*Epsilon_m^2/(9*Neta*kt*Epsilon*(pi/2-b/a)^2);
tc=2*(x0^3-x.^3)/(3*B)
figure
plot(tc,x/1e-6,'lineWidth',5)
set(gca,'FontSize', 18)
%title('Translation time Vs distance')
xlabel('Translation time (Seconds)')
ylabel('Distance (um)')
```

VITA

Sai Tharun Kotikalapudi

Candidate for the Degree of

Doctor of Philosophy

Dissertation: EFFECTS OF ALIGNED GRAPHENE NANOPLATELETS (GNPS) ON THE MULTIFUNCTIONAL PERFORMANCE OF CARBON FIBER REINFORCED POLYMER (CFRP) COMPOSITES

Major Field: Mechanical Engineering

Biographical:

Education:

Completed the requirements for the Doctor of Philosophy in Mechanical Engineering at Oklahoma State University, Stillwater, Oklahoma in May 2023.

Completed the requirements for the Master of Science in Mechanical Engineering at University of Florida, Gainesville, Florida in 2017.

Completed the requirements for the Bachelor of Technology in Mechanical Engineering at SASTRA University, Thanjavur, Tamil Nadu, India in 2014.

Experience:

Sai Tharun Kotikalapudi was born in Hyderabad, India, in 1991. He was a member of ASME, MRS and SAMPE at OSU. He worked as a Mechanical Design Engineer for TCS from Nov 2014 to Nov 2015 and as a Research Assistant at University of Florida from Jan 2017 to Dec 2018. He was hired as a Graduate Research Assistant under Dr. Raman P. Singh at HRC as OSU-Tulsa from Jan 2019 to May 2023. He also worked as a Materials Engineer for Structured Ions. LLC during summer of 2022.